



# CHIRAL FLOW OF LIGHT IN PHOTONIC CRYSTALS WITH BROKEN SYMMETRIES

NIKHIL PARAPPURATH




# Chiral Flow of Light in Photonic Crystals with Broken Symmetries

Nikhil Parappurath

Ph. D. Thesis, Eindhoven University of Technology, July 2019  
*Chiral Flow of Light in Photonic Crystals with Broken Symmetries*  
Nikhil Parappurath

ISBN: 978-94-92323-28-6

Copyright: This work is licensed under the Creative Commons Attribution  
4.0 International License. 



The work described in this thesis was performed at:  
AMOLF, Science Park 104, 1098 XG Amsterdam, The Netherlands, and  
Delft University of Technology, 2600 GA Delft, The Netherlands.

This work is part of the Dutch Research Council (NWO), and an industrial  
partnership program between Philips and NWO.

A digital version of this thesis is available at:  
<https://ir.amolf.nl/> and <https://research.tue.nl/>.



# Chiral Flow of Light in Photonic Crystals with Broken Symmetries

PROEFSCHRIFT

ter verkrijging van de graad van doctor aan de Technische Universiteit  
Eindhoven, op gezag van de rector magnificus prof.dr.ir. F.P.T. Baaijens,  
voor een commissie aangewezen door het College voor Promoties, in het  
openbaar te verdedigen op woensdag 3 juli 2019 om 13:30 uur

door

Nikhil Parappurath

geboren te Perinthalmanna, India

Dit proefschrift is goedgekeurd door de promotoren en de samenstelling van de promotiecommissie is als volgt:

Voorzitter:	prof. dr. ir. G. M. W. Kroesen	
1 <sup>e</sup> promotor:	prof. dr. E. Verhagen	
2 <sup>e</sup> promotor:	prof. dr. L. Kuipers	(Technische Universiteit Delft)
leden:	dr. A. Amo	(CNRS - Université de Lille)
	prof. dr. A. F. Koenderink	(Universiteit van Amsterdam)
	prof. dr. B. Koopmans	
	prof. dr. K. A. Williams	
	dr. A. G. Curto	

*Het onderzoek of ontwerp dat in dit proefschrift wordt beschreven is uitgevoerd in overeenstemming met de TU/e Gedragscode Wetenschapsbeoefening.*

*To all my teachers*



# CONTENTS

<b>1</b>	<b>Introduction</b>	<b>1</b>
1.1	When light comes to light . . . . .	2
1.2	The vectorial nature of light . . . . .	3
1.3	Crystals for light . . . . .	5
1.3.1	Photonic crystals . . . . .	5
1.3.2	Bloch waves and dispersion relation . . . . .	6
1.3.3	Photonic crystal slabs . . . . .	9
1.4	Chirality in optics. . . . .	10
1.5	Topological insulators for light . . . . .	11
1.5.1	Topology . . . . .	11
1.5.2	Quantum Hall effect and quantum spin Hall effect . . . . .	13
1.5.3	The Su–Schrieffer–Heeger model . . . . .	14
1.6	Outline of the thesis . . . . .	16
<b>I</b>	<b>Resonant Scattering and Chirality in Photonic Crystals</b>	<b>19</b>
<b>2</b>	<b>Quasinormal Modes and the Scattering Matrix</b>	<b>21</b>
2.1	Introduction . . . . .	22
2.2	Theory . . . . .	24
2.2.1	Quasinormal modes . . . . .	24
2.2.2	Coupled-mode equations . . . . .	25
2.2.3	Expansion of the scattering matrix . . . . .	27
2.3	Applications . . . . .	31
2.3.1	Photonic crystal slab . . . . .	31
2.3.2	Asymmetric photonic crystal structure . . . . .	33
2.4	Discussion and conclusions . . . . .	35
	Appendices . . . . .	38
2.A	Case of orthogonal modes . . . . .	38
2.B	Free choice of amplitude normalization . . . . .	38
2.C	Convergence . . . . .	38
2.D	Electric field amplitudes of quasinormal modes . . . . .	39
<b>3</b>	<b>Asymmetric Transmission in Chiral Photonic Crystals</b>	<b>41</b>
3.1	Introduction . . . . .	42
3.2	On the origin of asymmetric transmission in resonant systems . . . . .	43
3.3	Predicting asymmetric transmission from the quasinormal modes of a system . . . . .	46
3.4	On the limit of asymmetric transmission . . . . .	48

3.5	Discussion and Conclusions . . . . .	52
	Appendices . . . . .	53
3.A	Derivation of asymmetric transmission from quasinormal modes . . . . .	53
3.B	Principle of Reciprocity and the limit of AT . . . . .	56
3.C	AT and its limit for general structures . . . . .	56
3.D	Implications of angular dependence. . . . .	58
<b>II</b>	<b>Topological Photonic Crystals for Light Manipulation</b>	<b>61</b>
<b>4</b>	<b>Direct Observation of Topological Edge States in Silicon Photonic Crystals</b>	<b>63</b>
4.1	Introduction . . . . .	64
4.2	The origin of topological states for light. . . . .	65
4.3	Mapping dispersion of topological states . . . . .	67
4.4	Detection of edge-state pseudospin . . . . .	69
4.5	Symmetry breaking and spin-spin scattering . . . . .	71
4.6	Conclusions. . . . .	75
	Appendices . . . . .	76
4.A	Experimental methods . . . . .	76
4.A.1	Sample design and FEM simulations. ....	76
4.A.2	Sample Fabrication . . . . .	77
4.A.3	Experimental Details . . . . .	77
4.A.4	Extraction of modes from dispersion crosscut . . . . .	79
4.B	Direct Fabry-Pérot reflections and reflectometry of an ordinary lattice . . . . .	79
4.C	Orthogonal linear polarization of bulk modes . . . . .	80
4.D	Tight-binding model . . . . .	81
4.E	Polarization tomography of edge states . . . . .	85
<b>5</b>	<b>Confining and Guiding Light in Topological Photonic Crystals</b>	<b>87</b>
5.1	Introduction . . . . .	88
5.2	Imaging guided light in topological waveguides . . . . .	89
5.3	Routing light around a topological junction. . . . .	92
5.4	Cavities formed by topological edges . . . . .	93
5.4.1	Cavity modes in topological ring resonators . . . . .	93
5.4.2	Comparison to a simple cavity model . . . . .	97
5.4.3	Effect of cavity shape on frequencies and losses . . . . .	98
5.5	Topological coupling of confined light . . . . .	99
5.6	Near-field study of topological photonic crystals. . . . .	104
5.6.1	Scanning near-field optical microscopy. ....	104
5.6.2	Near-field imaging of edge state propagation . . . . .	106
5.6.3	Visualizing higher-order Bloch harmonics of edge states. .	108

5.7	Conclusions and outlook. . . . .	111
	Appendices. . . . .	113
5.A	Experimental methods . . . . .	113
5.A.1	Sample design and fabrication . . . . .	113
5.A.2	Experimental setup details . . . . .	114
5.A.3	Extraction of cavity mode quality factors . . . . .	115
	<b>Bibliography</b>	<b>129</b>
	<b>Summary</b>	<b>131</b>
	<b>Samenvatting</b>	<b>135</b>
	<b>Acknowledgements</b>	<b>139</b>
	<b>About the author</b>	<b>143</b>
	<b>List of Publications</b>	<b>145</b>





# 1

## INTRODUCTION

*“Stories are light. Light is precious in a world so dark.  
Begin at the beginning. Tell Gregory a story. Make some light.”*

— Kate DiCamillo, *The Tale of Despereaux*, 2003

## 1.1. When light comes to light

ONE of the first ideas that comes to mind when we think of the word *light* is of vision. Visual perception happens when light reflected from objects reaches our eyes. Sources of light, from the sun that ensures our very existence on earth to the modern lamps that illuminate our dark dull home interiors, form an indispensable part of our life. Light, in a way, shapes the world around us as we see it. When it comes to light, however, there is a lot more to it than meets the eye; both figuratively and literally. Light is a carrier of both energy and information. This, together with the possibility of engineering its interaction with matter, made it a powerful presence in modern society where it finds immense applicability in a myriad of fields spanning food processing, health, defence, security, renewable energy and communication. Light with shorter wavelengths compared to visible spectrum can ensure clean drinking water (ultraviolet filters) while much longer wavelengths come handy when we need to quickly warm up our lunch in the cafeteria (microwave ovens). Various forms of light assist a multitude of applications like sensors, medical imaging, laser-assisted surgery, infrared vision, terahertz scanning devices, stealth radars, biometric systems, etc. Constant efforts in the field of photovoltaics aiming to fulfil our ever increasing energy requirements, from world-record solar cells [1] to fully solar-powered airports [2], demonstrate the power of light towards establishment of a sustainable planet. Among the applications, one of the most advanced and fast-evolving technologies is the field of communication. Its large information bandwidth and low loss make light a key player in the communication arena. With optical fibre networks that span thousands of kilometres to transport huge amounts of data across the globe forming the foundation for the internet [3, 4], lightwave communication has come a long way since Alexander Graham Bell's photophone in 1880 [5].

To harness the potential of light to the maximum extent, we should be able to control its interaction with matter to the best possible degree. Structuring matter at extremely small scales (smaller than the wavelength of light) offers interesting possibilities of manipulating light at the subwavelength-scale, opening a whole new world of physics called nano-optics [6]. Ever-increasing demand for faster, more efficient and secure information processing platforms is constantly stimulating quests for novel technologies. Bandwidth limitations and heat generation associated with electronic components used in integrated circuitries call for alternative optical technologies [7]. Use of light in information processing is making a huge headway in this regard with the advent of trailblazing research fields like quantum photonics [8] and silicon photonics [9, 10]. These fields continue to strive for realization of photonic components to replace electronic elements in the semiconductor industry as well as novel building blocks for quantum information processing. Addressing light-matter interaction from a fundamental perspective could provide

intriguing insights in this respect.

Light is an electromagnetic wave. Since electric and magnetic fields are quantities associated with both magnitude and direction, light fields can be described as vectors. This vectorial nature, which is behind the concept of *polarization*, makes light extra powerful, imparting the potential to encode both classical and quantum information in it.

This thesis aims to explore the interaction of polarized light with nanostructures, bringing about exotic effects to manipulate it in different ways like breaking the symmetry of its propagation and guiding light of different polarizations to different directions. Investigations presented in this thesis are mainly based on utilization of concepts like chirality and topology in periodically structured materials at the nanoscale called *photonic crystals*. This chapter provides a basic introduction to the main concepts that are used in the work presented in the thesis: Polarized light, photonic crystals, chirality and topological photonics. The final section presents an outline of the rest of the chapters.

## 1.2. The vectorial nature of light

Light is composed of oscillating electric and magnetic fields. *Polarization* is a term used to represent the direction of oscillation of the electric field vector in a propagating wave [11, 12]. If the electric field oscillations are restricted to a given direction (the field vector in the plane transverse to the propagation direction), light is said to be *linearly polarized*. If the field vector instead describes a circle in the transverse plane, the field is said to be *circularly polarized*.

Let us consider a light wave that is propagating along the  $z$  direction in a Cartesian coordinate system to illustrate the concept of polarization. The electric field in the plane perpendicular to the direction of propagation can be decomposed into two orthogonal components as  $\mathbf{E} = E_x \hat{\mathbf{x}} + E_y \hat{\mathbf{y}}$ , with

$$\begin{aligned} E_x &= E_{0x} \cos(\omega t - kz), \\ E_y &= E_{0y} \cos(\omega t - kz + \phi), \end{aligned} \quad (1.1)$$

where  $\hat{\mathbf{x}}$  and  $\hat{\mathbf{y}}$  represent unit vectors along the  $x$  and  $y$  axes,  $E_{0x}$  and  $E_{0y}$  represent the maximum amplitude of the components,  $\omega = 2\pi f$  is the angular frequency of the wave,  $t$  represents time,  $k$  is the propagation constant and  $\phi$  is the phase difference between the  $x$  and  $y$  components [13]. We have fixed the phase of  $E_x$  without loss of generality.

When the two components are in phase ( $\phi = 0$ ), the addition of in-plane field components results in a vector pointed along an angle  $\psi = \arctan(E_{0y}/E_{0x})$ , and light is said to be linearly polarized along  $\psi$ . Special cases of linear polarization are for example *horizontally polarized* light ( $\phi = 0$ ,  $E_{0y} = 0$ ,  $\psi = 0$ ) and *vertically polarized* light ( $\phi = 0$ ,  $E_{0x} = 0$ ,  $\psi = \frac{\pi}{2}$ ). Equal amplitudes of  $x$  and  $y$  components result in *diagonally polarized* light when in

phase ( $\phi = 0, \psi = \frac{\pi}{4}$ ) and light of *anti-diagonal polarization* when out of phase by  $\pi$  ( $\phi = \pi, \psi = -\frac{\pi}{4}$ ).

Light becomes circularly polarized upon a special combination of these components such that they have equal amplitude ( $E_{0x} = E_{0y}$ ) and are out of phase by  $\frac{\pi}{2}$  ( $\phi = \pm\frac{\pi}{2}$ ). To an observer looking in a direction opposite to the direction of propagation, the resulting vector, at the fixed location of the observer, describes a circle in the transverse plane, rotating clockwise or counter-clockwise depending on the sign of  $\phi$ . This effectively determines the handedness of light. Light is called *right-circularly polarized* when the phase difference is  $\phi = +\frac{\pi}{2}$ , and the vector rotates clockwise in *time* as seen by the observer. At a specific time, the tip of the electric field traces out a right-handed helix in *space* along the propagation direction ( $z$ ). When the  $x$  and  $y$  components are out of phase by  $\phi = -\frac{\pi}{2}$ , the field vector rotates counter-clockwise as seen by the observer, and light is called *left-circularly polarized*. For all other combinations of amplitudes and phases of the components, the resulting vector traces out ellipses of different orientations, and light is said to be *elliptically polarized* in a general sense. Circular polarization and linear polarization can be considered to be special cases of elliptical polarization [13].

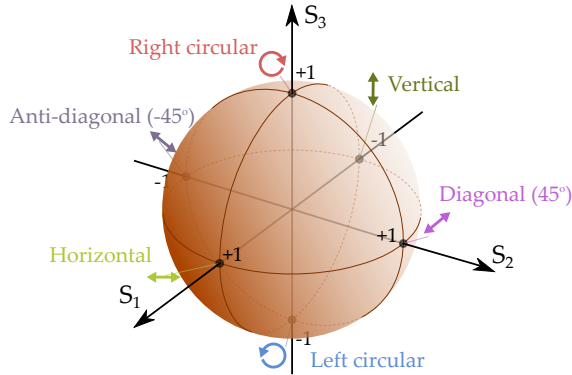


**Figure 1.1: Poincaré sphere:** Representation of different polarization states as points on the surface of a Poincaré sphere, drawn on a rectangular coordinate system formed by the Stokes parameters  $S_1$ ,  $S_2$ , and  $S_3$ .

The quantification of polarized optical fields forms an integral part of the work presented in this thesis. We use a set of mathematical parameters called *Stokes parameters* to effectively describe the polarization state of any optical field. For the planar field components in Eq. (1.1), they are defined as [14]:

$$S_0 = E_{0x}^2 + E_{0y}^2, \quad (1.2)$$

$$S_1 = E_{0x}^2 - E_{0y}^2, \quad (1.3)$$

$$S_2 = 2E_{0x} E_{0y} \cos \phi, \quad (1.4)$$

$$S_3 = 2E_{0x} E_{0y} \sin \phi. \quad (1.5)$$

Here  $S_0$  represents the total intensity of the electric field. The parameter  $S_1$  quantifies the degree of vertical or horizontal polarization of the field. The parameters  $S_2$  and  $S_3$  represent the degree of diagonal polarization and circular polarization of the field, respectively. If the field is fully polarized, i.e., the polarization does not fluctuate within the considered observation time [15], these parameters are related to each other by the identity:

$$S_0^2 = S_1^2 + S_2^2 + S_3^2. \quad (1.6)$$

Any polarization state can be encoded using a set of Stokes parameters. If we normalize the Stokes parameters such that the total intensity  $S_0$  is unity, we can represent these quantities in the form of a sphere of unit radius with axes  $S_1$ ,  $S_2$  and  $S_3$ , where each point on the surface of the sphere represents a unique polarization state in such a way that the entire surface covers the whole polarization space. Such a representation of polarized states, called the *Poincaré sphere*, helps us to form an intuitive understanding of the polarization states and their manipulation. Figure 1.1 shows an illustration of the Poincaré sphere. Some of the special polarization states along with the corresponding Stokes parameter value are provided in the figure. For example, perfectly right- and left-circularly polarized states are represented by the top and bottom poles of the sphere (along the axis  $S_3$ ). It is also obvious from the figure that the sign of  $S_3$  tells us the handedness of a circularly polarized field. We finally note that, for light of finite coherence, the light field may be partially polarized in the sense that the right hand side of Eq. (1.6) is smaller than  $S_0^2$ . Even in such cases, the four Stokes parameters describe the polarization state.

## 1.3. Crystals for light

### 1.3.1. Photonic crystals

Atoms or molecules arranged in an orderly fashion make up atomic or molecular crystals. The interaction of electron waves with the periodic potential in crystals gives rise to band structures in solid state physics featuring interesting phenomena like electronic *bandgaps* [16]. Bandgaps are ranges of energies at which electrons are forbidden to propagate within the crystal. In the late 1980's Eli Yablonovitch and Sajeev John independently proposed the existence of bandgaps for light waves using photonic analogues of atomic

crystals [17–19]. Such crystals, formed by periodic arrangements of materials with different dielectric constants, are called *photonic crystals* [20, 21].

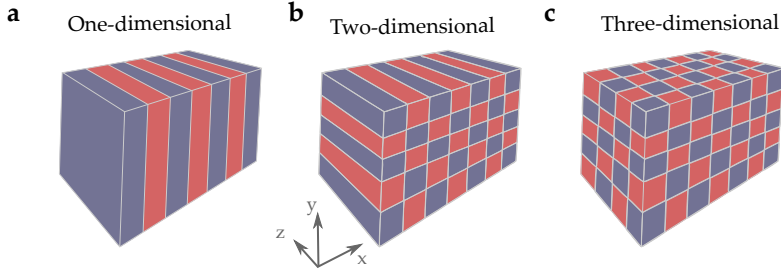


**Figure 1.2: Different types of photonic crystals:** a. One-dimensional, b. two-dimensional, and c. three-dimensional photonic crystals. Blue and red correspond to materials with different dielectric permittivity.

Depending on the dimensions along which the dielectric function is periodically modulated, photonic crystals can be classified as shown in Fig. 1.2 into one-dimensional (1-D), two-dimensional (2-D), and three-dimensional (3-D). When sheets of two materials having different refractive indices (or dielectric permittivity) are stacked together, they form a 1-D photonic crystal. Some man-made examples include Bragg reflectors and anti-reflection coatings used in lenses. Even though such structures provide stop-gaps for light (i.e., a finite range of wavelengths for which light cannot pass through the structures), these operational bandgaps are limited by the angle at which light passes through the structure. Compared to the 1-D photonic crystals, there can be numerous ways to achieve periodic modulations of dielectric constants in their 2-D or 3-D counterparts. Figure 1.2 shows one each from the many possible arrangements, where a 2-D photonic crystal is formed by stacking linear dielectric rods horizontally and a 3-D one is made by stacking cubes of different permittivities in an alternating fashion.

### 1.3.2. Bloch waves and dispersion relation

Let us consider a homogeneous medium having constant dielectric permittivity  $\epsilon = n^2$ , where  $n$  is the refractive index of the medium. The propagation of light in media is governed by Maxwell's equations [22]. For simplicity, we consider in the following a single polarization (such that the field can be written as a scalar) and propagation along the  $x$  axis. When the dielectric permittivity is homogeneous, the solutions are simple *plane waves* of the form  $E_k(x)e^{-i\omega t}$ , with

$$E_k(x) = E_0 e^{ikx}, \quad (1.7)$$

where  $k$  assumes a constant value  $k_0 = \pm n\omega/c$ . Now, let us consider a simple photonic crystal that is periodic in the  $x$  direction and is uniform along  $y$  and  $z$  (similar to Fig. 1.2a). The periodic modulation of the dielectric constant in this

photonic crystal is defined as  $\varepsilon(x) = \varepsilon(x + ma)$ . Here  $m$  is an integer and  $a$  is called the periodicity of the system. *Bloch's theorem* [23] states that, in such a discrete periodic medium, the solutions of the electromagnetic wave equations are also periodic and of the form:

$$E_k(x) = E_0 e^{ikx} u_k(x), \quad (1.8)$$

where  $u_k$  is a discrete periodic function with same periodicity as of  $\varepsilon$  such that  $u_k(x) = u_k(x + ma)$ . Wave solutions  $E_k$  given by Eq. (1.8) are called *Bloch states*.

Since  $u_k$  is a periodic function, it can be expressed in the form of a Fourier series as [24]:

$$u_k(x) = \sum_{j=-\infty}^{+\infty} C_j e^{ij \frac{2\pi}{a} x}, \quad (1.9)$$

so that Eq. (1.8) becomes:

$$E_k(x) = \sum_{j=-\infty}^{+\infty} C_j E_0 e^{i(k+j \frac{2\pi}{a})x}. \quad (1.10)$$

This form of expressing electric fields is called the plane-wave expansion method as the fields are expressed as the sum of a set of plane waves. Each  $j^{\text{th}}$  component in the expansion is called a *Bloch harmonic*; and  $C_j$  is the Bloch coefficient whose magnitude we call the *weight* of the Bloch harmonic.

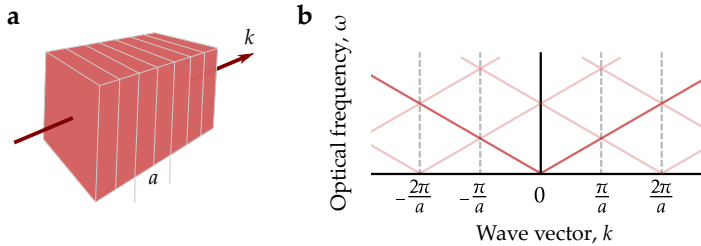


**Figure 1.3: Dispersion relation of a homogeneous medium with pseudo-periodicity:**  
**a.** Sketch of a homogeneous medium with imposed periodicity  $a$ . Direction of light propagation is indicated by the arrow. **b.** Bloch waves of the system. The dark and light red lines correspond to the fundamental and higher Bloch harmonics, respectively.

The relation between wave vector  $k$  and optical frequency  $\omega$  (eigenvalues of the wave equation) of a wave is called *dispersion relation*. Figure 1.3b shows the dispersion relation of a homogeneous medium with an artificially imposed pseudo-periodicity  $a$ . Of course, one can always consider homogeneous space to be periodic, with a lattice constant  $a$  that can be chosen at will. The dark red line represents the dispersion of the plane wave solution Eq. (1.7). Since the solution to wave equations in a homogeneous medium is a plane wave with wave vector  $k = \pm n\omega/c$ , the dispersion relation is linear. For a given optical

frequency, solutions can exist both at  $+k$  and  $-k$ . In other words, there is always a forward propagating and a backward propagating wave for a given frequency. In the dispersion relation, the direction of propagation is given by the slope of the dispersion. Defined as  $v_g = d\omega/dk$ , the slope quantifies the direction and speed of energy transport in the medium and is called the *group velocity* of the wave.

Due to the pseudo-periodicity  $a$ , we can define additional Bloch harmonics; a few of them are represented by the light red lines. Importantly, the weight  $C_j$  of each of these harmonics is necessarily zero due to the fact that the permittivity is not modulated, i.e., the harmonics are only there because we chose to artificially impose a periodicity.

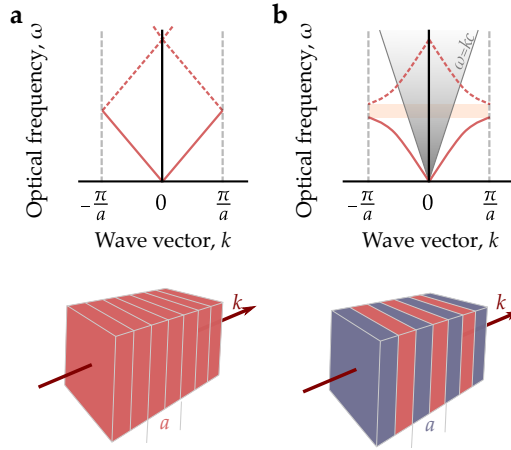


**Figure 1.4: Band folding in photonic crystals:** **a.** Dispersion relation of a homogeneous medium in the first Brillouin zone (dashed grey lines) with folded bands. Dashed red lines correspond to the folded dispersion. **b.** Dispersion relation of a 1-D photonic crystal with periodicity  $a$ . Shaded region in light orange indicates the bandgap opening. Grey solid line and shaded region indicates the air light line and light cone respectively.

The multiple harmonics can be constructed through the concept of *band folding* in photonic crystals. Equation (1.10) tells us that, in a periodic medium, the Bloch state with a certain wave vector  $k$  is identical to the state with wave vector  $k + j\frac{2\pi}{a}$ . Thus, the dispersion diagram is also periodic with a periodicity  $2\pi/a$ . This value is called the *reciprocal lattice vector* of the photonic crystal. Due to the periodicity of the dispersion diagram, it is possible to identify points in the wave vector axis along which we can *fold* the original dispersion (the dark red line in Fig. 1.3b) back to the region between  $k = -\frac{\pi}{a}$  and  $k = \frac{\pi}{a}$  to draw all the states within that region (including the light red lines in Fig. 1.3b). This region is called the *first Brillouin zone* in the reciprocal space. Figure 1.4a shows the folded version of the dispersion diagram of a homogeneous medium (from Fig. 1.3). We can notice a crossing of the states



around the Brillouin zone edge. A *photonic bandgap* opens around the crossing point when we introduce an actual periodic modulation in the medium, as shown in Fig. 1.4b.<sup>1</sup> This is accompanied by the fact that now in principle all Bloch harmonics can acquire a finite weight. These weights, a property of the eigenmodes, are not captured in dispersion diagrams such as Figs. 1.3b and 1.4, which only depict eigenvalues.

### 1.3.3. Photonic crystal slabs

Two-dimensional photonic crystals that are homogeneous in the direction perpendicular to the crystal plane (e.g., the  $z$  direction in Fig. 1.2) suffer from a drawback that they cannot confine light in the perpendicular direction. Even though 3-D photonic crystals offer confinement of light in all three directions, there are a lot of challenges associated with them in integration to the existing semiconductor fabrication techniques. This led to the evolution of a different class of structures called *photonic crystal slabs* [25, 26]. They offer a 2-D photonic bandgap due to the planar periodicity and can confine light in the third direction by *index guiding* (the phenomenon which confines light within the medium of higher refractive index when it is surrounded by a medium of lower refractive index — total internal reflection).

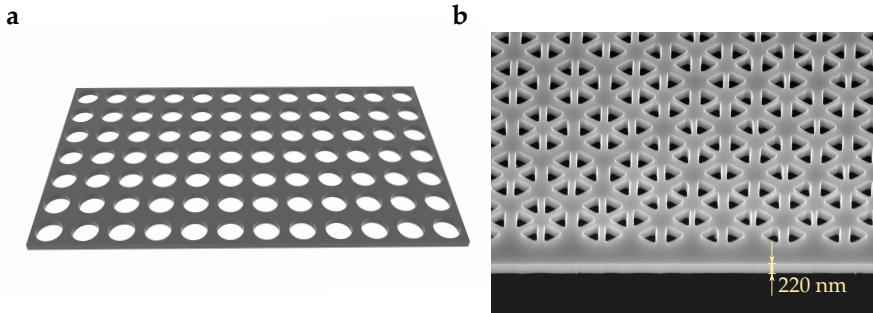


**Figure 1.5: Photonic crystal slabs:** **a.** Sketch of a 2-D photonic crystal slab of silicon with circular holes in a square lattice. **b.** Scanning electron microscope image of the silicon photonic crystal that we use in Ch. 4 and 5.

In a photonic crystal slab, the periodicity in the  $x$  and  $y$  directions still ensures the existence of Bloch modes within the structure propagating in the plane of the slab. Any photonic crystal mode with frequency  $\omega$  having at least one Bloch harmonic with wavevector magnitude  $k_j$  such that  $\omega > k_j c$ , can radiate into free-space. The area in the dispersion diagram above the light line where the modes leak out to free-space is called a *light cone* (see Fig. 1.4b). As we will see throughout the thesis, the existence of modes above the light

<sup>1</sup>Strictly speaking, we should call it a stop gap as propagation is forbidden only for a range of angles. Here, we however restrict ourselves to wavevectors normal to the interfaces.

line becomes important when we want to study photonic crystal modes using far-field experimental techniques.

Figure 1.5a shows an illustration of a typical photonic crystal slab. The structure consists of a square lattice of circular air holes embedded in a silicon slab of finite thickness. The periodicity is of the order of the wavelength of light. The work presented in this thesis mainly focuses on 2-D photonic crystal slabs of different types. The shape and geometry of the periodically arranged holes can vary depending on the applications. As a representative sample, Fig. 1.5b shows a scanning electron micrograph of one of the fabricated photonic crystal slabs that we use in chapters 4 and 5. The sample consists of triangular air holes arranged as hexagonal clusters in silicon.

## 1.4. Chirality in optics

In a broad sense, the term *chirality*<sup>2</sup> is used to denote objects or behaviour that are not *mirror-symmetric* [27]. Chiral objects cannot be super-imposed onto their mirror images through translations and rotations. The word chirality is derived from its most identified example: the human hand ( $\chi\epsilon\iota\rho$  in Greek, Fig. 1.6). Chirality in nature is also present at microscopic scales, ranging from the helical structure of DNA to sucrose and glucose molecules.

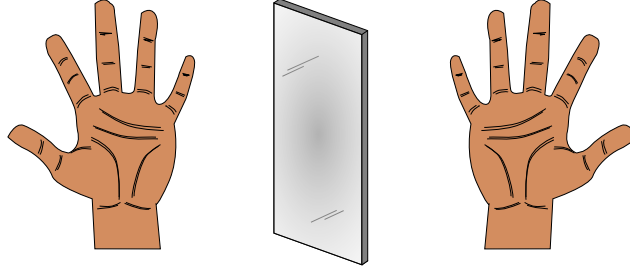


**Figure 1.6: Chirality:** The human hand is one of the most famous examples of a chiral object. The right hand is the mirror image of the left hand. It is not possible to superimpose the two.

Chiral materials interacting with light can present an interesting phenomenon called *optical activity*. This can either be the rotation of plane-polarized light while passing through the material (called *circular birefringence*), or the differential transmission of oppositely handed circularly polarized light (called *circular dichroism*). Optical activity assists characterization

<sup>2</sup>We note that there is an existing convention to denote edge states in quantum Hall topological insulators, which we encounter later, as *chiral* edge states. However, in this thesis, we don't follow this particular convention of edge state classification. We do not use the term 'chiral' to differentiate edges states in quantum Hall- and quantum spin Hall effect insulators. We use the term 'chiral' in the sense of 'handedness' or 'twistedness' throughout this thesis.

and sensing in chemistry and pharmaceutical science. In natural materials consisting of chiral molecules, these effects are quite weak. Thus, the reverse application, i.e., using chiral response to manipulate light, is challenging in small systems.

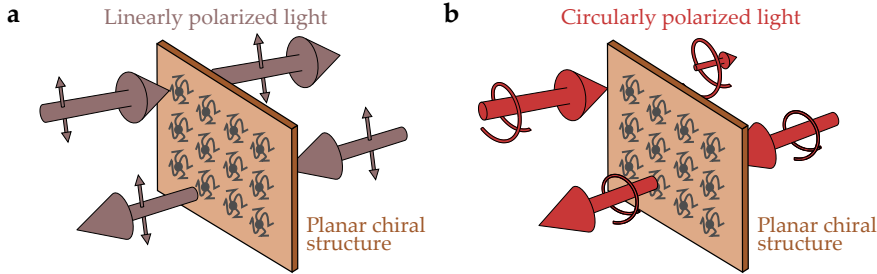


**Figure 1.7: Asymmetric transmission (AT) in planar chiral structures:** a. a planar chiral structure offering zero AT for linearly polarized light impinging from opposite directions. b. Asymmetric transmission for circularly polarized light in planar chiral structures. The structure offers less transmission in the forward direction and more transmission in the backward direction for right-circularly polarized incidence.

Artificial structures with geometric chirality at the nanoscale can be used to create chiroptical responses much larger than that from bulk materials. One of the most pronounced effects that can be brought about is *asymmetric transmission* (AT). A structure is said to be asymmetrically transmitting when light of a given polarization is transmitted through a structure by different amounts for opposite directions of incidence. Only strictly chiral objects can display AT for all angles and polarizations. For example, a structure that is only chiral in a two-dimensional plane (a so-called *planar chiral* structure, such as depicted in Fig. 1.7) cannot offer AT for normally incident linearly polarized light: The light ‘sees’ the structure in the same way from both directions. Such a structure can offer AT only for circularly polarized light, which does ‘see’ the in-plane handed nature of the structure.

To have AT for linearly polarized light, the interacting structures should also have a broken mirror-symmetry in the propagation direction. We will encounter such photonic crystal structures capable of offering asymmetric transmission for linearly polarized light in dielectric materials in Ch. 3 .

## 1.5. Topological insulators for light

### 1.5.1. Topology

Physics often borrows concepts from mathematics and applies them to the description of phenomena to bring about fascinating effects and applications. *Topology* is the branch of mathematics that studies properties of spaces or sur-

faces that do not change under smooth continuous deformations [28]. Physics embraced the concept of topology to form a whole new field—topological physics—hatching a bunch of groundbreaking brainchildren: from topological phases of matter in condensed matter physics to exotic protected states of light in photonics.



**Figure 1.8: Topological invariants:** Prof. Thors Hans Hansson explaining the concept of topological invariants using a bun, bagel, and a pretzel during the announcement of 2016 Nobel Prize in physics. *Image courtesy: NobelPrize.org. Nobel Media AB 2019.*

In topological physics, quantities that are preserved under deformations, called *topological invariants*, play important roles. The concept of topological invariants is often introduced with the example of buns, bagels and pretzels (Fig. 1.8). The notion invoked here is that the number of holes in the system can be used to differentiate systems of different geometrical topology. For example, a bun and a bowl belong to a single topological class (zero holes). It is always possible to continuously deform a bun to the shape of a bowl without introducing holes in the system. The number of holes in the system is preserved against continuous deformations. In a similar way, a bagel and a coffee mug would belong to another topological class (one hole). Here the topological invariant is the *genus*, denoting the number of holes of the system, and it can only have integer values. Even though this system can serve as an excellent example for a general introduction of topology, we should not confuse ourselves by tying the notion of topology uniquely to the shape of external geometries. Most of the interesting topological physics rely on different topological invariants, which are calculated through integrals of various functions defined on the band structures of materials, thus quantifying the global structure of Bloch states of the system in momentum space [29, 30]. These invariants can be integers ( $\in \mathbb{Z}$ , called *Chern numbers*) or binary values ( $\in \mathbb{Z} \bmod 2$ , called  $\mathbb{Z}_2$  topological invariants).

### 1.5.2. Quantum Hall effect and quantum spin Hall effect

The power of topology comes to view when certain physical behaviour or function is linked to topological invariants. The best known example is the existence of *edge states*. When two materials having energy gaps that are described by different topological invariants are brought together, topology dictates that there must exist states localized to the boundary, effectively closing the energy gap. This condition is called the *bulk-edge correspondence*, which we will discuss later in this section. A famous example is the *integer quantum Hall effect* (QHE) [31, 32] in two-dimensional electronic systems (Fig. 1.9a). In the QHE, a strong magnetic field applied perpendicular to the material prevents electronic conduction in the bulk, but does allow electrons to ‘skip’ along the edges. The material is insulating in the bulk while supporting edge states that are responsible for quantized Hall conductance. These states are non-reciprocal and can travel in only one direction along an edge, determined by the sign of the magnetic field. As their existence is guaranteed and direction is locked, they show remarkable robustness against disorder. If the state encounters a defect in its course, because it is not allowed to travel in the opposite direction, it will pass it without scattering.

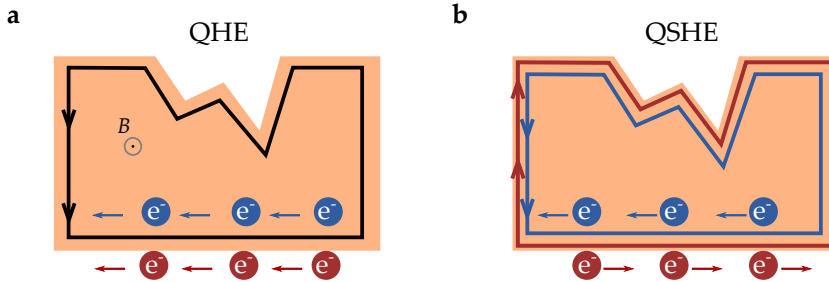


**Figure 1.9: Quantum Hall effect and quantum spin Hall effect:** **a.** A sketch illustrating the quantum Hall effect in electronics. Application of a magnetic field perpendicular to a 2-D insulator causes electrons to travel unidirectionally along the edges, giving rise to edge current (indicated by the black line) that is robust against disorders. Both up-spin electrons (red) and down-spin electrons (blue) travel in the same direction. **b.** Sketch of a topological insulator where up-spin electrons (red) and down-spin electrons (blue) travel in the opposite directions along the edge. Electrons with a given spin travel unidirectionally.

The explicit requirement of an external magnetic field for unidirectional transport of electrons was lifted with the discovery of the phenomenon of the *quantum spin Hall effect* (QSHE) in a new class of materials called topological insulators (Fig. 1.9b) [33–35]. The effect relies on *spin*, the intrinsic angular momentum of electrons [36]. In the QSHE, electrons with positive spin travel in one direction while negative-spin electrons travel in the opposite direction along edges of materials that are insulating in the bulk. Analogous to the

QHE, these states are topologically protected. This behaviour, originating from *spin-orbit coupling*, offers robust backscattering-free conduction as long as disorder does not induce spin-flips.

Realizing similar effects for light has huge significance both in view of possible applications and fundamental understanding. The prospects of backscattering-free propagation for light immune to defects are highly promising, because of the large and detrimental role of disorder in photonic systems, e.g. in the field of communication. The requirement of magnetic fields or gyromagnetic materials limits the realization of the QHE for photonic applications. Realization of the QSHE for light can be made possible with methods that allow light fields, in particular their vectorial nature, to mimic the opposite spins for electrons [37–40]. In Ch. 4 we will investigate a system that offers spin-orbit coupling for light via states that live at the boundary between two photonic crystals with different band structure topologies.

### 1.5.3. The Su–Schrieffer–Heeger model

The origin of gapless edge states when two gapped materials with different topological invariants are brought together is generally explained with the concept of bulk–boundary correspondence in topological physics, which we illustrate in the following. To introduce the concepts of band inversion and symmetry breaking that we will employ later, let us consider a simple yet concrete topological model: The *Su–Schrieffer–Heeger* (SSH) model. The model was first proposed by W. P. Su, J. R. Schrieffer, and A. J. Heeger to describe the electronic states in the 1-D long-chain polymer polyacetylene [41, 42]. The top panel of Fig. 1.10a shows the chemical structure of a polyacetylene chain. In the SSH method, the band structure of the 1-D chain is calculated using a *tight-binding* approximation. The tight-binding approach is an approximation that describes wavefunctions of a periodic system using interactions between wavefunctions of the isolated atoms situated in separate atomic lattice sites [43]. Here we follow the conventions outlined in Ref. [44]. The calculations of dispersion and electronic wavefunctions illustrated in Fig. 1.10b-e have been adapted from Ref. [45].

The SSH method describes hopping of electrons across a lattice where each unit cell contains two atomic sites as shown in the bottom panel of Fig. 1.10a. The hopping amplitudes across the chain are defined by an intra-cell amplitude  $v$  (brown line) and an inter-cell amplitude  $w$  (pink line) such that  $v = 1 - w$ . In the figure, the length of these lines represent the strength of coupling between atomic sites (a shorter line corresponds to a stronger bond). The dispersion relation of such a system is given by [44]:

$$E(k) = (v^2 + w^2 + 2vw \cos k)^{\frac{1}{2}}. \quad (1.11)$$

Let us consider three systems:  $v > w$ ,  $v < w$  and  $v = w$ . For the  $v > w$  case, the dispersion is gapped at the Brillouin zone edge as can be seen in Fig. 1.10b.

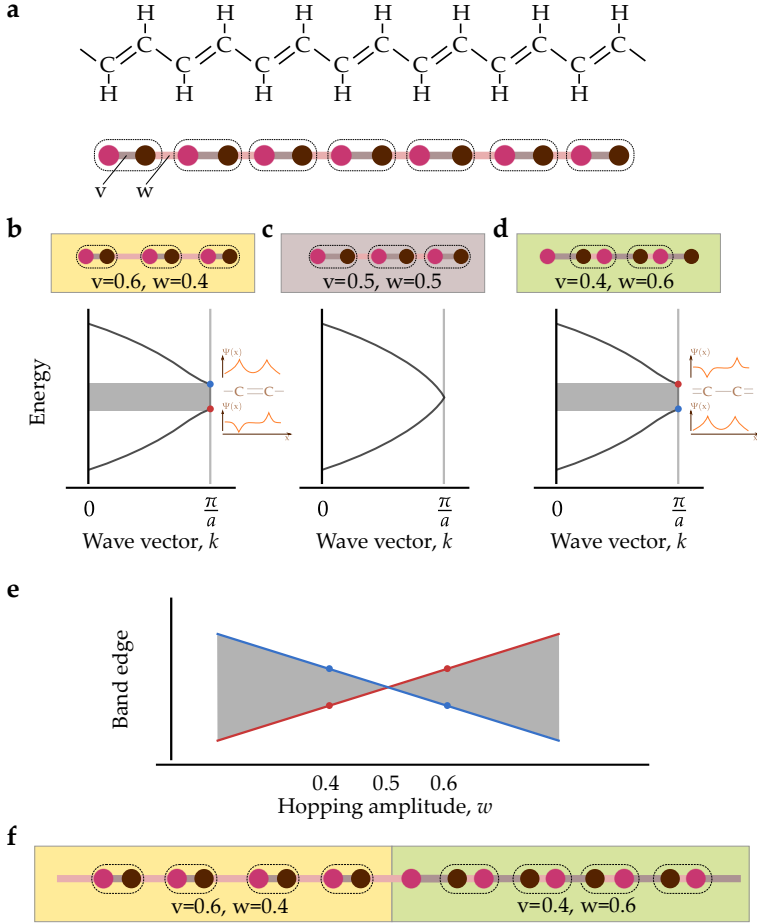


**Figure 1.10: The Su-Schrieffer-Heeger (SSH) model:** **a.** Chemical structure of polyacetylene chain (top panel) and SSH tight-binding model (bottom panel). Each unit cell (dashed rectangular) contains two atomic sites. Intra-cell and inter-cell hopping amplitudes are represented by brown ( $v$ ) and pink ( $w$ ) lines, respectively. Length of these lines represents the strength of coupling between atomic sites such that shorter lines corresponds to stronger bonds. **b-d.** Dispersion relations when  $v > w$ ,  $v = w$  and  $v < w$  respectively. Symmetric and antisymmetric wavefunctions at the band edges, represented by blue and red dots, are shown right next to them. **e.** Variation of bandgap as a function of hopping parameter  $w$ . Blue and red lines track the symmetric and antisymmetric band edges respectively. Subfigures **b-e** are based on calculations and figures found in Ref. [45]. **f.** An edge formed between two SSH chains with different couplings.

The electronic wavefunctions of the band edges are shown right next to them. The state at the top band edge is symmetric in the unit cell, indicated by a blue dot in the figure. The bottom edge of the gap features an antisymmetric state,

indicated by a red dot. There is also a gap at the Brillouin zone edge when the inter-cell hopping amplitude  $v$  is less than the intra-cell hopping amplitude  $w$  as shown in Fig. 1.10d. Indeed, the energy spectrum must be identical to the previous scenario, as we can obtain the case  $v < w$  from the case  $v > w$  by a simple shift of the definition of a unit cell in the infinite chain. However, this means that there is an inversion in symmetries of the electronic wavefunctions in the unit cell. The top edge of the band is now antisymmetric and the bottom edge is symmetric. The gap closes for the  $v = w$  case as can be seen in Fig. 1.10c. If we plot the energy gap at the Brillouin zone edge as a function of inter-cell hopping amplitude, it can be seen that the continuous variation of hopping amplitude from  $w < v$  case to  $w > v$  is necessarily associated with the closing of the gap (Fig. 1.10e), which is related to the inversion of symmetry between the two cases. The bandgaps at opposite sides of the  $v = w$  condition can be characterized by a different topological invariant.<sup>3</sup> When two such systems are brought together, the topological phase transition (closing and opening the gap) at the boundary necessitates the existence of edge states. These are localized at the boundary between different domains (Fig. 1.10f) and have a spatial extent that is inversely proportional to the size of the bandgap, i.e. the magnitude of  $|v - w|$ . Importantly, the existence of these states is protected to disorder in the frequencies or coupling rates, as long as that disorder is not large enough to close the bandgap.

We will see later in Ch. 4 that a continuous symmetry breaking that is similar to the deviation from the  $v = w$  case in the SSH model can create topological bandgaps in two-dimensional systems, which also feature band inversion and the existence of protected edge states.

## 1.6. Outline of the thesis

This thesis explores the possibilities of symmetry breaking at the nanoscale to selectively couple the direction and polarization of light waves using photonic crystal systems. The thesis is organized in two parts:

### Part I: Resonant Scattering and Chirality in Photonic Systems

This part focuses on the far-field properties of a system's eigenmodes and uses these to develop a theoretical framework for designing high-performance nanophotonic systems with desirable scattering properties such as asymmetric transmission.

In **chapter 2**, we introduce a theoretical formalism to predict the behaviour of (polarized) light waves as they interact with a given system. Using coupled mode theory, we show that the scattering matrix, a mathematical tool that quantifies the relation between incoming and outgoing waves, can be fully

<sup>3</sup>For a mathematical definition of the topological invariant called *winding number*, see Refs. [44, 46].



reconstructed from the knowledge of complex eigenfrequencies and the far-field properties of the system's quasinormal eigenmodes.

**Chapter 3** applies the theoretical formalism to the prediction and optimization of structural chirality for polarization manipulation in nanophotonic systems. This chapter concentrates on the phenomenon of AT. We probe the origin of AT in resonant systems and find its relation to the systems' complex eigenmodes. Building upon the theoretical framework presented in chapter 2, we develop a strategy to find structures that can offer very high AT. We discover that there exists a fundamental limit to the maximum AT possible for a single mode in any chiral resonator. A design route for a highly chiral dielectric photonic crystal structure that reaches this fundamental limit for AT is proposed.

## Part II: Topological Photonic Crystals for Light Manipulation

This part discusses the realization and applications of photonic spin-orbit coupling in topological photonic crystals. The fabrication, observation, analysis and robustness of topological edge states in silicon photonics are discussed and experimentally investigated.

In **chapter 4**, we realize an optical analogue of spin-orbit coupling in silicon photonic crystals. We directly observe photonic QSHE edge states in this system. Using Fourier microscopy and polarimetry, we probe the origin of their topological protection and reveal that the edge-state pseudospin is encoded in its unique far-field circular polarization. We quantify the small spin-spin scattering that is inherent due to the symmetry-breaking present in the system.

Finally, in **chapter 5**, we demonstrate the guiding, routing, confinement and coupling of these edge states in nanophotonic structures. The robustness of protected propagation is visualized along topological waveguides and sharp chiral junctions. Optical cavities are fabricated to demonstrate the topological properties of confinement and coupling of light in these cavities. The thesis ends with a section on the first near-field observation of topological edge states in the photonic domain. Using polarization-resolved photon scanning tunnelling microscopy, we study the different Bloch harmonics that compose the states of topological photonic crystals.



# I

## RESONANT SCATTERING AND CHIRALITY IN PHOTONIC CRYSTALS



# 2

## QUASINORMAL MODES AND THE SCATTERING MATRIX

*“[...] , the grand thing is to be able to reason backwards.”*

— Sir Arthur Conan Doyle, *A Study in Scarlet*, 1887

*It is well known that the quasinormal modes (or resonant states) of photonic structures can be associated with the poles of the scattering matrix of the system in the complex-frequency plane. In this chapter, the inverse problem, i.e., the reconstruction of the scattering matrix from the knowledge of the quasinormal modes, is addressed. We develop a general and scalable quasinormal-mode expansion of the scattering matrix, requiring only the complex eigenfrequencies and the far-field properties of the eigenmodes. The theory is validated by applying it to the resonant scattering properties of two-dimensional photonic crystal slabs with multiple overlapping electromagnetic modes.*

## 2.1. Introduction

Optical systems can be driven by external light waves, causing them to absorb or radiate energy. The scattering matrix is a powerful tool that can tell us a lot about the response of a system when it is excited by external light fields, by describing the relation between all possible incoming and outgoing light waves. Scattering matrices enjoy a well deserved popularity in electromagnetic modelling, ranging from microwave devices [48] to nanophotonics applications, such as scattering and transmission from nanostructured objects [49–51]. Physical systems can also be represented in terms of the modes of the system. For nonconserving systems, which lose energy by radiation after being driven externally, these modes are called quasinormal modes, resonant states, or leaky modes [52].<sup>1</sup>

Most of the systems that are usually investigated with scattering-matrix techniques display a highly structured resonant response as a function of the excitation frequency (or energy). Quasinormal modes represent the bare skeleton around which such a frequency-dependent response is built. These resonances in the spectrum are also directly related to the poles of the scattering matrix in the complex-frequency plane [53, 54]. The interplay among different electromagnetic modes has been proven to be crucial for explaining several intriguing phenomena, such as Fano resonances in optical systems [55], scattering dark states [56, 57], the optical analogue of electromagnetically induced transparency and superscattering [58], and for designing new optical materials, such as optical metasurfaces for wavefront shaping [59]. A deeper insight into the connection between quasinormal modes and scattering properties of the system would help us to understand and predict the behaviour of complex optical systems. For example, it allows to model the transmission of light through complex nanostructures by describing the system in terms of a few parameters that describe mechanisms such as coupling, dissipation, resonances etc. An extremely interesting and desirable functionality in this respect would be the ability to reconstruct *ab initio* the entire scattering matrix of a system from the knowledge of its quasinormal modes. Not only would such quasinormal-mode expansion contribute to the understanding of complicated spectral features in terms of interference and superposition of resonant states, but it would also offer practical advantages from the numerical point of view, since a full eigenmode calculation is generally faster and more comprehensive than a large number of single-frequency simulations.

Temporal coupled mode theory for optical resonators offers a promising theoretical platform to carry out this program. Such a framework has been fruitfully employed to study the transmission of layered photonic-crystal structures [55, 60, 61], gratings [62], coupled cavities and waveguides [63, 64], and the scattering cross section of nanoparticles [56, 65, 66]. However,

<sup>1</sup>A more rigorous definition of quasinormal modes in electromagnetic systems is presented later in Sec. 2.2.1.

coupled-mode theory has been typically restricted to a selection of only one or two modes of the optical system. The residual spectral response is accounted for by a slowly-varying frequency-dependent background, which is typically fitted from simulation data [55, 60, 61, 63]. Part of the difficulty in expanding coupled-mode theory by including an arbitrary number of modes lies in estimating the coupling coefficients that relate the resonant states with the input–output channels. For a small number of modes, these can be obtained from symmetry considerations [55, 63] or from the temporal decay rates [61]. However, in order to address the general case of multiple modes and an arbitrary configuration of input–output channels, a direct connection between the parameters of coupled-mode theory and the far-field properties of quasinormal modes is required.

In this chapter, we establish such a connection and present a general theory to expand the scattering matrix on the quasinormal modes of photonic systems, which can be directly scaled to any number of eigenmodes and incoming or outgoing channels. The theory, based on the far-field asymptotic behaviour of the modes and the unitarity property of the scattering matrix, represents a fully predictive tool that does not require the fitting of an additional nonresonant background. Modal methods such as the one we present here offer a deeper physical insight into the properties of resonant systems, because they allow us to draw a connection between the origin of complicated spectral features and the characteristics of the underlying quasinormal modes. For these reasons, they are particularly suitable for describing, understanding, and optimizing complex photonic systems.

There are formal similarities between our results and the expansion of the electromagnetic Green function on normalized quasinormal modes, which is a well known result from classical electrodynamics [67–69]; of course, when the expansion of the Green function is known for any point in space, then the scattering properties of the system can also be obtained [69, 70]. The theory that we present is formulated in a basis of input and output channels and it differs from these approaches in requiring only the far-field behaviour of the modes at the input–output ports, as opposed to the full spatial distribution of the eigenfield. Moreover, our theory is independent of the choice of the normalization of the quasinormal modes.

The chapter is organized as follows. In Sec. 2.2 we derive the quasinormal-mode expansion of the scattering matrix, whereas in Sec. 2.3 we numerically validate the theory in the case of photonic crystal slabs, a class of systems that is particularly relevant in the subsequent chapters. In this section, we use the theoretical formalism derived in Sec. 2.2 to predict the transmission properties of photonic crystal systems from the far-field properties of the quasinormal modes computed independently by a finite element solver.

## 2.2. Theory

### 2.2.1. Quasinormal modes

We consider only non-absorbing dielectric systems in this thesis.<sup>2</sup> Note, however, that such optical systems are still non-conservative because of the energy lost via far-field radiation. The photonic system is described by a spatially inhomogeneous distribution of the dielectric function  $\varepsilon(\mathbf{r}, \omega)$ . It is assumed that in the limit  $r \rightarrow \infty$ , the dielectric function  $\varepsilon(\mathbf{r}, \omega)$  tends to the constant value  $\varepsilon_b$  and we define  $\Delta\varepsilon(\mathbf{r}, \omega) = \varepsilon(\mathbf{r}, \omega) - \varepsilon_b$ . For the photonic, non-magnetic systems that we consider, we can assume that the permeability is non-dispersive.

Modes of an electromagnetic system are defined as discrete sets of transverse solutions  $(\tilde{\mathbf{E}}_j, \tilde{\mathbf{H}}_j)$  of the source-free Maxwell's equations of the system:

$$\begin{aligned} -\frac{i}{\mu_0} \nabla \times \tilde{\mathbf{E}}_j(\mathbf{r}) &= \tilde{\omega}_j \tilde{\mathbf{H}}_j(\mathbf{r}), \\ \frac{i}{\varepsilon_0 \varepsilon(\mathbf{r}, \tilde{\omega}_j)} \nabla \times \tilde{\mathbf{H}}_j(\mathbf{r}) &= \tilde{\omega}_j \tilde{\mathbf{E}}_j(\mathbf{r}), \end{aligned} \quad (2.1)$$

with some boundary conditions, where  $\mu_0$  and  $\varepsilon_0$  are the vacuum permeability and permittivity. Quasinormal modes or resonant states are complex-frequency solutions of Eq. (2.1) with outgoing radiation boundary conditions [71–74]. In that case,  $\tilde{\omega}_j$  denotes the complex eigenfrequency of the  $j^{\text{th}}$  quasinormal mode. As a consequence of the complex eigenfrequency, quasinormal modes are characterized by a diverging amplitude in the far field. Conforming to the existing conventions [52], here and in the following, tilde ( $\sim$ ) is used to distinguish the modal fields from external or scattering fields.

The linear system of equations (2.1) is equivalent to a quadratic eigenproblem for the electric field:

$$\nabla \times \nabla \times \tilde{\mathbf{E}}_j(\mathbf{r}) - \varepsilon(\mathbf{r}, \tilde{\omega}_j) \frac{\tilde{\omega}_j^2}{c^2} \tilde{\mathbf{E}}_j(\mathbf{r}) = 0, \quad (2.2)$$

where  $c = 1/\sqrt{\mu_0 \varepsilon_0}$  is the velocity of light in vacuum. Following the usual scattering theory, we suppose that the system is illuminated by an incident field  $\mathbf{E}_b$ , which, in turn, is a solution of the wave equation (2.2) with only the background dielectric constant,  $\varepsilon_b$ . Splitting the total field in the incident and scattered components,  $\mathbf{E}(\mathbf{r}) = \mathbf{E}_b(\mathbf{r}) + \mathbf{E}_s(\mathbf{r})$ , the latter can be shown to satisfy the inhomogeneous wave equation in the presence of a source term proportional to the incident radiation, i.e.,

$$\nabla \times \nabla \times \mathbf{E}_s(\mathbf{r}) - \varepsilon(\mathbf{r}, \omega) \frac{\omega^2}{c^2} \mathbf{E}_s(\mathbf{r}) = \Delta\varepsilon(\mathbf{r}, \omega) \frac{\omega^2}{c^2} \mathbf{E}_b(\mathbf{r}). \quad (2.3)$$

<sup>2</sup>However, it is possible to extend our formalism to account for nonradiative-dissipation channels that model (modest amounts of) absorption as discussed in Ref. [47].



Limiting ourselves to the region where  $\Delta\varepsilon \neq 0$ , in the assumption that quasinormal modes  $\tilde{\mathbf{E}}_j$  form a complete basis, we can expand the scattered field on them:

$$\mathbf{E}_s(\mathbf{r}) = \sum_j a_j \tilde{\mathbf{E}}_j(\mathbf{r}). \quad (2.4)$$

The exact expression for the coefficients  $a_j$  depends on the incident field. Eventually, the knowledge of  $\mathbf{E}_s$  in a finite region is sufficient to extract the far-field properties of the scattered field, as it is described by the same Eq. (2.3), which becomes

$$\nabla \times \nabla \times \mathbf{E}_s(\mathbf{r}) - \varepsilon_b \frac{\omega^2}{c^2} \mathbf{E}_s(\mathbf{r}) = \Delta\varepsilon(\mathbf{r}, \omega) \frac{\omega^2}{c^2} [\mathbf{E}_b(\mathbf{r}) + \mathbf{E}_s(\mathbf{r})]. \quad (2.5)$$

At this point, we expand the input field over a set of incoming waves (or, more generally, ports),  $\mathbf{E}_b(\mathbf{r}) = \sum_{\alpha} s_{+\alpha} \mathbf{E}_{\alpha}^{(+)}$ , and the total electric field over a corresponding set of outgoing waves,  $\mathbf{E} = \sum_{\alpha} s_{-\alpha} \mathbf{E}_{\alpha}^{(-)}$ , whose detailed expression depends on the specific geometry of the system. The amplitude of each outgoing wave,  $s_{-\alpha}$ , can be written as the sum of a direct channel, which is directly proportional to the incoming amplitudes  $s_{+\alpha}$ , and a resonance-mediated channel, which is proportional to the quasinormal-mode amplitudes  $a_j$ . In turn, the latter amplitudes are related to the incoming field through Eq. (2.3). From the linearity of Maxwell's equations, it follows that all these relations can be written in terms of linear operators. This is the basis of the coupled-mode formalism, which we illustrate in the following.

### 2.2.2. Coupled-mode equations

Seeking a more general formulation, we write the characteristic equation of quasinormal modes, Eq. (2.1), as an eigenvalue problem for the effective "Hamiltonian"  $\Omega + i\Gamma$ ,

$$(\Omega + i\Gamma)\mathbf{a}_j = \tilde{\omega}_j \mathbf{a}_j, \quad (2.6)$$

where  $\mathbf{a}_j$  is the modal amplitude eigenvector associated with the complex eigenvalue  $\tilde{\omega}_j$ . The components of the vectors  $\mathbf{a}_j$  are interpreted as the coefficients of the expansion of the electric field in terms of quasinormal modes, which we do not necessarily assume to be orthogonal according to the standard Hermitian product. Here and in the following parts of the chapter, we assume the convention  $e^{i\omega t}$  for the temporal dependence of the field. Due to the inherently dissipative nature of quasinormal modes, the Hamiltonian operator  $\Omega + i\Gamma$  is non-Hermitian and it has been split into Hermitian and skew-Hermitian parts, which are expressed in terms of the two Hermitian operators  $\Omega$  and  $\Gamma$ . Using the same language as in Eq. (2.6), we relate the incoming and outgoing amplitudes of the electromagnetic field (which we express in vector form as  $\mathbf{s}_+$  and  $\mathbf{s}_-$ ) by means of a system of coupled-mode

equations, in line with the formalism by S. Fan et.al. [55, 63]:

$$i\omega \mathbf{a} = i(\Omega + i\Gamma) \mathbf{a} + K^\top \mathbf{s}_+ \quad (2.7)$$

$$\mathbf{s}_- = C \mathbf{s}_+ + D \mathbf{a}. \quad (2.8)$$

The operator  $C$  represents the direct-coupling channel, whereas the operators  $K$  and  $D$  account for coupling between quasinormal modes and the incoming and outgoing ports, respectively. In the convention that  $|\mathbf{a}|^2$  is interpreted as the energy in the mode, and  $|\mathbf{s}_\pm|^2$  the power in the ingoing or outgoing port,  $\Omega$  and  $\Gamma$  have units of frequency,  $K$  and  $D$  have units of square root of frequency, and  $C$  is dimensionless. Although in principle there might be infinitely many quasinormal modes and ports, for practical reasons we assume that the number of modes and ports is truncated to the finite values  $n$  and  $m$ , respectively. In this way, all the operators reduce to finite-size matrices. The set of Eqs. (2.7) and (2.8) is summarized by the scheme in Fig. 2.1.

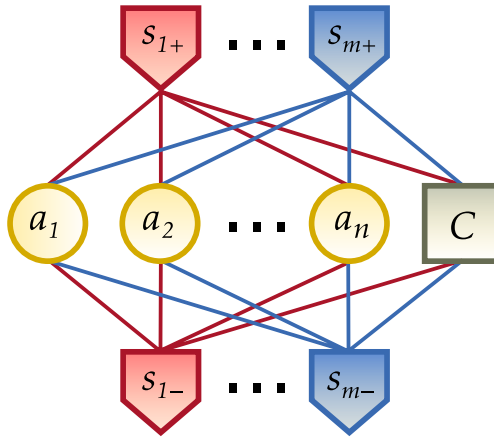


**Figure 2.1: Coupled-mode scheme:** Schematic of  $m$  ports coupled to  $n$  quasinormal modes with amplitudes  $a_j$  ( $j = 1, \dots, n$ ) and linked by a direct-coupling term  $C$ . The notation  $s_{p+}$  and  $s_{p-}$  ( $p = 1, \dots, m$ ) refers to the amplitude of incoming and outgoing waves, respectively.

As originally demonstrated in Refs. [55] and [63], some relations among the quantities that appear in Eqs. (2.7) and (2.8) can be directly deduced from some very general physical properties of the system. First, electromagnetic reciprocity and energy conservation imply that

$$K = D \quad (2.9)$$

and

$$\Gamma = \frac{1}{2} D^\dagger D, \quad (2.10)$$

respectively. Moreover, by comparing the dynamics described by Eqs. (2.7) and (2.8) with the time-reversed case and employing time-reversal symmetry, it can be shown that

$$CD^* = -D. \quad (2.11)$$

The system in Eqs. (2.7) and (2.8) has been extensively used to model the scattering properties of numerous photonic structures [56, 60, 61, 63, 66, 75], proving itself particularly valuable for investigating the physical mechanisms at the basis of various phenomena, such as the formation of Fano line shapes in the spectrum as a consequence of the interference between the resonant and the direct-coupling channels [55]. In all these cases, however, the number of modes included in the equations is limited to one or two. Then, in combination with the assumption that these modes obey certain symmetries (e.g., even/odd spatial symmetries), one can derive specific components of  $D$ . And the direct-coupling channel, if present, is accounted for by fitting a specific frequency-dependent background response obtained from independent numerical simulations of the spectrum (see, for instance, Refs. [55, 63, 66]). We will use such an approach in Ch. 3.

Nevertheless, the need for independent frequency-by-frequency simulations restricts the suitability of coupled-mode theory as a basic computational tool. Moreover, accurately fitting the direct-coupling background typically requires some additional assumptions which are difficult to interpret on physical grounds (for instance, the need for a frequency-dependent *effective* dielectric constant owing to the fact that the background reflection is caused by a structured system that is composed of different materials). In a broader sense, the actual separation between the resonant states and the frequency-dependent background is somewhat arbitrary, since the latter is also made up of a number of broad resonances associated with additional quasinormal modes. In the light of our assumption about the completeness of quasinormal modes (Sec. 2.2.1), we expect that by enlarging the set of electromagnetic modes, so as to include the resonances usually associated with the background, we could remove the need for fitting the direct-coupling background and treat all resonant states on equal grounds. In this way, in addition to getting a more transparent physical picture, we could also better elucidate the modal structure at the basis of resonant systems. In the following, we show that this strategy can be implemented, in a formalism that is easily scalable to multiple modes with varying decay rates.

### 2.2.3. Expansion of the scattering matrix

The scattering matrix of the system connects the amplitude of the outgoing waves with the amplitude of the incoming waves:

$$\mathbf{s}_- = \mathbf{S} \mathbf{s}_+. \quad (2.12)$$

Using the identity (2.9), it can be shown from Eqs. (2.7)–(2.8) that we have:

$$S = C - iD(\omega\mathbb{I} - \Omega - i\Gamma)^{-1}D^\dagger. \quad (2.13)$$

Here, we derive an expression for the expansion of the scattering matrix on quasinormal modes, on the basis of the system of Eqs. (2.7)–(2.8). To this purpose, in addition to the complex eigenfrequencies of the quasinormal modes,  $\tilde{\omega}_j$  ( $j = 1, \dots, n$ ), we also assume the knowledge of the asymptotic behaviour of the quasinormal-mode eigenfield in the output ports, which is equivalent to the knowledge of the relative complex amplitudes of the vectors

$$\mathbf{b}_j \doteq \mathbf{s}_-|_{\omega=\tilde{\omega}_j} = D\mathbf{a}_j. \quad (2.14)$$

For simplicity, we will refer to the vectors  $\mathbf{b}_j$  as the “scattering eigenvectors” of the system. As it is the case for all eigenproblems, the (complex) normalization constant of the eigenvectors can be set arbitrarily; however, as proven in appendix 2.B, the final expression for the scattering matrix does not depend on the choice of such a constant. As a consequence, our approach is inherently normalization-free, at variance with other works dealing with the expansion of the dyadic Green function, which require the quasinormal modes to be normalized in a specific fashion [72–74].

In practice, the complex eigenvalues and the scattering eigenvectors need to be computed by numerical eigensolvers. The specific method depends on the definition of the input–output ports, but, in general, it involves calculating the electric field at a point or on a surface in the far-field region of the system.

Since the matrix  $\Omega + i\Gamma$  is not Hermitian, the right eigenvectors alone are not orthogonal. However, as is known from the theory of complex Hamiltonians [76], right eigenvectors ( $\mathbf{a}_j$  in our case) form a biorthogonal basis together with left eigenvectors, which are defined by the equation

$$\mathbf{l}_j^\dagger(\Omega + i\Gamma) = \tilde{\omega}_j \mathbf{l}_j^\dagger. \quad (2.15)$$

To simplify the notation, we introduce the  $n \times n$  matrix  $A$  whose columns are the right eigenvectors  $\mathbf{a}_j$  and the corresponding matrix  $L$  of the left eigenvectors  $\mathbf{l}_j$ . With this new notation, Eq. (2.6) becomes:

$$(\Omega + i\Gamma)A = A\tilde{\Omega}, \quad (2.16)$$

with  $\tilde{\Omega}$  being the diagonal matrix of the complex eigenvalues  $\tilde{\omega}_j$ . Moreover, we define the  $m \times n$  matrix  $B$  whose columns are the vectors  $\mathbf{b}_j$ .

The complex Hamiltonian of Eq. (2.6) can then be expanded on the biorthogonal basis as follows [76]:

$$\omega\mathbb{I} - \Omega - i\Gamma = A(\omega\mathbb{I} - \tilde{\Omega})L^\dagger. \quad (2.17)$$

Even if the right eigenvectors are not orthogonal, they are however linearly independent [76]; thus, we can formally write  $L = (A^\dagger)^{-1}$ . Replacing Eq. (2.17)

into Eq. (2.13), we obtain the quasinormal-mode expansion of the scattering matrix,

$$S = C - iB \frac{1}{\omega \mathbb{I} - \tilde{\Omega}} \Lambda^{-1} B^\dagger, \quad (2.18)$$

where we define  $\Lambda \doteq A^\dagger A$  and we use the relation  $B = DA$ , which comes directly from Eq. (2.14). For all practical purposes, it is crucial to derive an expression for the matrix  $\Lambda$ . This latter matrix plays a fundamental physical role, because the amplitude and phase of its terms determine the oscillator strength of each resonance and affect the degree of interference among the modes, which, in turn, has been found responsible for the appearance of interesting spectral features, such as Fano line shapes [55] or the optical analogue of electromagnetically-induced transparency [66].

First of all, it can be shown that  $\Lambda$  is diagonal. This result follows from the symmetry of the complex Hamiltonian  $\tilde{\Omega} + i\Gamma$ , which can be proven by combining Eqs. (2.10) and (2.11). The same result can also be derived from the requirement that the resulting scattering matrix must be symmetric [63]. Next, by multiplying each side of Eq. (2.11) by  $A^*$  and after some algebraic manipulations, we obtain  $CB^* = -B\Lambda^{-1}(A^\dagger A)^*$ , which we can recast in the more compact form

$$CB^* + B\Lambda^{-1}Q^* = 0, \quad (2.19)$$

which defines the matrix  $Q = A^\dagger A$ .

By multiplying Eq. (2.16) by  $A^\dagger$  on the left, taking the difference with its Hermitian conjugate, and employing Eqs. (2.10) and (2.14), we arrive at

$$Q\tilde{\Omega} - \tilde{\Omega}^*Q = 2iA^\dagger\Gamma A = iB^\dagger B. \quad (2.20)$$

In general, the solution for  $Q$  cannot be written explicitly in terms of matrix products; however, it is straightforward to express it component-wise, as follows:

$$Q_{ij} = i \frac{b_i^\dagger b_j}{\tilde{\omega}_j - \tilde{\omega}_i^*}. \quad (2.21)$$

This latter equation allows us to clarify the physical meaning of Eq. (2.19), which is the principle of energy conservation. With the aid of Eqs. (2.18) and (2.21), it can be shown that Eq. (2.19) is equivalent to the condition

$$S^\dagger(\tilde{\omega}_j)b_j = 0. \quad (2.22)$$

From the inversion of the scattering matrix, on the other hand, we obtain that  $S^{-1}(\tilde{\omega}_j)b_j = 0$ , since quasinormal modes are defined as the self-sustaining solution of Maxwell's equations in the absence of any input radiation. Comparing the two results, it is clear that Eq. (2.19) guarantees that the scattering matrix is unitary at the modal eigenfrequencies, as required by energy conservation.

Equations (2.19) and (2.21) allow us to fully determine the matrix  $\Lambda$ , and, hence, the quasinormal-mode expansion of Eq. (2.18). However, a closer inspection of Eq. (2.19) reveals that the system has  $m \times n$  equations (the dimension of  $B$ ) and only  $n$  unknowns (the diagonal of  $\Lambda$ ). Thus, for a given direct coupling matrix  $C$ , the system is generally overdetermined and a solution is not always guaranteed to exist. From a different perspective, the direct matrix  $C$  cannot be chosen freely, but it must satisfy some constraints that depend on the properties of the resonant states. In practice, it might be difficult to choose a direct matrix with a simple analytical form and, at the same time, consistent with Eq. (2.19), especially when a large number of quasinormal modes is involved.

For all these reasons, it is essential to develop a general theory that encompasses also the case when the matrix  $C$  is an approximation of the exact direct-coupling matrix. To this end, instead of looking for an exact solution of Eq. (2.19), we search for an approximate solution in the least-square sense. To be more precise, having defined the vectors  $\mathbf{x}_j$  ( $j = 1, \dots, n$ ) as the columns of the matrix

$$X = CB^*(Q^*)^{-1}, \quad (2.23)$$

we look for the diagonal matrix  $\Lambda$  in Eq. (2.19) whose diagonal terms,  $\lambda_j$ , minimize the objective function

$$f(\lambda_1, \dots, \lambda_n) = \sum_{j=1}^n |\lambda_j \mathbf{x}_j + \mathbf{b}_j|^2. \quad (2.24)$$

This reformulation of the problem does not affect the generality of the theory, because, if Eq. (2.19) has an exact solution, then such solution must coincide with the least-square one [77].

A simple calculation of the stationary points of the objective function leads to the result  $\lambda_j = -\mathbf{x}_j^\dagger \mathbf{b}_j / (\mathbf{x}_j^\dagger \mathbf{x}_j)$ , which, once replaced into Eq. (2.18), provides us with the final expression

$$S = C + i \sum_{j=1}^n \frac{\mathbf{x}_j^\dagger \mathbf{x}_j}{\mathbf{x}_j^\dagger \mathbf{b}_j} \frac{\mathbf{b}_j \mathbf{b}_j^\dagger}{\omega - \bar{\omega}_j}. \quad (2.25)$$

Equation (2.25), together with Eqs. (2.23) and (2.21), is the desired expansion of the scattering matrix and it represents the main result of this chapter. Using Eq. (2.23), the expansion coefficients as they appeared in Eq. (2.18) can be explicitly written as

$$\frac{1}{\lambda_j} = -\frac{\mathbf{x}_j^\dagger \mathbf{x}_j}{\mathbf{x}_j^\dagger \mathbf{b}_j} = -\frac{\sum_{nn'} Q^{-1}_{nj} (Q^{-1}_{n'j})^* \mathbf{b}_n^\dagger C^\dagger C \mathbf{b}_{n'}}{\sum_n Q^{-1}_{nj} \mathbf{b}_n^\dagger C^\dagger \mathbf{b}_j}. \quad (2.26)$$

The denominator of the coefficient can be regarded as a modified inner product that renormalizes the scattering eigenvectors in order to guarantee the total scattering matrix to be unitary. In the limiting case when the off-diagonal elements of  $Q$  are negligible, the expression in Eq. (2.25) reduces as shown in appendix 2.A. In addition, in appendix 2.B we also show that the result in Eq. (2.25) is independent of the normalization of the scattering eigenmodes.

Indeed, Eqs. (2.25) and (2.26) allow determining the full scattering matrix from only the knowledge of the scattering eigenvectors  $\mathbf{b}_j$  (which can often be obtained from numerical calculations of a system's quasinormal modes) together with the background scattering matrix  $C$ . Importantly, the above theory unambiguously determines the relative phases with which different modes are excited by an incident wave, and with which they interfere in output waves. These phases are connected to the background scattering through energy conservation and time-reversal symmetry. We will use this theory in the next chapter, by assuming a simple model for  $C$ . In the following examples, we however show that the method can also be used without external assumption of  $C$ , by extending the method to include a large number of modes that together form a basis that is assumed to be complete and responsible for a system's broadband response.

## 2.3. Applications

### 2.3.1. Photonic crystal slab

As an illustrative example, we consider a photonic crystal slab composed of a square lattice of circular holes etched in a silicon membrane ( $\epsilon = 12.1$ ). Indicating with  $a$  the lattice constant, we assume the slab thickness and the hole radius  $t = 0.4a$  and  $r = 0.2a$ , respectively. For normally incident light polarized along one of the lattice axes, we can limit ourselves to a single polarization of light; moreover, in the range of frequencies  $\omega < 2\pi/a$ , only the zeroth order of diffraction is available. As a consequence, the system can be effectively described with two ports, corresponding to the plane waves  $E_{1,+} = s_{1,+} e^{-i\omega z/c}$  and  $E_{2,+} = s_{2,+} e^{i\omega z/c}$ , propagating along the normal direction to the slab, which we indicate as the  $z$  axis.

In Fig. 2.2a we show the complex eigenfrequencies of the quasinormal modes of the system for normally incident light. Although all the modes represent equally valid solutions of the same characteristic equation (2.2) and they are treated on equal grounds in the expansion of the scattering matrix (2.25), it is useful from a physical point of view to distinguish between two categories of quasinormal modes: weakly dissipating quasi-guided modes and leaky modes with much larger radiation rates. As it appears from Fig. 2.2a, the threshold between the two families can be set around  $\text{Im } \tilde{\omega} \approx 10^{-2} (2\pi c/a)$ , with a difference of more than one order of magnitude between the corresponding imaginary parts of the eigenfrequencies. The

leaky modes ( $\text{Im } \tilde{\omega} > 10^{-2} 2\pi c/a$ ) have strong similarities with the Fabry-Pérot resonances of a homogeneous dielectric slab with an average refractive index  $n_{\text{av}}$ , displaying a roughly constant frequency spacing of the order of the free spectral range  $\delta\omega = \pi c/(n_{\text{av}}t)$ . The deviation from the equal spacing behaviour grows when the frequency increases, due to the wavelength becoming more sensitive to the dielectric-function inhomogeneity in the system [60].

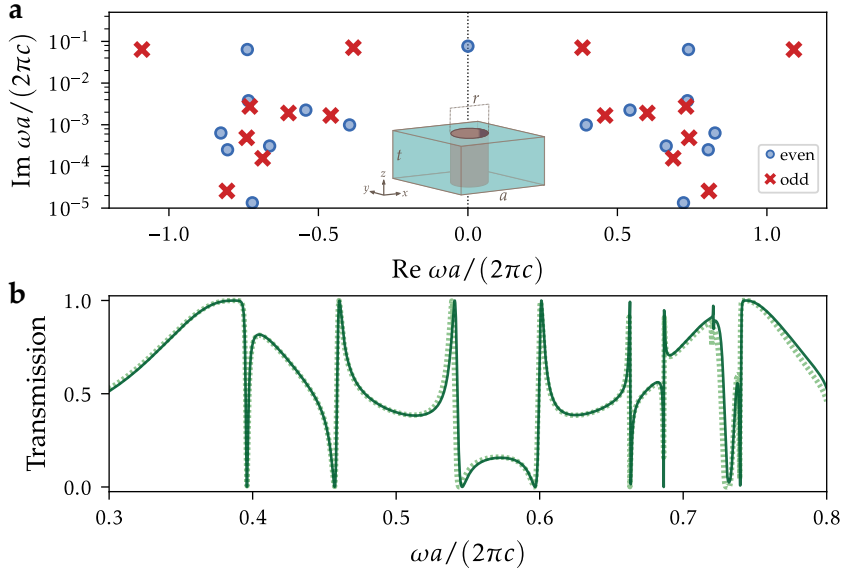


**Figure 2.2: Application of the theory to a photonic crystal slab:** The slab is composed of a square lattice of air holes etched in a suspended silicon membrane. **a.** Real and imaginary part (log scale) of the quasinormal-mode complex eigenfrequencies, together with the corresponding symmetry of the modes (even, odd) by inversion with respect to the slab middle plane. The unit cell of the structure is represented in the inset ( $t = 0.4a$  and  $r = 0.2a$ ). **b.** Transmission intensity computed by expanding the scattering matrix on the quasinormal modes (green solid line), compared with the exact result by the Fourier modal method (green dashed line) [78].

Quasi-guided modes can be easily computed in various ways, including, e.g., frequency-domain [73] or time-domain [68, 72] methods, or by determining the poles of the scattering or transmission coefficient in the complex frequency plane [53]. These techniques can also be combined, in order to exploit specific advantages. For instance, in the present example, the modes with  $\text{Re } \tilde{\omega}_j > 0$  have been computed by solving a linearised version of the eigenproblem in Eq. (2.2) with a commercial finite-element package (COMSOL Multiphysics 5.2), whereas, for better numerical accuracy, leaky modes have been obtained separately by looking for the complex-frequency poles of the transmission amplitude computed with the Fourier modal method using



a freely available solver [78]. Since the wave equation (2.2) is second order in the frequency, for each quasinormal mode with  $\text{Re } \tilde{\omega}_j > 0$  there exists a corresponding state with  $\tilde{\omega}_{j'} = -\tilde{\omega}_j^*$  and  $\tilde{\mathbf{E}}_{j'}(\mathbf{r}) = \tilde{\mathbf{E}}_j^*(\mathbf{r})$  [67], which has been included in the calculations, raising the total number of quasinormal modes under consideration in this example to  $n = 33$ . Due to numerical difficulties in performing the calculations near the imaginary axis of the complex-frequency plane, the decay rate of the  $\text{Re } \tilde{\omega}_j = 0$  mode has been estimated using the analytical formula for a homogeneous dielectric slab with an averaged refractive index [71].

The asymptotic behaviour of the eigenfield is entirely determined by the inversion symmetry of the system with respect to the middle plane of the slab. Since the electric field amplitude is either even or odd with respect to the inversion, as indicated in Fig. 2.2a, we can directly assume the scattering eigenvectors

$$\mathbf{b}_\pm = \frac{1}{\sqrt{2}} \begin{bmatrix} 1 \\ \pm 1 \end{bmatrix}. \quad (2.27)$$

for even (“+”) and odd (“−”) modes. As we already remarked, since the scattering matrix expansion is independent of the eigenfield normalization, any other choice of the normalization in Eq. (2.27) would have been equally suitable. Finally, in agreement with our assumption about the completeness of quasinormal modes for photonic systems, we take the  $2 \times 2$  identity matrix as the direct-coupling matrix

$$\mathbf{C} = \mathbb{I}_{2 \times 2}. \quad (2.28)$$

In this way, we can derive the expression of the scattering matrix of the photonic crystal slab by applying Eq. (2.25) with the complex eigenfrequencies of Fig. 2.2a and the scattering eigenvectors of Eq. (2.27). The transmission intensity obtained from the resulting scattering matrix is shown by the solid green curve in Fig. 2.2b, and it is compared with an independent calculation by the Fourier modal method (dashed green line) [78]. The agreement between the curves is excellent, highlighting the validity of the quasinormal-mode expansion of the scattering matrix. The comparison confirms that the first-principle description of the optical properties of the system provided by the theory is complete and accurate; moreover, we stress that such a description does not require any *ad-hoc* assumptions on the direct coupling channel and is based only on the complex eigenfrequencies of the quasinormal modes.

### 2.3.2. Asymmetric photonic crystal structure

A specific advantage of the scattering-matrix expansion is the straightforward applicability to generic systems lacking any particular symmetry. In order to illustrate this point, we consider a square lattice of L-shaped void structures partially patterned in a silicon slab. The shape and size of the structures are schematised in the inset of Fig. 2.3a. The height of the patterned region ( $h =$

$0.2a$ ) is one half of the total thickness of the slab ( $t = 0.4a$ ), resulting in a configuration which is not symmetric by inversion along  $z$ . Moreover, for incident light polarized along one of the lattice main axes, the transmitted and reflected radiation will include a cross-polarized fraction. Therefore, we can model the system by defining four ports, corresponding to plane waves propagating above and below the slab and polarized along the two in-plane crystal axis (which we indicate as  $x$  and  $y$ ). In agreement with the assumption that quasinormal modes form a complete basis, we also assume the identity matrix as the direct-coupling matrix, i.e.,  $C = \mathbb{I}_{4 \times 4}$ .

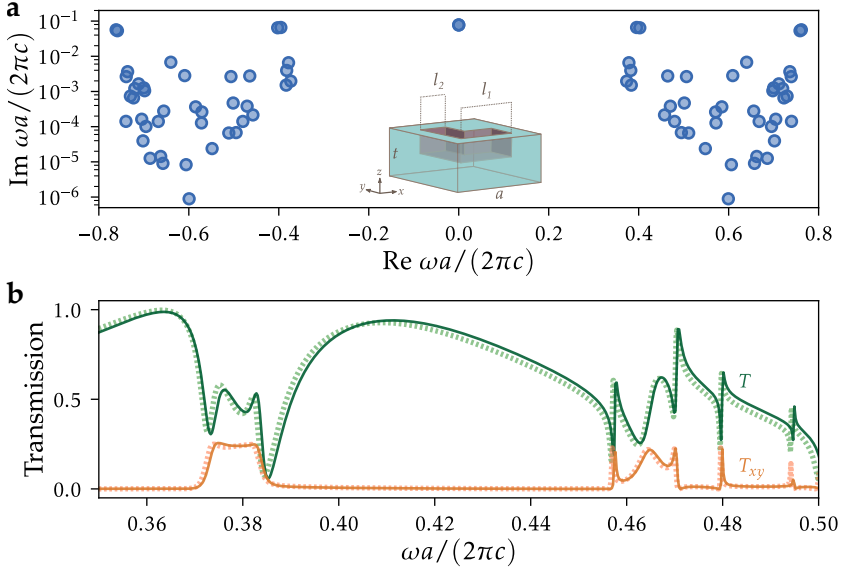


**Figure 2.3: Application of theory to an asymmetric photonic crystal structure:** **a.** Circles: real and imaginary part (log scale) of the quasinormal-mode eigenfrequencies of a square lattice of L-shaped patterned structures in a silicon membrane. The unit cell of the structure is represented in the inset ( $t = 0.4a$ ,  $l_1 = 0.6a$ , and  $l_2 = 0.3a$ ). Note that the structure is not symmetric by inversion along the  $z$  axis. **b.** Total transmittance,  $T$  (green), and cross-polarized transmittance,  $T_{xy}$  (orange), computed by expanding the scattering matrix on the quasinormal modes (solid lines), compared with the exact result by the Fourier modal method [78] (dashed lines).

The complex eigenfrequencies of the quasinormal modes, computed with the finite-element method (COMSOL Multiphysics 5.2), are presented in Fig. 2.3a. Even in this case we can distinguish between a set of quasi-guided modes and a set of roughly equispaced leaky modes with a larger dissipation rate. Similarly to the previous example, the decay rate of the pair of modes with  $\text{Re } \tilde{\omega}_j = 0$  has been estimated using the analytical results for a homogeneous dielectric slab, and, moreover, we have also explicitly included the modes with  $\tilde{\omega}_{j'} = -\tilde{\omega}_j^*$ . However, in this case the scattering

eigenvectors  $\mathbf{b}_j$  must be obtained from the asymptotic behaviour of the calculated quasinormal-mode eigenfield (see appendix 2.D). To this purpose, we consider the  $x$  and  $y$  electric-field components of each quasinormal mode in two planes located above and below the silicon slab at a sufficiently large distance to make the near-field contributions negligible. The specific choice of the distance does not affect the results, since only the relative amplitudes among the field components are relevant for the theory. It is interesting to note that the scattering eigenvector can also be computed with a near-to-far-field transformation of the quasinormal modes [79].

From the expansion of the scattering matrix in Eq. (2.25), we computed the total transmission intensity,  $T$ , and the cross-polarized transmission intensity,  $T_{xy}$  (i.e., the intensity of  $x$ -polarized transmitted light for  $y$ -polarized incident radiation). These quantities are shown (solid lines) in Fig. 2.3b and they are compared with the exact results (dashed lines) obtained from the Fourier modal method [78]. There is good agreement between the curves, especially in the vicinity of multiple narrow resonances, further confirming the validity of our approach as a predictive tool for computing the scattering matrix of electromagnetic systems. The small deviation from the exact result in the high-frequency region of Fig. 2.3b is likely due to the lower number of leaky modes included in this example with respect to the case of Sec. 2.3.1. The large radiative width of leaky modes (with a quality factor of the order of 10) implies that additional states beyond the frequency range under consideration may still have a small effect on the transmission in Fig. 2.3b. To corroborate this hypothesis, we verified that the agreement with simulation data can be further improved when an additional pair of leaky modes at  $\text{Re } \tilde{\omega}_j \simeq 1.1(2\pi c/a)$  is included in the scattering matrix expansion (see appendix 2.C for a short discussion on the convergence).

Computing the eigenvalues of Fig. 2.3a with the finite-element method takes about one hour on a multiprocessor workstation. By comparison, on the same workstation the time required by a single frequency-point calculation of the transmission using the same finite-element solver and the same mesh is about three minutes, implying that computing the transmission spectrum of Fig. 2.3b (roughly 1000 points) would require about 50 hours with the finite-element method. This 50-fold reduction of computational time highlights the computational advantage of modal methods over frequency-domain full-wave simulations using the same electromagnetic solver.

## 2.4. Discussion and conclusions

In this chapter, we derived a general approach to expand the scattering matrix of optical systems on the basis of quasinormal modes and we validated it with illustrative examples. The theory is directly scalable to any number of modes and input–output channels. This particular feature allows us to treat all resonant modes on equal grounds, going beyond the traditional partition

of a system in a small set of narrow modes and a frequency-dependent background fitted from simulation data. In this way, we achieve a more transparent picture of the modal structure of the system and, at the same time, we solve the ambiguity that could arise in defining the background channel in complex optical structures with a wide distribution of resonance widths. Eliminating the need for fitting a frequency-dependent background allows us to turn the quasinormal-mode expansion into a first-principle and self-consistent computational tool, which only requires the knowledge of the complex eigenfrequencies and the far-field behaviour of the electromagnetic modes.

Creating artificial optical materials is an important goal in current nanophotonic research [80]. Such materials allow us to precisely control the intensity, phase, and polarization of scattered and transmitted light and to enhance light-matter interaction at the nanoscale. Spatial arrangements of optical resonators have been used, for instance, to realize high-contrast gratings [81], photonic metasurfaces [59, 82, 83], and zero-refractive-index metamaterials [84]. When the constituting optical resonators are chiral, several intriguing effects can be observed, such as the asymmetric transmission of circularly and linearly polarized light [85, 86]. Even for a single optical resonator, like a multilayered particle, the interference of different resonant states give rise to interesting phenomena, such as, for instance, the optical analogue of electromagnetically induced transparency and superscattering [58] and the formation of scattering dark states [56, 57]. Multiple-resonance effects can also be exploited to tailor the scattering cross section of a scatterer, making it transparent to an outside observer [87]. Furthermore, hybrid photonic-plasmonic systems allow us to tailor the interaction with quantum emitters [88, 89] and evidence polaritonic effects [90]. All these optical systems are typically characterized by a complex spectral structure, due to the presence of multiple electromagnetic modes coupled to the environment via various incoming and outgoing channels.

Typically, as an alternative to modal expansion, the scattering matrix and the derived quantities (such as transmission or scattering intensities) can also be computed with a full-wave solver on a frequency-by-frequency basis. The expansion on quasinormal modes, however, offers several advantages over direct frequency-domain computations on several aspects. In the first place, modal methods allow for a significant reduction of computational times [69, 74], especially when the presence of narrow resonances dictates a very fine frequency resolution. The computationally most demanding phase of the modal expansion is the calculation of the quasinormal modes. After that, the method allows us to arbitrarily reduce the frequency resolution at no further computational cost.

More importantly, the scattering matrix expansion provides a more complete amount of information and offers a deeper physical insight with respect to a frequency-by-frequency calculation. This aspect is especially helpful, for instance, in the process of designing and optimizing optical materials.

Building upon the connection between quasinormal modes and scattering properties established by the theory, instead of looking for a specific spectral feature among a large number of simulated spectra with varying parameters, one could equivalently search for a quasinormal mode with specific attributes. This strategy is generally faster, more transparent, and more suggestive of the relation among the physical parameters. For all these reasons, the quasinormal-mode expansion of the scattering matrix is particularly suitable for investigating the physical mechanisms at the heart of highly structured spectra, such as those arising from the interference of several closely spaced modes. Indeed, as we noted above, this is the case for many photonic systems which are currently the subject of intense research efforts. At the same time, the theory also represents a powerful and predictive tool for the first-principle calculation of the scattering behaviour of general physical systems.

## APPENDICES

### 2.A. Case of orthogonal modes

If the scattering amplitudes of the quasinormal modes are orthogonal (i.e.,  $\mathbf{b}_i^\dagger \mathbf{b}_j = 0$  for  $i \neq j$ ), or the spectral overlap between the modes can be neglected, the coupling matrix  $Q$  of Eq. (2.21) becomes diagonal. The least-square solutions of Eq. (2.19) can, then, be written as  $\lambda_j = -\mathbf{b}_j^\dagger C^\dagger \mathbf{b}_j / (2\text{Im } \tilde{\omega}_j)$ . As a result, the scattering-matrix expansion of Eq. (2.25) assumes the simpler expression:

$$S = C + 2i \sum_{j=1}^n \frac{\text{Im } \tilde{\omega}_j}{\omega - \tilde{\omega}_j} \frac{\mathbf{b}_j \mathbf{b}_j^\dagger}{\mathbf{b}_j^\dagger C^\dagger \mathbf{b}_j}. \quad (2.A.1)$$

### 2.B. Free choice of amplitude normalization

Here, we show that the result in Eq. (2.25) is independent of the normalization of the scattering amplitudes of the quasinormal modes. To this end, we consider a different set of amplitudes  $\mathbf{b}'_j$ , which differ from the original  $\mathbf{b}_j$  by some complex multiplicative constants  $\phi_j$  (which can be different for different modes):

$$\mathbf{b}'_j = \phi_j \mathbf{b}_j. \quad (2.B.1)$$

Introducing the diagonal matrix  $\Phi = \text{diag}(\phi_j)$  and the matrix  $Q'$ , defined by the expression in Eq. (2.21) with the modified eigenvectors, it is straightforward to verify that  $Q = \Phi^{*-1} Q' \Phi^{-1}$ . In a similar fashion, we observe that Eq. (2.19) retains exactly the same form provided that  $Q$ ,  $B$ , and  $\Lambda$  are replaced by  $Q'$ , the column matrix of the new eigenvectors,  $B'$ , and  $\Lambda' = \Phi \Lambda \Phi$ , respectively. Then, substituting these replacements in Eq. (2.18), we obtain that:

$$S = C - iB \frac{1}{\omega \mathbb{I} - \tilde{\Omega}} \Lambda^{-1} B^\dagger = C - iB' \frac{1}{\omega \mathbb{I} - \tilde{\Omega}} \Lambda'^{-1} B'^\dagger, \quad (2.B.2)$$

i.e., the expansion of the scattering maintains exactly the same formal expression independently of the choice of the eigenvector normalization constants.

### 2.C. Convergence

In Fig. 2.C.1, we illustrate the effect of including an additional pair of leaky modes to the set employed in Sec. 2.3.2 and originally displayed in Fig. 2.3. The additional modes, which are highlighted with an arrow in Fig. 2.C.1a, have been computed from the complex-frequency poles of the transmission amplitude with the Fourier modal method [78]. As it can be seen from Fig. 2.C.1c, the agreement between the total transmission predicted from our theory (green solid curve) and the simulated data (dashed curve) is further

improved with respect to Fig. 2.3, in agreement with the considerations on the completeness of the quasinormal-mode basis.

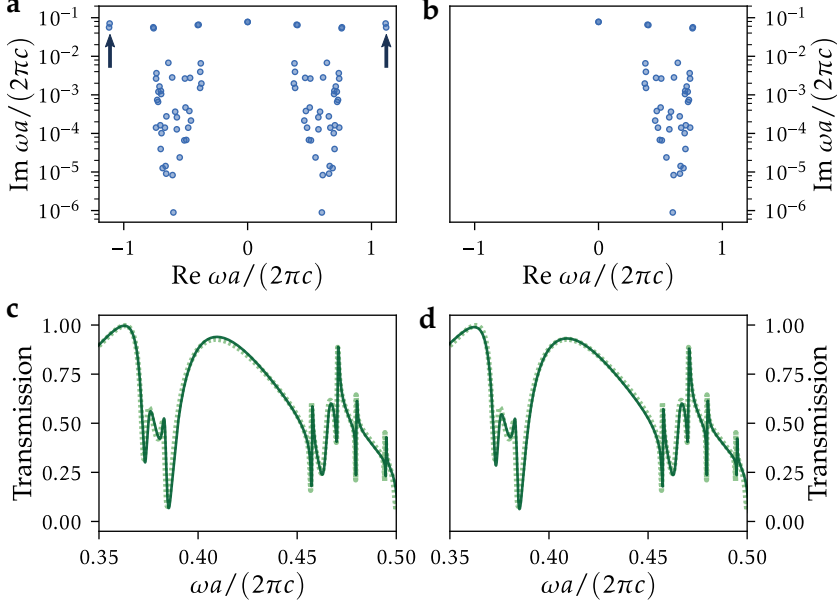


**Figure 2.C.1: Effects of addition and removal of modes:** a, b. Real and imaginary part (log scale) of different sets of the modal eigenfrequencies for the system considered in Sec. 2.3.2 in the main text. c, d. Comparison of the total transmission computed by the quasinormal-mode expansion (solid green curve) with the exact result (dashed curve). Curves in c and d refer to the choices of the modes in a and b, respectively.

Incidentally, we notice that other choices of the set of electromagnetic modes could provide comparable accuracy in the prediction of the transmission properties. For instance, in Fig. 2.C.1b and d we show that, in this particular example, excluding the modes with  $\text{Re } \tilde{\omega}_j < 0$  [see Fig. 2.C.1b] leads to an excellent agreement with the exact simulated data [Fig. 2.C.1d], without the need for including the additional pair of leaky modes discussed beforehand. The accuracy is probably due to the fact that the set of leaky modes ( $\text{Im } \tilde{\omega}_j > 10^{-2} a / (2\pi c)$ ) in Fig. 2.C.1b is clearly symmetric with respect to the small frequency range considered in Fig. 2.C.1d, suggesting that, in some cases, the convergence behaviour of the quasinormal-mode expansion could be enhanced by a suitable choice of the modes.

## 2.D. Electric field amplitudes of quasinormal modes

For illustration purposes, we also show in Fig. 2.D.1a and b a plot of the amplitude of the electric field of two quasinormal modes selected from those of

Fig. 2.3a in the main text, computed with the finite-element method (COMSOL Multiphysics 5.2).

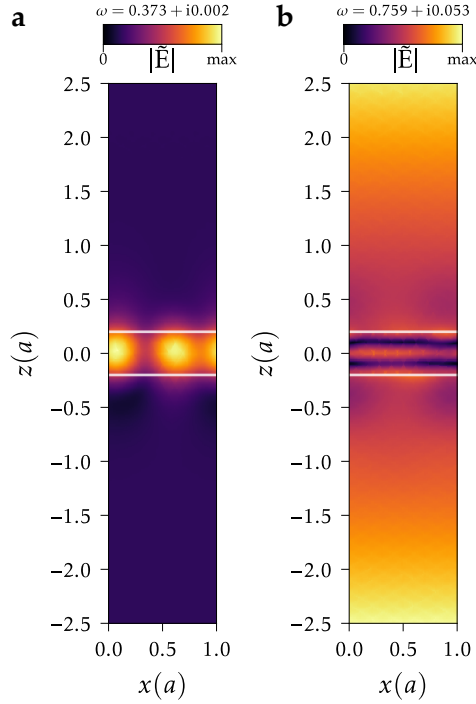


**Figure 2.D.1: Mode fields:** Amplitude of the electric field of two quasinormal modes selected from those of Fig. 2.3a in the main text. The plot shows a region of the  $xz$  plane along the edge of the unit cell close to the long side of the L-shaped structure ( $y = 0$ ). The complex frequencies of the modes are: **a**  $\omega a/(2\pi c) = 0.373 + i0.002$ , and **b**  $\omega a/(2\pi c) = 0.759 + i0.053$ .

The corresponding complex frequencies are indicated in the figure. The plot displays a region of the  $xz$  plane on the edge ( $y = 0$ ) of the unit cell of the periodic photonic structure (see the schematic in Fig. 2.3). The divergent far-field behaviour of the highly radiative quasinormal mode (Fig. 2.D.1b) is clearly recognizable.



# 3

## ASYMMETRIC TRANSMISSION IN CHIRAL PHOTONIC CRYSTALS

*“Nothing is so stifling as symmetry. Symmetry is boredom, [...] There is something more terrible than a hell of suffering – a hell of boredom.”*

— Victor Hugo, *Les Misérables*, 1862

*In this chapter, we investigate the origin and limit of the phenomenon of asymmetric transmission (AT) in chiral photonic systems. We observe that AT is strongly related to the far-field properties of eigenmodes of the system. We find that the resonant chiral phenomenon of AT is related to, and is bounded by, the non-resonant scattering properties of the system. A fundamental limit to the maximum AT possible for a single mode in any chiral resonator is determined using the principle of reciprocity. Finally, a design route for a highly chiral dielectric photonic crystal structure that reaches this fundamental limit for AT is proposed.*

### 3.1. Introduction

A strong chiral response is essential for realizing devices that can manipulate the polarization of light. Natural chiral materials rely on bulk properties such as birefringence, resulting in thick and bulky devices for polarization control. Much stronger chirality can be realized by exploiting the interaction of light with artificial nanostructures [92–94]. Such interactions are observed to be enhanced through local resonances such as those supported by plasmonic antennas [95, 96], periodically structured dielectric waveguides [97], etc. Arrangements of sub-wavelength-sized optical scatterers, called metasurfaces, are known for their exotic light-steering properties and polarization-dependent response [82, 98]. A better understanding of light-matter interaction at the nanoscale will help us to realize optical metasurfaces with designable vectorial electromagnetic near and far fields. Polarization-manipulating nanostructures are also important for realizing compact and/or on-chip polarization rotators, wave plates and polarizing beam splitters [83, 99–102].

Out of the chiroptical responses considered in Sec. 1.4, an extreme possible consequence of the chirality of a system is asymmetric transmission (AT), the difference in total transmittance when light with a certain polarization impinges from opposite sides of the system [85]. While it is possible to realize systems that radiate asymmetrically in opposite directions by breaking mirror symmetry in the propagation direction [103], the phenomenon of AT however requires a strongly chiral response.

Notably, when an emitter is placed in asymmetrically transmitting systems, this strong chirality also implies a significant difference between the polarizations of the light emitted in opposite sides of the system. Realization of AT in nanostructures thus relates directly to potential functionalities such as polarization control of spontaneous emission [104], spin-dependent light emission [105, 106] and enantioselective sensing [107]. There has been a considerable number of experimental attempts at realizing strong chirality in nanostructures. Several of these have been shown to offer AT for circularly polarized light using both metallic [108–111] and dielectric [112, 113] structures. However, to realize AT for linearly polarized light is significantly more challenging, as it strictly requires broken mirror symmetry in the propagation direction [114]. So far, attempts at realizing AT for linearly polarized light have been restricted mainly to metallic structures [86, 115–118]. Important open questions remain, like how to introduce an efficient symmetry breaking, what is the maximum AT that can be achieved, and how to design structures that can offer this maximum AT.

In this chapter, we investigate in detail the AT for linearly polarized light in dielectric chiral resonators. We show that the quasinormal modes of the system can be used to predict the AT for any system. We develop a theoretical formalism to find structures that can offer very high AT. Comparing full-field

simulations to theory based on the previous chapter, the origin and limits of AT are explored in terms of the properties of the quasinormal modes of the system. We uncover an important relation between the AT, which is a resonant phenomenon, and the direct reflectivity, which is a non-resonant property of the system. This relation, derived from the principle of reciprocity, creates a fundamental limit for AT in any chiral resonator. Following an optimization strategy to conform to this result, an example design for a photonic crystal structure with subwavelength thickness that can offer AT as high as 85% is proposed.

### 3.2. On the origin of asymmetric transmission in resonant systems

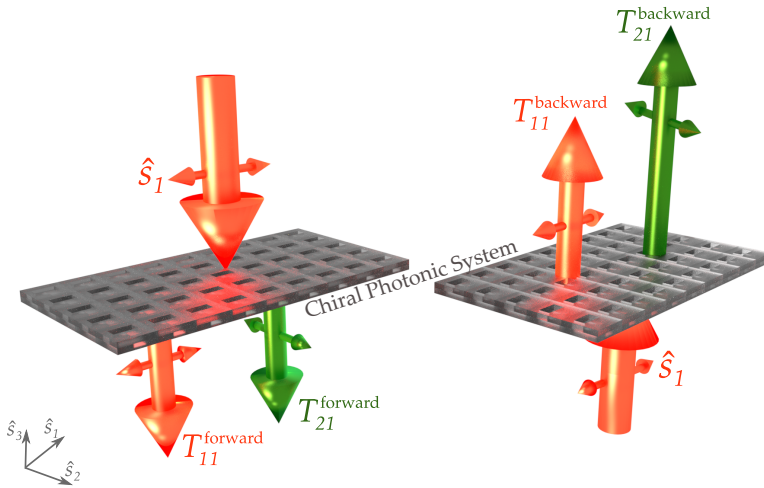


**Figure 3.1: Concept of AT:** Linearly polarized ( $\hat{s}_1$ -polarized) light is incident from opposite sides of a chiral photonic system.  $T_{11}$  and  $T_{21}$  are the transmittances of the electric field component parallel and orthogonal to  $\hat{s}_1$ , respectively. AT is the difference between the total transmittances in the two directions.

Figure 3.1 illustrates the concept of AT in chiral systems. Linearly polarized light is normally incident on the system in the forward direction (top-to-bottom direction in the figure). We denote the polarization of the incident beam as  $\hat{s}_1$  and the orthogonal polarization component as  $\hat{s}_2$ . The transmitted electric field of light can, in principle, contain both components. For  $\hat{s}_1$ -polarized incident light with electric field  $E_1^{in}$ , the complex forward transmission coefficients corresponding to the two electric field components along

$\hat{s}_1$  and  $\hat{s}_2$  in the transmitted light can be defined as  $t_{11}^f = (\hat{s}_1 \cdot \mathbf{E}^{\text{tr}}) / E_1^{\text{in}}$  and  $t_{21}^f = (\hat{s}_2 \cdot \mathbf{E}^{\text{tr}}) / E_1^{\text{in}}$ , where  $\mathbf{E}^{\text{tr}}$  is the total transmitted electric field. The respective transmittances, i.e., the ratios of the transmitted intensities and the incident intensity, are then  $T_{11}^f = |t_{11}^f|^2$  and  $T_{21}^f = |t_{21}^f|^2$ . For  $\hat{s}_1$ -polarized incidence, the total transmittance in the forward and backward direction can be respectively expressed as

$$T_1^f = T_{11}^f + T_{21}^f, \quad (3.1)$$

$$T_1^b = T_{11}^b + T_{21}^b. \quad (3.2)$$

Asymmetric transmission is the difference in the total transmittances in the two directions for polarized light and can be represented by

$$AT = |T_1^f - T_1^b|. \quad (3.3)$$

For reciprocal materials, a relation exists among transmittances in forward and backward directions such that [114, 118]:

$$T_{11}^f = T_{11}^b, \quad T_{22}^f = T_{22}^b, \quad T_{12}^f = T_{21}^b, \quad T_{21}^f = T_{12}^b. \quad (3.4)$$

Thus, using Eqs. (3.2) and (3.4) in Eq. (3.3), we can write AT as the difference in the orthogonal transmittances for two mutually perpendicular polarized incidences in a given direction. i.e.,

$$AT = |T_{12}^f - T_{21}^f|, \quad (3.5)$$

where  $T_{ij}^f = |(\hat{s}_i \cdot \mathbf{E}^{\text{tr}}) / E_j^{\text{in}}|^2$ .

In the following, we probe the origin of AT in chiral systems. Even though our conclusions and methodology apply to any general photonic system, we will now illustrate them with a specific example, a dielectric bilayer photonic crystal slab. We consider light that propagates perpendicular to the plane in which the structure is periodic. A unit cell of the 2-D periodic structure is shown in the inset of Fig. 3.2b. It is composed of two rectangular air holes stacked in mutually perpendicular fashion in a high-index ( $n = 3.48$ ) material. The orthogonal arrangement of holes breaks mirror symmetry in the propagation direction ( $z$  axis in the inset). Here, without loss of any generality, we choose  $\hat{s}_1$  and  $\hat{s}_2$  along the geometrical  $x$  and  $y$  axes, respectively. Finite element method (FEM) simulations (COMSOL Multiphysics 5.2) are used to calculate various transmittances  $T_{xx}$ ,  $T_{yx}$ ,  $T_{xy}$  and  $T_{yy}$  of the structure in a given frequency range. In Fig. 3.2a,  $T_{xx}$  and  $T_{yx}$  (violet and orange dashed lines, respectively) are the simulated parallel and orthogonal transmittances for  $x$ -polarized incident field.  $T_{xy}$  and  $T_{yy}$  (green and pink dashed lines) denote the simulated orthogonal and parallel transmittances, respectively, for a  $y$ -polarized incident field. The parallel transmittances for both incident polarizations,  $T_{xx}$  and  $T_{yy}$ , coincide over the entire frequency range. However, there

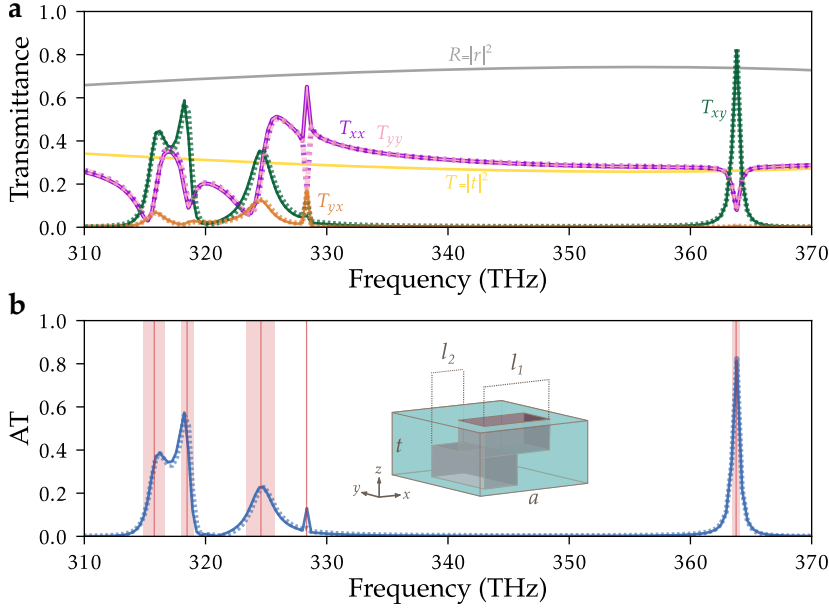


**Figure 3.2: Transmission spectra:** Various transmittances (a) and AT (b) as a function of frequency of the linearly polarized ( $x$  or  $y$  polarized) incident light, propagating in positive  $z$  direction. Transmittances  $T_{xx}$ ,  $T_{yx}$ ,  $T_{xy}$ ,  $T_{yy}$  and AT are shown as violet, pink, green, orange and blue curves, respectively. Dashed lines and solid lines correspond to the FEM simulation data and theoretically predicted values, respectively. Gray and yellow lines represent the calculated background reflectance and transmittance, respectively, for an effective uniform slab (see Sec. 3.3). Red vertical-lines and shaded areas, respectively, correspond to the calculated real parts and linewidths of the eigenfrequencies of the structure for zero parallel wave vector. The inset in panel b shows a unit cell of the proposed structure ( $t = 0.5a$ ,  $l_1 = 0.6a$  and  $l_2 = 0.3a$ ).

is a significant difference between the spectra of orthogonal transmittances  $T_{yx}$  and  $T_{xy}$  at certain frequencies. The AT spectrum for an  $x$  (or  $y$ ) polarized incident light is calculated from the simulation results using Eq. (3.5) and shown as a dashed blue line in Fig. 3.2b.

As is evident from the figure, the AT spectrum has pronounced features around certain frequencies. The resonant nature of this chiral response hints at a connection to the resonant modes of the structure. We calculate the eigenfrequencies of the structure for a parallel wavevector of zero using FEM simulations. Red vertical lines in Fig. 3.2b correspond to the real parts of the eigenfrequencies and light-red shaded areas show the linewidths of these modes. These simulations reveal that the resonances in the AT spectrum indeed coincide with the real parts of the eigenfrequencies of the structure, indicating a strong relation between the AT and the complex-frequency modes of the structure. With this understanding of the origin of AT, we now apply the scattering-matrix formalism developed in Ch. 2 to predict AT from the prop-

erties of these eigenmodes.

### 3.3. Predicting asymmetric transmission from the quasinormal modes of a system

Here we follow a general approach and develop a theoretical formalism to predict AT from the quasinormal modes in any chiral resonator.

3

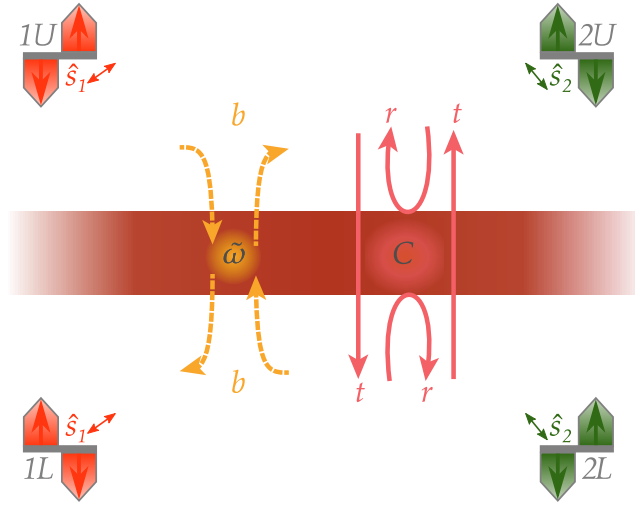


**Figure 3.3: Coupled-mode-theory-based concept of eigenmodes' interaction with incoming/outgoing waves:** Four ports  $1U, 2U, 1L$  and  $2L$  represent incoming and outgoing electromagnetic plane waves of the two polarizations  $\hat{s}_1$  and  $\hat{s}_2$ . The ports corresponding to orthogonal polarizations are separately shown for clarity. Scattering eigenvector  $b$  mediates the interaction of resonances ( $\tilde{\omega}$ ) with these ports. Waves can also couple directly ( $C$ ) through reflection and transmission coefficients  $r$  and  $t$ . See the text for detailed description.

Consider an open optical system having a set of quasinormal modes as shown in Fig. 3.3. The modes interact with incoming and outgoing plane waves above and below the system. The two orthogonal polarizations  $\hat{s}_1$  and  $\hat{s}_2$  characterize the electric fields of these waves. Four ports  $1U, 2U, 1L$  and  $2L$ , carrying incoming and outgoing electromagnetic waves, are used to represent these two polarizations above and below the system. The ports  $1U$  and  $2U$  respectively depict the polarizations  $\hat{s}_1$  and  $\hat{s}_2$  of the incoming or outgoing waves above the structure. The two polarization ports above the system are shown separately in the figure for clarity. Similarly, the ports  $1L$  and  $2L$  depict the polarizations  $\hat{s}_1$  and  $\hat{s}_2$  of the waves below the structure.

As seen in Ch. 2, the system's scattering matrix, which contains frequency-

dependent transmission and reflection coefficients, can be written as the sum of two scattering matrices featuring the two types of interaction between the incoming and outgoing waves: (i) the resonance-assisted interaction (denoted by the  $\tilde{\omega}$  channel in Fig. 3.3), where the waves couple through the resonant modes of the structure, and (ii) the non-resonant interaction (denoted by  $C$  in the figure), where the waves couple directly through a non-resonant background process.

The resonant interaction, as illustrated in the figure, is related to the mode's radiated electric field values at ports  $1U, 2U, 1L$  and  $2L$ , which can be described by a scattering eigenvector  $\mathbf{b} = [b_{1U} \ b_{2U} \ b_{1L} \ b_{2L}]^\top$  that contains the far-field components of quasinormal modes at each port. We characterize the non-resonant coupling by the frequency-dependent scattering matrix  $C$ . This direct-process scattering matrix has a non-chiral and polarization-independent response as:

$$C(\omega) = \begin{bmatrix} r(\omega) & 0 & it(\omega) & 0 \\ 0 & r(\omega) & 0 & it(\omega) \\ it(\omega) & 0 & r(\omega) & 0 \\ 0 & it(\omega) & 0 & r(\omega) \end{bmatrix}. \quad (3.6)$$

The direct scattering matrix  $C$  must be unitary and symmetric for reciprocal materials [55]. The frequency-dependent coefficients  $r$  and  $t$  are the direct reflection and transmission coefficients, respectively.<sup>1</sup>

For the structure under consideration, the non-resonant reflection and transmission coefficients in Eq. (3.6) are obtained by fitting [60] the background response of the numerical simulation data to the response of a slab-like structure with an effective homogeneous permittivity and thickness. The calculated slowly varying transmission and reflection intensities  $T = t^2$  and  $R = r^2$  are shown as yellow and gray solid lines, respectively, in Fig. 3.2. Using Eq. (2.25), we predict various transmittances  $T_{xx}, T_{yx}, T_{xy}$  and  $T_{yy}$  as well as the AT for the example structure. The predicted quantities, represented by solid lines in Fig. 3.2a and b, correspond very well with the simulation data.

In these predictions, we use only the complex frequencies and the far-field electric field amplitudes of the eigenmodes. Since we are able to predict the AT for the structure only from the far-field properties of the eigenmodes of the structure, it is now clear that AT is a resonant phenomenon that completely depends on the far-field characteristics. So, by tuning the mode properties, we can enhance the AT offered by the structure. At this juncture, it is instructive to study what the maximum AT is that can be achieved in any structure and how to design structures that can reach such a limit.

<sup>1</sup>The arbitrary phase factor of this matrix, which depends on the choice of the positions of our reference ports [61], can be omitted without any loss of generality and we can suppose  $r$  and  $t$  to be positive real amplitudes such that  $r^2 + t^2 = 1$ .

### 3.4. On the limit of asymmetric transmission

Dependence of the AT on the far-field properties of the eigenmodes stems from the interaction of the incoming and outgoing waves with the scattering eigenvector  $\mathbf{b}$  of the modes. The eigenvector  $\mathbf{b}$  can be normalized arbitrarily as the expression for the scattering matrix is independent of such normalization (see Sec. 2.B). Thus, for each mode,  $\mathbf{b}$  basically comprises a set of field values ( $b_{1U}, b_{2U}, b_{1L}$  and  $b_{2L}$ ). The field values  $b_{1U}$  and  $b_{2U}$  represent the two components of eigenmode polarization above the structure and  $b_{1L}$  and  $b_{2L}$  represent the two eigenmode polarization components below the structure in the far field. For the example structure, the eigenmode field polarizations above and below the structure are related to each other by certain symmetry properties. The symmetry in the chosen structure is such that it returns to the original configuration after a series of operations: (i) an inversion along  $z$ , (ii) an inversion along  $x$ , and (iii) a clockwise rotation of  $90^\circ$  about  $z$  (see Fig. 3.A.1 in appendix). This symmetry dictates that the eigenvectors of the system must satisfy the following relation among the polarization components of the eigenmode field below the structure and the polarization components above the structure:

$$b_{1L} = \pm b_{2U}, \quad b_{2L} = \pm b_{1U}. \quad (3.7)$$

Inspection of calculated eigenfields from the FEM simulation confirms these relationships. In the range of frequencies we plot in Fig. 3.2, it can be observed that the highest AT occurs around an isolated mode at  $\omega_0/2\pi = 364$  THz. The linewidth of the mode is  $\sim 0.6$  THz. We can represent the far-field polarization ( $b_{1U}, b_{2U}$ ) of the eigenmode in terms of a set of normalized Stokes parameters  $S_1, S_2$  and  $S_3$  [14].

Expressing  $\mathbf{b}$  in terms of the polarization parameters and applying Eqs. (3.5) and (2.25) we get an equation for the AT provided by a single mode in terms of its polarization parameters (as elaborated in appendix 3.A). We find that, at the eigenfrequency, the peak value of AT and the polarization parameters of the eigenmode have a direct relation:

$$\text{AT} = ||b_{1U}|^2 - |b_{2U}|^2| = |S_1|, \quad (3.8)$$

where  $S_1$  is the first normalized Stokes parameter. This very simple, yet powerful relation holds a huge potential for obtaining the maximum possible AT by parametric optimization of any structure. A chosen structural parameter can be swept while tracking the isolated modes and the calculated  $S_1$  can predict the AT for each case. To illustrate this, we vary a single parameter, the total thickness of the chiral photonic crystal, and depict the predicted AT for the considered isolated eigenmode as a function of the thickness. The blue solid line in Fig. 3.4a represents the theoretically predicted AT (the Stokes parameter  $S_1$ ) for different thicknesses. The transmission simulation results are shown alongside as dashed lines to verify the prediction. It can be seen



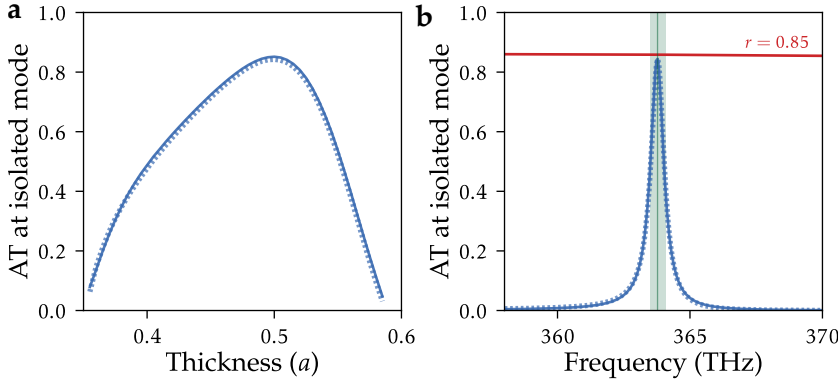


**Figure 3.4: Parameter optimization and the fundamental limit of AT for a single mode of the proposed structure:** **a.** Predicted AT for an isolated single mode for different thicknesses of the structure are shown as blue solid line. Corresponding simulation results are shown as blue dashed line. **b.** Calculated AT (blue solid line) and fundamental limit of maximum AT (red solid line) for a single mode (green vertical line) together with FEM simulation data (blue dashed lines). The green shaded region denotes the linewidth of the mode.

that the optimum thickness is  $0.5 \cdot a$ , where  $a$  is the periodicity of the structure. In fact, the structure we presented in Fig. 3.2 is the optimized case. It is to be noted that the maximum AT offered by the structure is  $\sim 85\%$ , which is less than unity.

According to Eq. (3.8), we would attain unity AT when  $|S_1| = 1$ , i.e., when the eigenmode of the structure is completely linearly polarized along one of the  $x$  and  $y$  Cartesian axes of the structure. However, we find that the polarization parameters of the mode are restricted such that it is not always possible to get a mode that is completely linearly polarized in the far field. This constraint arises from the principle of reciprocity, which relates the polarization parameters of the resonant mode to the non-resonant scattering properties of the structure. In the following, we show how the principle of reciprocity puts a fundamental limit to the possible polarization parameters for a mode, and hence the AT.

From Eq. 2.11, the principle of reciprocity in coupled-mode theory can be expressed for a single mode as:

$$C\mathbf{b}^* = -e^{i\xi}\mathbf{b}, \quad (3.9)$$

where the total phase factor  $\xi$  subsumes the arbitrary phase factors in the definition of  $C$  and in the normalization of  $\mathbf{b}$  (see Sec. 3.B). Expressing Eq. (3.9) in terms of the components  $r$  and  $t$  that make up  $C$  and the polarization parameters from the normalized  $\mathbf{b}$  (as detailed in Sec. 3.B), we obtain that Eq. (3.9) implies the relation:

$$\frac{t}{r} = \left| \frac{S_3}{S_1} \right|, \quad (3.10)$$

which indicates that the ratio between the Stokes parameters  $S_3$  and  $S_1$  of the eigenmode is related to the non-resonant background transmission of the structure at the mode frequency. This is extremely interesting, because it shows that a mode can be linearly polarized ( $|S_3| = 0, |S_1| = 1$ ) only if the corresponding non-resonant transmission coefficient  $t$  is zero. Realistically, the background transmission from a homogeneous effective dielectric slab can never go to zero. Consequently, the modes of the system are generally constrained to be elliptically polarized.

We use Eq. (3.10) to derive the fundamental constraint on the AT for the structure. The relation  $S_1^2 + S_3^2 \leq 1$ , which follows directly from the normalization of Stokes parameters, then implies  $S_1^2 (1 + \frac{t^2}{r^2}) \leq 1$ , and from Eq. (3.8) we obtain:

$$AT \leq r = \sqrt{R}, \quad (3.11)$$

where  $R = r^2$  is the non-resonant reflectivity of the structure. It is interesting to note that AT, which is the difference between two resonant transmission intensities, has a limit which is given by the non-resonant reflection amplitude. For practical applications that require maximum AT, it is thus important to engineer maximum non-resonant  $R$  at the operation wavelength.

We choose the mode ( $\omega_0/2\pi = 364$  THz) having the highest AT from the FEM simulation data and calculate the fundamental limit for the maximum AT around this mode. The dashed line in Fig. 3.4b shows the FEM simulation-based AT as a function of the frequency of the normally incident light. The calculated fundamental limit,  $r$ , is shown as the red solid line. It can be seen that the theoretically calculated AT (blue solid line) as well as the FEM simulation data are very close to the fundamental limit.

The discussion so far in this section has been limited to the particular structure we proposed as an example. The specific symmetry properties of the structure were used to derive the results stated above. It is therefore important to verify the universality of the results on the limit of AT. In the following, we seek a fundamental limit for the AT offered by any single-mode resonator regardless of its symmetry properties and find that the result stays the same for the general case as well.

For deriving the limits for a general structure, we are no longer allowed to use the relation given by Eq. (3.7), as it was derived from the specific symmetry properties of the example. Equation (3.9), which is based on the principle of reciprocity, is still valid and can be used to relate below-the-structure polarization parameters to the polarization parameters above the structure. Using this new relation (see appendix 3.C for a detailed derivation) in Eq. (2.25) leads to a general expression for AT in terms of the polarization parameters  $S_1$  and  $S_3$ , the phase factor  $\xi$ , and the coefficients  $r$  and  $t$ :

$$AT = \left| \frac{r t^2 (1 - S_1^2) \sin \phi \sin \xi}{(1 + r (\cos \phi \cos \xi + S_1 \sin \phi \sin \xi))^2} \right|, \quad (3.12)$$

where  $\phi = \arctan(\frac{S_3}{S_2})$  is the phase difference between the orthogonal polarization components of the eigenmode field above the structure. The local maximum of this equation can be found from an analysis of its first-order derivatives, and corresponds to the condition  $|S_1| = r$ ,  $|S_3| = t$  and  $\xi = \pm \frac{\pi}{2}$ . The corresponding value of AT at the maximum is  $AT_{max} = r = \sqrt{R}$ . As we will now show, this maximum is a global maximum, which means that the non-resonant reflectivity puts the same fundamental limit for the AT in any single mode resonator irrespective of its structural symmetry.

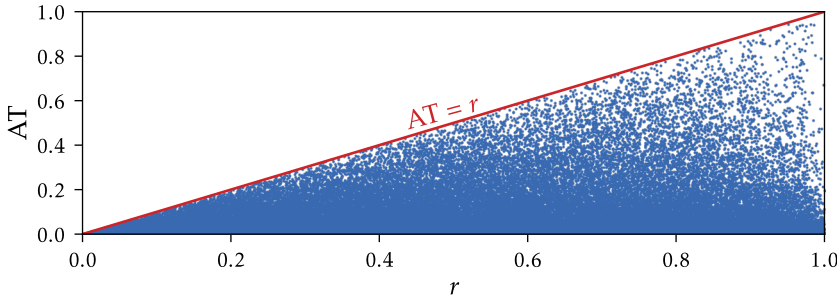


**Figure 3.5: Fundamental limit of AT:** Scatterplot of AT vs the non-resonant reflection coefficient  $r$  for 100,000 random eigenmode polarizations in a structure without any specific symmetry properties. Solid red line corresponds to  $AT = r$ .

Using Eq. (3.12), we calculate AT for an isolated mode for 100,000 randomly chosen points in the polarization space i.e., random values of  $S_1$ ,  $\phi$ , and  $\xi$ . The calculated AT is plotted in Fig. 3.5 as a function of reflection coefficient  $r$ . This effectively means that we have computed the responses of a large number of different hypothetical structures (in terms of the properties of their resonant states). It can be observed that all the values are below or at the predicted fundamental limit,  $r$ . It must also be noted that most of the random polarizations exhibit an AT significantly lower than the fundamental limit. Only very few combinations of polarization parameters can produce an AT close to the fundamental limit.

As we have shown using Eq. (3.10) and Fig. 3.4a earlier in this section, with an educated choice of structural symmetry and a proper optimization of structural parameters, we can now design structures that offer an AT near the fundamental limits. The system proposed as an example in Fig. 3.2b would be an excellent candidate for realizing high AT with a fully dielectric structure.

### 3.5. Discussion and Conclusions

The basis for the outlined theoretical results is coupled-mode theory, which allows to extend these results to any general resonator system. The discussed examples used for deriving the limits are dielectric 2-D periodic structures. For metallic or lossy systems including systems with more than two input/output channels, the expression for the scattering matrix and the subsequent equations for AT and its limits can be re-derived considering the non-radiative decay rates of the modes [47]. We remark that it is not yet clear if the effect of AT can be enhanced by stacking multiple structures. In all cases, one could in principle raise the limits through any approaches that raise the non-resonant reflectivity of the system. It must also be noted that it is possible to use the coupled-mode theory for describing the scattering properties of arbitrary-shaped particles [66]. This allows us to extend our formalism to such particles as well. We observe narrow band of operation for the highest AT structures. Further studies are required to find if a limit exists also for the bandwidth of operation for AT.

In conclusion, by developing a theoretical formalism that can predict AT offered by any system from the far-field properties of its complex eigenmodes, we showed that the AT in chiral resonators depends strongly on their eigenmodes. We investigated the theoretical maximization of AT in chiral resonators. A fundamental limit for AT provided by a single mode is presented. We also proposed the design for a chiral photonic crystal that can offer AT as high as the fundamental limit, which is the non-resonant reflection amplitude of the system. The theoretical formalism presented here opens ways for designing and optimizing new structures for light manipulation.

## APPENDICES

## 3.A. Derivation of asymmetric transmission from quasinormal modes

Here, based on symmetry properties, we derive an expression for AT from a single mode. We have seen in Ch. 2 that building upon Ref. [55], the scattering matrix for a system with a set of complex eigenfrequencies  $\tilde{\omega}_j (j = 1, \dots, m)$  can be written as

$$S(\omega) = C + i \sum_{j=1}^m \frac{1}{\lambda_j} \frac{\mathbf{b}_j \mathbf{b}_j^\top}{\omega - \tilde{\omega}_j}, \quad (3.A.1)$$

where  $C$  is the direct-transport matrix (assumed to be a scattering matrix itself, thus unitary and symmetric) and  $\tilde{\omega}_j$  are the complex eigenfrequencies of the quasinormal modes of the system (we assume the convention  $\text{Im}(\tilde{\omega}_j) > 0$ ). The general expression for the coefficients  $\lambda_j$  is already discussed in Ch. 2. For a single isolated mode (with eigenfrequency  $\tilde{\omega}_0$ ), this expression reduces to  $\lambda_0 = \mathbf{b}^\top C^\dagger \mathbf{b} / (2\text{Im}(\tilde{\omega}_0))$ . Then, at the resonance frequency ( $\omega = \text{Re}(\tilde{\omega}_0)$ ), Eq. (3.A.1) becomes:

$$S = C - 2 \frac{\mathbf{b} \mathbf{b}^\top}{\mathbf{b}^\top C^\dagger \mathbf{b}}. \quad (3.A.2)$$

Both the direct-coupling matrix  $C$  and the resulting scattering matrix  $S$  are unitary. From the relation  $\mathbf{b}^\top S^\dagger S \mathbf{b}^* = \mathbf{b}^\top \mathbf{b}^*$ , by replacing Eq. (3.A.2), we obtain

$$|\mathbf{b}^\top C^\dagger \mathbf{b}|^2 = |\mathbf{b}^\top \mathbf{b}|^2. \quad (3.A.3)$$

The scattering eigenvector  $\mathbf{b}$  consists of a set of electric field components along  $\hat{\mathbf{s}}_1$  and  $\hat{\mathbf{s}}_2$  ( $b_{1U}$  and  $b_{2U}$ , respectively) which represents the eigenmode polarization above the structure and a set of field components ( $b_{1L}$  and  $b_{2L}$ ) which represents the eigenmode polarization below the structure, in the far-field. Thus,  $\mathbf{b}$  can be written as:  $\mathbf{b} = [b_{1U} \ b_{2U} \ b_{1L} \ b_{2L}]^\top$ . As it can be seen by direct inspection, Eq. (3.A.2) is independent of the choice of the normalization of  $\mathbf{b}$ .

As mentioned in the main text, for reciprocal materials the asymmetric transmission (AT) can be defined as the difference in orthogonal transmittances for two mutually perpendicular polarized incidences in a given direction. For generality, let us define the two orthogonal linearly polarized input vectors as

$$\hat{\mathbf{s}}_{1\text{in}} = \begin{bmatrix} \cos \psi \\ \sin \psi \\ 0 \\ 0 \end{bmatrix}, \quad \hat{\mathbf{s}}_{2\text{in}} = \begin{bmatrix} -\sin \psi \\ \cos \psi \\ 0 \\ 0 \end{bmatrix}, \quad (3.A.4)$$

where the angle  $\psi$  gives the polarization angle of input light with respect to the geometrical reference  $x$  axis of the structure.

Let  $t_{21}$  be the transmission component along  $\hat{s}_2$  when the input is  $\hat{s}_{1\text{in}}$  and  $t_{12}$  be the transmission component along  $\hat{s}_1$  when the input is  $\hat{s}_{2\text{in}}$ . The cross-polarized transmission coefficients,  $t_{21}$  and  $t_{12}$ , can then be calculated as:

$$\begin{aligned} t_{21} &= \begin{bmatrix} 0 & 0 & -\sin \psi & \cos \psi \end{bmatrix} S \hat{s}_{1\text{in}}, \\ t_{12} &= \begin{bmatrix} 0 & 0 & \cos \psi & \sin \psi \end{bmatrix} S \hat{s}_{2\text{in}}. \end{aligned} \quad (3.A.5)$$

The expression for AT can thus be written as:

$$AT = |T_{21} - T_{12}| = ||t_{12}|^2 - |t_{21}|^2|. \quad (3.A.6)$$

The symmetry properties of the example structure can be used to derive a relation between the polarizations of the eigenmode above and below the structure.

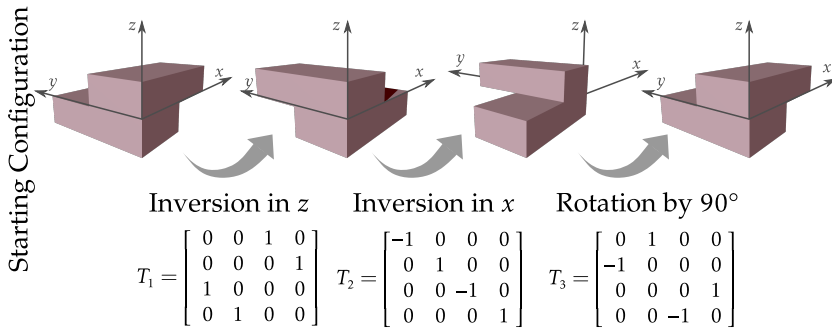


**Figure 3.A.1: Series of symmetry operations for the proposed structure:** A cartoon illustrating one possible series of symmetry operations that would return the proposed structure to its original configuration. For simplicity, the cartoon shows the arrangement of holes inside the unit cell. Corresponding transformation matrices are shown alongside.

The structure possesses certain symmetry properties such that it returns to the original configuration after a possible series of operations as illustrated in Fig. 3.A.1. For simplicity, in the figure we show only the configuration of holes inside a unit cell. Shown alongside the operations in the figure are the corresponding transformation matrices:  $T_1$  (an inversion along  $z$ ),  $T_2$  (an inversion along  $x$ ), and  $T_3$  (a clockwise rotation of  $90^\circ$  about  $z$ ).

The total transformation matrix for such a series of operations can be written as:

$$T = T_3 T_2 T_1 = \begin{bmatrix} 0 & 0 & 0 & 1 \\ 0 & 0 & 1 & 0 \\ 0 & 1 & 0 & 0 \\ 1 & 0 & 0 & 0 \end{bmatrix}. \quad (3.A.7)$$

From this symmetry it follows that the eigenvectors of the system must satisfy the relation  $T\mathbf{b} = \pm\mathbf{b}$  [119]. For this relation to hold, the eigenmode electric field values above and below the structure must be related according to Eq.(3.7), which is repeated here for convenience:

$$b_{1L} = \pm b_{2U}, \quad b_{2L} = \pm b_{1U}. \quad (3.A.8)$$

As a consequence of this symmetry relations, we can represent the scattering eigenvector  $\mathbf{b}$  only in terms of the polarization parameters above the structure:

$$\mathbf{b} = \begin{bmatrix} \cos\theta e^{-i\frac{\phi}{2}} \\ \sin\theta e^{i\frac{\phi}{2}} \\ \pm \sin\theta e^{i\frac{\phi}{2}} \\ \pm \cos\theta e^{-i\frac{\phi}{2}} \end{bmatrix}, \quad (3.A.9)$$

where  $\tan(\theta)$  is the ratio of amplitudes of the field components  $b_{1U}$  and  $b_{2U}$  and  $\phi$  is the relative phase between them.

In order to compute the AT, the cross-polarized transmittances  $T_{21}$  and  $T_{12}$  can be obtained from Eq. (3.A.2), (3.A.3), (3.A.5), and (3.A.9):

$$\begin{aligned} T_{21} &= |t_{21}|^2 = |(\pm \cos^2\theta \cos^2\psi e^{-i\phi} \mp \sin^2\theta \sin^2\psi e^{i\phi})|^2, \\ T_{12} &= |t_{12}|^2 = |(\pm \sin^2\theta \cos^2\psi e^{i\phi} \mp \cos^2\theta \sin^2\psi e^{-i\phi})|^2. \end{aligned} \quad (3.A.10)$$

AT can then be calculated from Eq. (3.A.6):

$$AT = |T_{12} - T_{21}| = |\cos(2\theta) \cos(2\psi)|. \quad (3.A.11)$$

This equation gives us an insight into the choice of input polarization direction for maximizing the AT. The maximum AT corresponds to the choice of the input polarization along the geometrical reference  $x$  axis of the structure ( $\psi = 0$ ). In this case, we have a final expression for AT as:

$$AT = |\cos(2\theta)|. \quad (3.A.12)$$

The polarization of the far-field of eigenmodes can also be expressed in terms of normalized Stokes parameters, which, using the notation of Eq. (3.A.9), are defined as

$$\begin{aligned} S_0 &= \cos^2\theta + \sin^2\theta = 1, \\ S_1 &= \cos^2\theta - \sin^2\theta = \cos(2\theta), \\ S_2 &= 2\cos\theta \sin\theta \cos\phi = \sin(2\theta) \cos\phi, \\ S_3 &= 2\cos\theta \sin\theta \sin\phi = \sin(2\theta) \sin\phi. \end{aligned} \quad (3.A.13)$$

Using the definition of the Stokes parameters, Eq. (3.A.12) can be recast in the form reported in Eq.(3.8):

$$AT = |S_1|. \quad (3.A.14)$$

### 3.B. Principle of Reciprocity and the limit of AT

From Eq. (2.11), the principle of reciprocity in coupled-mode theory states that the direct-process matrix and the resonant process are related by the expression

$$\bar{C} \mathbf{d}^* = -\mathbf{d}, \quad (3.B.1)$$

where  $\mathbf{d}$  is the vector containing coupling coefficients that relate the resonance to the input and output waves and  $\bar{C}$  is the direct coupling matrix of the system [55]. For a single mode, the coupling vector is proportional to the far-field amplitudes of the eigenmode with a complex proportionality coefficient having unit magnitude, i.e.,  $\mathbf{d} = e^{i\zeta} \mathbf{b}$ . By expressing the direct matrix as  $\bar{C} = e^{i\chi} C$ , where  $C$  is the direct matrix defined in Eq. (3.6) of the main text, we can write the principle of reciprocity as:

$$e^{i\chi} C \mathbf{b}^* = -e^{2i\zeta} \mathbf{b}. \quad (3.B.2)$$

The  $C$ -matrix phase factor can be incorporated without loss of generality in a total phase factor  $\xi = 2\zeta - \chi$ . In this way, we arrive at Eq.(3.9) of the main text:

$$C \mathbf{b}^* = -e^{i\xi} \mathbf{b}. \quad (3.B.3)$$

Using Eq. (3.A.9) and the definition of  $C$  from Eq. (3.6) in Eq. (3.B.3), we can write:

$$r \cos \theta e^{i\frac{\phi}{2}} \pm it \sin \theta e^{-i\frac{\phi}{2}} = -e^{i\xi} \cos \theta e^{-i\frac{\phi}{2}}, \quad (3.B.4)$$

$$r \sin \theta e^{-i\frac{\phi}{2}} \pm it \cos \theta e^{i\frac{\phi}{2}} = -e^{i\xi} \sin \theta e^{i\frac{\phi}{2}}. \quad (3.B.5)$$

The ratio of Eq. (3.B.4) and Eq. (3.B.5), after some algebraic manipulations, gives Eq. (3.10) in the main text:

$$\frac{t}{r} = \left| \frac{2 \cos \theta \sin \theta \sin \phi}{\cos^2 \theta - \sin^2 \theta} \right| = \left| \frac{S_3}{S_1} \right|. \quad (3.B.6)$$

From this equation and the normalization of the Stokes parameters ( $S_1^2 + S_2^2 + S_3^2 = 1$ ), the intrinsic limit on AT discussed in the main text,  $AT \leq r$ , is derived.

### 3.C. AT and its limit for general structures

For general structures without any symmetry properties, we are no longer allowed to use the symmetry condition given by Eq. (3.A.8). However, we can express the polarization components of the eigenmode field below the structure in terms of the components above the structure using the principle



of reciprocity in Eq. (3.B.3). From Eq. (3.B.3), it can be shown that:

$$\begin{aligned} b_{1L} &= \frac{b_{1U} r + b_{1U}^* e^{-i\xi}}{i t}, \\ b_{2L} &= \frac{b_{2U} r + b_{2U}^* e^{-i\xi}}{i t}. \end{aligned} \quad (3.C.1)$$

Using the same notation as in Eq. (3.A.9) for the polarization of the field above the structure, we can write  $\mathbf{b}$  as:

$$\mathbf{b} = \begin{bmatrix} \cos \theta e^{-i\frac{\phi}{2}} \\ \sin \theta e^{i\frac{\phi}{2}} \\ \frac{1}{i t} (r + e^{i(\phi-\xi)}) \cos \theta e^{-i\frac{\phi}{2}} \\ \frac{1}{i t} (r + e^{-i(\phi+\xi)}) \sin \theta e^{i\frac{\phi}{2}} \end{bmatrix}. \quad (3.C.2)$$

AT can be obtained from Eq. (3.A.6), together with Eqs. (3.A.2) and (3.A.5), as

$$AT = \left| \frac{4 r t^2 \cos^2 \theta \sin^2 \theta \sin \phi \sin \xi}{(1 + r (\cos^2 \theta \cos(\phi - \xi) + \sin^2 \theta \cos(\phi + \xi)))^2} \right|. \quad (3.C.3)$$

In deriving this equation we have assumed  $\psi = 0$  without loss of generality in the definition of the input vectors in Eq. (3.A.4).

We can write Eq. (3.C.3) in terms of the Stokes parameters for the polarization above the structure, obtaining Eq. (3.12) in the main text, which is repeated here:

$$AT = \left| \frac{r t^2 (1 - S_1^2) \sin \phi \sin \xi}{(1 + r (\cos \phi \cos \xi + S_1 \sin \phi \sin \xi))^2} \right|. \quad (3.C.4)$$

As stated in the text, the maxima of AT correspond to the points  $|S_1| = r$ ,  $|S_3| = t$ ,  $\xi = \pm\pi/2$ , as can be verified by computing the first derivatives of Eq. (3.C.4). In a similar fashion, it can be verified that all these points are equivalent global maxima.

As an example, in Fig. 3.C.1, we plot the maximum AT (maximized over  $\xi$ ) given by Eq. (3.C.4) as a function of  $S_1$  and  $\phi$ , for a direct reflection coefficient  $r = 0.85$ . The global maximum of AT is marked by the green circle and corresponds to the value  $AT = r = 0.85$ , as expected. The dashed green line indicates the curve in polarization space where the ratio between the Stokes parameters is equal to the ratio of the direct-process reflection and transmission coefficients, i.e., it corresponds to Eq. (3.B.6). It can be seen that most of this line is along near-the-limit regions of the maximum AT. As discussed beforehand, all the structures with the same symmetry as the one proposed in this chapter follow the same relation. As a consequence, structures having symmetries of this kind have significant prospects for offering AT near the fundamental limit.

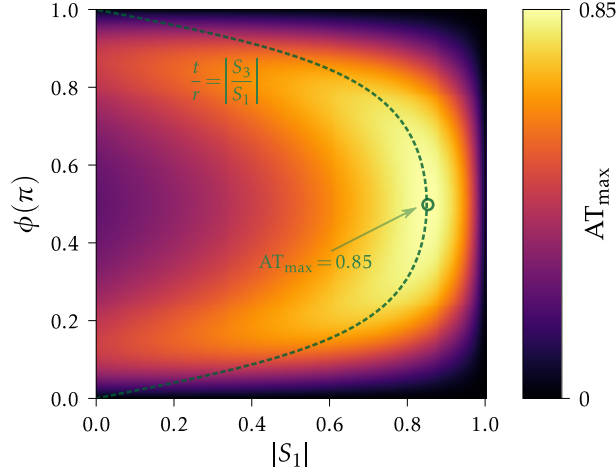


**Figure 3.C.1: Numerical maximization of AT:** The 2-D plot shows numerically calculated values of AT, maximized over the total phase factor  $\xi \in (0, 2\pi)$  and given by Eq. (3.C.4) as a function of eigenmode polarization parameters  $S_1$  and  $\phi$ . The green circle marks the maximum value of  $AT_{max}$  in the 2-D space. The green dashed line corresponds to the points in the polarization space that follow the relation  $\frac{t}{r} = \left| \frac{S_3}{S_1} \right|$ .

### 3.D. Implications of angular dependence

In all the simulations and calculations presented in the main text, we consider light that is incident normally onto the sample. However, a real experimental setup involves the use of finite-size incident beams with a finite angular spread. It is thus important to calculate the variation of AT as a function of angle of incidence. This is particularly relevant to the example of a planar periodic sample that we used in our example, as its modal bandstructure will depend on angle.

We consider a beam of light that is polarized perpendicularly to the in-plane axis  $y$  and propagates along either the  $z$  or  $-z$  directions. As a consequence of the finite size of the beam, the incident electric field can be described as the superposition of plane waves with different in-plane wavevectors  $\mathbf{k}_{\parallel} = (k_x, k_y)$ :

$$\mathbf{E}(\mathbf{r}) = \int dk_x dk_y \frac{\mathcal{E}(k_x, k_y)}{\sqrt{k_x^2 + k_z^2}} \begin{bmatrix} -k_z \\ 0 \\ k_x \end{bmatrix} e^{i(k_x x + k_y y + k_z z)}, \quad (3.D.1)$$

where  $\mathcal{E}(k_x, k_y)$  corresponds to the amplitudes of the in-plane Fourier components and  $k_z = \pm(k_0^2 - k_x^2 - k_y^2)^{1/2}$ .

In Fig. 3.D.1, for a given frequency ( $\omega_0/2\pi = 363.78$  THz), we calculate the AT of the system introduced in Fig. 3.2 as a function of the in-plane wavevec-

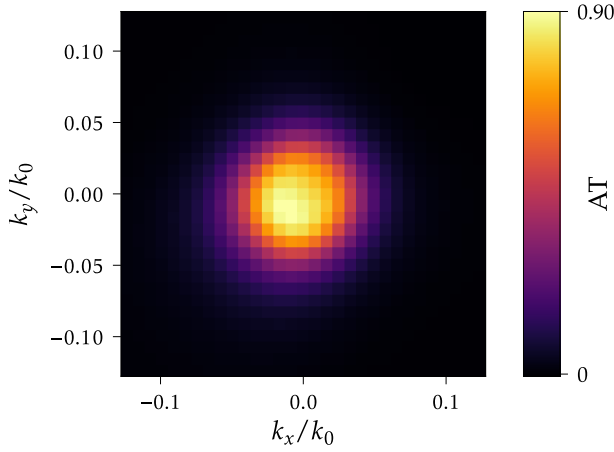


**Figure 3.D.1: AT at oblique incidence:** Variation of AT as a function of in-plane wave-vector at a frequency of  $\omega_0/2\pi = 363.78$  THz from FEM simulations. In-plane wave vector is shown in units of  $k_0 = \omega_0/c$ .

tor  $\mathbf{k}_{\parallel} = (k_x, k_y)$ . The calculations have been performed with the finite element method. As evident from the figure, AT varies with the variation of the incident angle with respect to normal incidence ( $k_x = k_y = 0$ ). This is likely a result of the fact that for finite angles the mode frequency is expected to shift away from the resonance frequency  $\omega_0$  at normal incidence, as well as a potential evolution of the mode's polarization along the photonic crystal band. From the data in the figure, we can estimate a maximal half opening angle for the incident field of the order of  $\text{NA} \simeq 0.05$ , that corresponds, assuming a Gaussian envelope for the field, to a minimal beam waist of the order of  $w \simeq 6\lambda_0$ . This value also constrains the minimal size of the sample, and it seems fully compatible with realistic experimental and fabrication conditions.



# II

## TOPOLOGICAL PHOTONIC CRYSTALS FOR LIGHT MANIPULATION



# 4

## DIRECT OBSERVATION OF TOPOLOGICAL EDGE STATES IN SILICON PHOTONIC CRYSTALS

*“Only the number theory and topology (analysis situs) still remain purely mathematical disciplines without any application to physics. Could it be that they will be called to help in our further understanding of the riddles of nature?”*

— George Gamow, *Biography of Physics*, 1961

*Introducing topological protection in photonic materials offers new prospects for guiding and manipulating classical and quantum light. The mechanism of spin-orbit coupling promises the emergence of edge states that are helical; exhibiting unidirectional propagation that is topologically protected against back-scattering. We directly observe the topological states of a photonic analogue of electronic materials exhibiting the quantum Spin Hall effect, living at the interface between two silicon photonic crystals with different topological order. Through the far-field radiation that is inherent to the states' existence we characterize their properties, including linear dispersion and low loss. Importantly, we find that the edge state pseudospin is encoded in unique circular far-field polarization and linked to unidirectional propagation, thus revealing a signature of the underlying photonic spin-orbit coupling.*

---

Parts of this chapter are contained in the preprint arXiv:1811.10739 (2018) [120].

## 4.1. Introduction

The concept of topology has proven immensely powerful in physics, describing new phases of matter with unique properties. The connection of the quantum Hall effect [121] to band structure topology explained the emergence of topologically protected unidirectional transport of electrons. These states exist at the edge of two-dimensional systems subject to an external magnetic field that breaks time-reversal (TR) symmetry. The prediction [33] and observation [34, 35] of the quantum spin-Hall effect (QSHE) unlocked a new door in the field of topological physics. This effect relies on spin-orbit coupling instead of an external magnetic field, causing spin-up and -down electrons to propagate in opposite directions in states that are protected by TR symmetry.

4

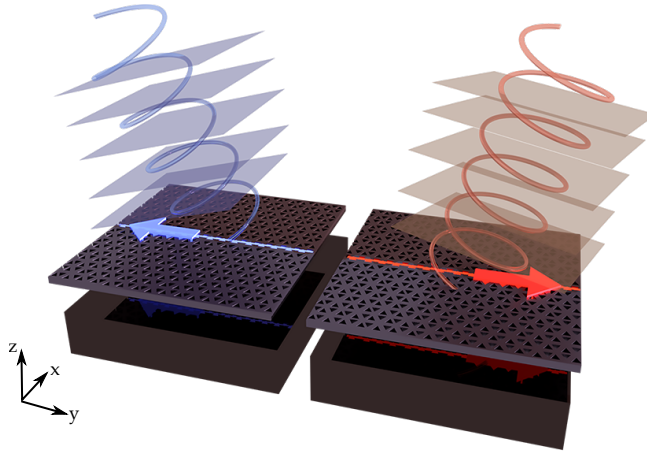


**Figure 4.1: Schematic representation of spin-orbit coupling in topological photonic crystals:** Chirality of the radiation field is connected to propagation direction of states at edges between photonic crystals with different topological bandstructure.

There has been a recent surge in attempts to implement topological protection in the acoustic, mechanical, microwave and optical domains [30, 122–135], owing to the application potential of robust transport. A particular opportunity is provided by photonic spin-orbit coupling [40, 136]. Photonic analogues of the QSHE were realized using arrayed ring resonators, where the helicity of propagation in the ring takes the role of (pseudo)spin [39, 137–140]. Recently, the QSHE was also predicted to occur in photonic crystals with special symmetries, with edge state propagation direction linked to local circular Poynting vector flows [141–143]. Such states were observed in the microwave domain [144, 145], and coupled to spin-polarized quantum dots [146]. Realizing topological photonic states in the telecom domain is especially promising in view of exciting possibilities like nanoscale routing, resilience to disorder,



one-way transport and robust light emission in integrated photonic chips. In contrast to valley-Hall topological photonic crystals [147–149] that operate below the light line, we can learn about the properties of topological photonic crystals employing QSHE even in far-field experiments [150].

In this chapter, we directly observe topological photonic states at telecom wavelengths in photonic crystals in silicon-on-insulator technology. Through angular spectroscopy and polarimetry, we retrieve the intriguing properties of not only the bulk states of crystals with different topological order, but also of the edge states that appear at their interfaces. We determine their dispersion, and reveal that the radiation of the topological states carries their unique nature: The states' pseudospin is encoded in the circular polarization of their far field, and one-to-one related to the unidirectional propagation. We show that the measured quality factors of  $\sim 450$  are intrinsically limited by the very radiation we observe, and experimentally observe an anti-crossing between unidirectional modes due to symmetry breaking at the crystal edge. A tight-binding model fitted to the measured bulk state dispersion correctly predicts the magnitude of this spin-spin scattering.

## 4.2. The origin of topological states for light

The topological states we study appear in two-dimensional photonic crystal slabs with engineered bandstructures. We fabricate photonic crystals with hexagonal unit cells containing equilateral triangular holes in a silicon membrane through electron beam lithography and reactive ion and wet etching of a silicon-on-insulator substrate (see appendix 4.A.2 for the detailed step-by-step procedure). Figure 4.2a shows a pseudo-coloured scanning electron micrograph of a fabricated sample in top view.

As bosonic systems do not feature the Kramers doubling that guarantees the existence of electronic states of opposite spin in crystals, we follow a symmetry-based approach to topological photonics outlined by Wu and Hu [141] and Barik et al. [142]. The scheme starts from a photonic crystal with scattering sites (in our case the triangular holes) arranged in a honeycomb lattice. We call such a lattice an 'ordinary lattice'. Viewing these crystals as a triangular lattice of hexagonal unit cells with six sites each, they exhibit a doubly degenerate Dirac cone at the  $\Gamma$  point (see Fig. 4.3b for the dispersion of such a system, calculated by finite-element method with COMSOL Multiphysics 5.2). We note that this choice of (six-site) unit cell is for now somewhat artificial: It is not the smallest possible unit cell of the honeycomb lattice. Choosing a smaller (two-site) unit cell would have led to a bandstructure with Dirac points at the edge of the Brillouin zone. Our choice leads to a 'folding' of those bands, such that the Dirac cones are 'copied' to the  $\Gamma$  point and become doubly degenerate [141, 142] — even though these particular Bloch components do not carry weight in the expansion of the eigenstates' fields. In that sense, identifying the six-fold unit cell here is

similar to choosing the two-site unit cell in the SSH model in Sec. 1.5.3, for the case  $v = w$ .

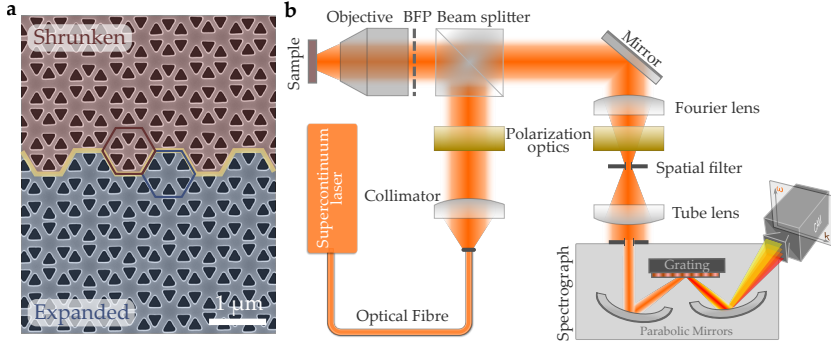


**Figure 4.2: Fabricated sample and experimental setup:** **a.** A scanning electron micrograph of the fabricated sample. The yellow line represents the arm-chair like edge between two pseudo-coloured regions of differing topology. Unit cells on either side are highlighted by red and blue hexagons. **b.** Experimental setup for Fourier spectroscopy. A Fourier lens images the objective back-focal plane (BFP) onto the spectrometer slit using a tube lens. A spatial filter chooses the area from which light is collected. Quarter wave plates together with linear polarizers (polarization optics) are used to define polarization of input light and for polarimetry measurements.

Preserving the  $C_6$  crystal symmetry, each hexagonal cluster is then deformed either by concentrically shifting the holes inwards (‘shrunk lattice’, top of Fig. 4.2a) or outwards (‘expanded lattice’, bottom of Fig. 4.2a), without altering unit cell size. Such deformations open a gap at the Dirac point, but qualitatively in different ways (see Fig. 4.3a and c for the calculated dispersion diagrams of the shrunk and expanded lattices, respectively). Note that, as the six-site unit cell became the smallest that describes the structure due to the deformation, the Bloch components close to the  $\Gamma$  point are now expected to acquire finite weight in the field expansion, in contrast to the ordinary lattice. A continuous deformation of the lattice from shrunk to expanded is necessarily accompanied by a closing of the bandgap, akin to the behaviour in the one-dimensional Su–Schrieffer–Heeger model [41, 44, 127, 151] described in Sec. 1.5.3. The shrunk and expanded lattices are then associated with two different band structure topologies analogous to a  $\mathbb{Z}_2$  topological insulator. A band inversion takes place across the closing of the gap, meaning that the nature of the states at the top and bottom band edges is opposite for shrunk and expanded crystals. The states of the bottom (top) bands in the shrunk (expanded) lattice, characterized by the out-of-plane magnetic field  $H_z$ , resemble  $p$ -orbitals, whereas the top (bottom) bands are  $d$ -like [141, 142]. Bulk-edge correspondence guarantees the existence of topologically protected states at the edge of two domains of different topology, such as the armchair interface in Fig. 4.2a. These states are expected to propagate along the edge

with a finite extent into either domain.

The unit cell deformation that opens the bandgap also couples the TE-like states in the silicon slab to far-field radiation. As both the band edges and edge states appear close to the  $\Gamma$  point, they are naturally phase-matched to free-space radiation [150]. As observed before, in either expanded or shrunk lattices the fundamental Bloch harmonic of the photonic crystal eigenmodes can carry finite weight. We can thus use this radiation field to characterize the energy, momentum, localization, and polarization of the states of the crystals and their edges.

### 4.3. Mapping dispersion of topological states

We use the reflectometry setup outlined in Fig. 4.2b to directly measure the photonic crystal band dispersion in reciprocal space. Focused infrared light from a supercontinuum laser source excites the crystal modes. Directly reflected and re-radiated light is collected from an area of  $\sim 30 \times 102 \mu\text{m}$ , restricted by a spatial filter (see appendix 4.A.3 for more details and a list of components). The numerical aperture of the objective was chosen to be of the order of 0.5, so as to match with the calculated angular distributions in Fig. 4.3a-c. By imaging the objective back focal plane onto the entrance slit of a spectrograph [152], we record two-dimensional images of frequency versus  $k_y$  wavevector of reflected light with  $k_x = 0$  on an infrared camera at the spectrograph output.

Figure 4.3d and f show the measured reflection as a function of frequency and  $k_y$  from shrunk and expanded lattice crystals for diagonally polarized input. The spectrally broad fringes are due to Fabry-Pérot-like reflections between the suspended membrane and the substrate (see appendix Fig. 4.B.1). We observe sharper resonant features interfering with this direct reflection background to produce bands with Fano lineshapes. The dispersion of these states corresponds well to the calculated photonic crystal band diagrams in Fig. 4.3a and c for both lattices, apart from an overall  $\sim 10\text{THz}$  frequency offset that is likely related to deviations of fabricated hole size and shape from designed geometry. Band gaps are visible around optical frequencies of  $\sim 200\text{THz}$ , with widths of  $9\text{THz}$  ( $\Delta\omega/\omega_0 \approx 4.4\%$ ) for the shrunk lattice and  $18\text{THz}$  ( $\Delta\omega/\omega_0 \approx 8.9\%$ ) for the expanded lattice. These measured bandgaps are in good agreement with the calculated relative gaps of  $4.7\%$  and  $7.8\%$ , respectively.

In addition to the expanded and shrunk lattices, we also fabricate an *ordinary* photonic crystal without the symmetry breaking, i.e., triangular holes arranged in a perfect honeycomb lattice. In such a system, there are no photonic crystal modes that can couple to the far-field, as the fundamental Bloch harmonic carries no weight due to the lattice symmetry. In Fig. 4.3e we show the measured reflected intensity for a honeycomb lattice of triangular holes. As expected, we don't see any sharp resonances in the spectra except for the

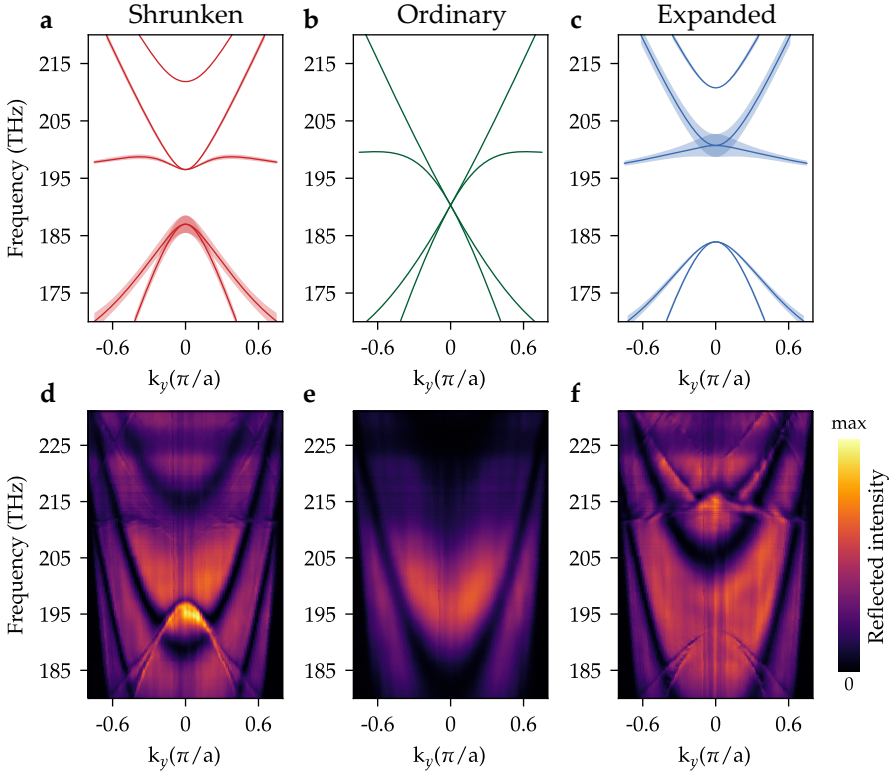


**Figure 4.3: Dispersion maps of the bulk lattices:** a-c. Calculated dispersion of the shrunk, ordinary and expanded lattices, respectively. Linewidths of the calculated modes for the corresponding lattices, scaled by a factor of 5, are shown as shaded regions. d-e. Measured dispersion of the shrunk, ordinary and expanded lattices, respectively, for diagonally polarized incidence.

background fringes from the Fabry-Pérot-like air cavity.

Figure 4.3 also shows the band inversion when comparing the reflection of shrunk and expanded lattices, manifested in the leakiness of their upper and lower bands [150]. The  $p$ -orbitals of  $H_z$  associated with the bottom (top) band edge of the shrunk (expanded) lattice mean that their in-plane electric field distributions are even with respect to the center of the unit cell. As such, these states can couple to radiation normal to the slab, whereas the  $d$ -orbital states are quadrupolar and dark. We observe the bright spectral features of the  $p$ -orbital states at opposite sides of the gap for the two lattices, accompanied with linewidth reduction of the other edge. The latter is confirmed by the mode calculations in Fig. 4.3a and c, where the shading widths are proportional to the imaginary part of the eigenmode frequency. These radiation properties thus confirm that the two lattices feature band gaps of different

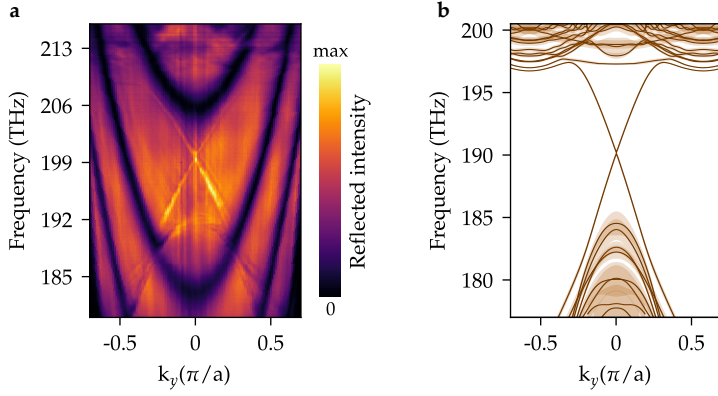


**Figure 4.4: Dispersion maps of the edge states:** **a.** Measured dispersion at an armchair edge, for diagonally polarized incidence, normalized to the maximum pixel value. **b.** Dispersion calculated by finite element method simulations. Calculated linewidths are shown as shaded region in **b**.

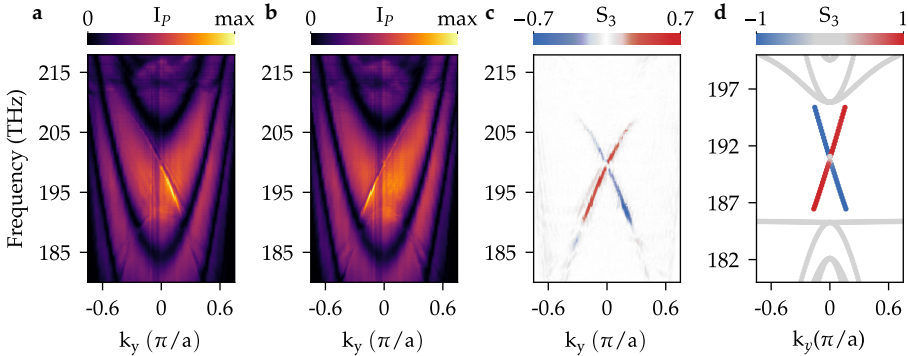
topological character.

Figure 4.4a shows the band diagram measured in reflection when exciting the armchair-like edge between regions of expanded and shrunk lattices with a diagonally polarized focused beam. We observe two states that close the bandgap with opposite group velocities, crossing at the  $\Gamma$  point. They exhibit the characteristic linear dispersion of edge states in QSHE topological insulators, with a measured group velocity that does not vary much ( $\sim c/6.3$  to  $\sim c/5.3$ ) over the effective band gap. The measured band diagram correspond well to the calculated modes shown in Fig. 4.4b.

#### 4.4. Detection of edge-state pseudospin

We then turn to study the polarization properties of these edge states, modifying the setup to add the functionality of polarimetry. This allows quantifying the polarization of the reflected field in terms of its Stokes parameters [14, 153]. We first excite the edge with circularly polarized (CP) light of different handedness and plot the intensity of the polarized component of the reflected field,  $I_p = \sqrt{S_1'^2 + S_2'^2 + S_3'^2}$ , where  $S_i$  are unnormalized Stokes parameters, in Figs. 4.5a and b. One recognizes that the two edge states of positive or negative group velocity are excited selectively with near-perfect contrast using either left or right CP inputs, respectively.

This observed helical nature of the edge states' far field can be understood by considering how these states originate from the  $p$ - and  $d$ -like orbitals in the infinite lattice unit cells. At the  $\Gamma$  point, the bands are degenerate. In the  $H_z$  field basis of  $|p_{\pm}\rangle = (|p_x\rangle \pm i|p_y\rangle)/\sqrt{2}$  and  $|d_{\pm}\rangle = (|d_{(x^2-y^2)}\rangle \pm i|d_{(xy)}\rangle)/\sqrt{2}$ , a tight-binding model that describes coupling between the sites results in



**Figure 4.5: Polarimetry results:** **a, b.** Total reflected intensity of the polarized field ( $I_p$ ) as a function of frequency and wavevector  $k_y$ , when the armchair edge is excited with right- (a) and left- (b) circularly polarized light. Images are normalized with respect to corresponding maximum pixel values. **c.** Measured circular polarization intensity (normalized Stokes parameter  $S_3$ ) when the edge is excited with light that is linearly polarized along  $y$ . A center block is placed at the real space plane to spatially filter background reflections (see appendix Fig. 4.A.2). **d.** Normalized  $S_3$  for the edge states as predicted by the tight-binding model.

a  $4 \times 4$  Hamiltonian in the approximation of nearest-neighbor coupling and linear expansion in  $k_x$  and  $k_y$  that is block-diagonal, meaning that only states of the same pseudospin  $\pm$  are coupled [141]. As a result, the edge states that connect the top and bottom bands must be associated with a single pseudospin, admixing either  $|p_+\rangle$  and  $|d_+\rangle$  or  $|p_-\rangle$  and  $|d_-\rangle$ . Since the  $p$ -like component is predominantly responsible for the plane wave emitted to the far-field, one can see that the fundamental harmonic of the Bloch mode must be circularly polarized, with handedness equal to the pseudospin.

This radiation and its polarization can be quantified in the tight-binding model by calculating the total in-plane dipole moment inside the unit cell  $\mathbf{p} \propto \sum_{i=1}^6 \hat{\theta}_i \psi_i$ , where  $\hat{\theta}_i$  is the azimuthal unit vector of the  $i^{\text{th}}$  site and  $|\psi\rangle$  is a six-dimensional scalar “wave function” with components  $\psi_i$  corresponding to  $H_z$  at site  $i$ . A tight-binding model with nearest-neighbour approximation such as the one in Ref. [142] predicts degenerate bulk bands over the entire reciprocal space. In contrast, we observe splitting of both upper and lower bands away from the  $\Gamma$  point in experiment and finite element simulation, with linear polarization (see appendix Fig. 4.C.1). In order to also correctly predict the polarization of the bulk bands, we need to extend the tight-binding model beyond the nearest-neighbour approximation. By introducing additional coupling terms up to third order in the tight-binding model (see appendix Fig. 4.D.1), we retrieve the observed lifting of degeneracy, allowing the prediction of the polarization of each observed state.

To assess the polarization of the edge and bulk states experimentally, we excite the edge with light that is horizontally polarized, and perform full



polarization tomography of the emitted radiation as a function of frequency and wavevector along the edge. To isolate the fields of the photonic crystal modes, the spatial filter is modified to block direct reflection from the slab and the substrate below (see appendix Fig. 4.A.2c). Figure 4.5c displays the measured Stokes parameter  $S_3$  — which quantifies the detected circularly polarized intensity — normalized to the maximum value of total intensity of the polarized component. We see that only the edge states exhibit a significant degree of CP. Their opposing helicity is evident: The emission of the negative pseudospin state with negative group velocity is mostly left CP and that of the positive pseudospin state with positive group velocity is mostly right CP. In other words, we directly observe the pseudospin of the topological edge states, and the experiments reveal a clear signature of the photonic spin-orbit coupling that lies at the root of the QSHE. The measured far-field polarization is in good agreement with the results of the tight-binding model, whose parameters are fitted to the observed frequencies. We find that, also with the inclusion of the higher-order coupling terms, the average dipole moment remains CP. This behaviour is illustrated in Fig. 4.5d which shows the Stokes parameter  $S_3$  calculated by our theoretical model for edge as well as bulk modes.

## 4.5. Symmetry breaking and spin-spin scattering

Topological protection in our system is linked to a ‘pseudo’ time-reversal symmetry, which needs the preservation of  $C_6$  symmetry while deforming the honeycomb lattice unit cells [29]. However, at the interface between two deformed lattices,  $C_6$  symmetry breaking is unavoidable. This results in photonic spin-spin scattering — coupling of the counter-propagating edge states that opens a small gap around the  $\Gamma$  point [154]. With the inclusion of higher-order coupling terms, a small anticrossing between the two edge states is predicted by the tight-binding model, as can be seen in Fig. 4.5d. We see this also in experiment as a discontinuity around 200 THz in Fig. 4.5a and b. The amount of spin-spin scattering and thus the intrinsic limit to topological protection in photonic crystals can be recognized from this gap.

Here, we use Fourier spectroscopy as an effective method to probe even small amounts of scattering and investigate the limits to spin-orbit coupling in photonics. To quantify the anticrossing in our system experimentally, we take a closer look at the dispersion of states living at the two possible types of interfaces between shrunken and expanded lattices: (i) an armchair edge and (ii) a zigzag edge. The leftmost panels Fig. 4.6a and b show cartoons of the two edges. Taking a crosscut at  $k_y = 0$  in the measured dispersion maps (center panel in Fig. 4.6a and b) of the two edges for diagonally polarized input, and plotting the reflected intensity normalized to that from a silver mirror around the  $\Gamma$  point, show the anticrossing in the two edges (right panels in Fig. 4.6a and b). For each edge, the reflectance at  $k_y = 0$  is fitted with

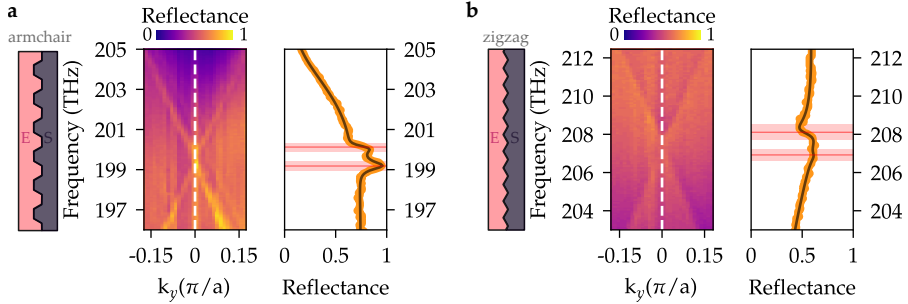


**Figure 4.6: Quantifying spin-spin scattering in the system: a, b.** Measured reflectance showing dispersion of armchair and zigzag edge states, respectively, as a function of wavevector  $k_y$ . Sketches of the edges are shown in the left panels. Measured intensity along the cross-cut indicated by the white line in the dispersion is shown in each of the right panels (orange data). The black line shows a fit with a set of complex Lorentzians (see appendix 4.A.4). Red lines and shaded areas correspond to the extracted resonance frequencies and linewidths.

two complex Lorentzians together with a slowly varying background (see appendix 4.A.4 for a discussion on the fitting model). The armchair and zigzag edge states are split by gaps of 1.0 THz and 1.2 THz, respectively. This corresponds quite well to predictions of the tight-binding model. For an armchair waveguide, the tight-binding model, whose parameters were obtained from fitting to bulk simulation data independently of the gap, predicts a gap of 0.6 THz. We do note that the bandgaps predicted by finite element calculations were somewhat smaller ( $\sim 0.1$  THz for the armchair edge and  $\sim 0.8$  THz for the zigzag edge). Further studies should determine whether spin-spin scattering is practically limited by fundamental symmetry breaking at the interface, or by other factors including fabrication disorder.

We also quantify the edge-state losses from the reflectance fit. Shaded regions in Fig. 4.6b depict the fitted linewidths of the modes, which exhibit quality factors ( $Q$ ) of 413 and 486. These deviate not far from the  $Q \approx 604$  predicted by FEM simulation (obtained from the linewidth of edge modes in Fig. 4.4b). The difference could be due to structural disorder, deviation of hole shape with respect to the designed (simulated) structure, or interaction of the propagating mode with radiation fields reflected from the Si substrate. Nonetheless, we conclude that the edge states propagate over distances of many wavelengths in the photonic crystal slab, even though their fundamental Bloch component is inherently phase-matched to the free-space continuum.

A smaller factor of expansion or shrinking in the corresponding bulk lattices would mean a smaller amount of  $C_6$  symmetry breaking across the edge, and we expect radiation losses as well as spin-spin scattering to reduce further for such smaller sizing factors of the shrunken and expanded unit cells. To test this hypothesis, we define a quantity which we call sizing factor,  $sf$ , denoting



the deviation of the unit cells in expanded or shrunken lattices from the unit cell in an ordinary graphene-like lattice. The sizing factors  $sf_e$  and  $sf_s$  tell us how ‘expanded’ or ‘shrunk’ the bulk lattices are: They determine the radial position of the triangular holes within a unit cell in such a way that the holes are situated at  $R_e = (1 + sf_e)a/3$  and  $R_s = (1 - sf_s)a/3$ , respectively, from the center of the unit cells, where  $a$  is the lattice periodicity. In Fig. 4.7, we plot the calculated eigenfrequencies at the  $\Gamma$  point for zigzag edges formed by different combinations of  $sf_e$  and  $sf_s$  from finite element simulations.

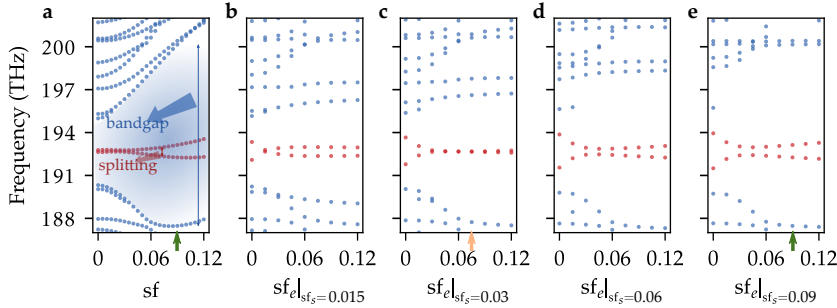


**Figure 4.7: Effect of shrinking or expansion factor in spin-spin scattering and topological bandgap:** **a.** Eigenfrequencies at the  $\Gamma$  point (red markers denote edge modes and blue markers denote bulk modes) calculated by finite element simulations as a function of deformation of bulk lattices from an ordinary lattice (see the text for definition of  $sf$ ). The green arrows mark the sizing factor of the samples used in experiments. **b–e.** Eigenfrequencies calculated at the  $\Gamma$  point against  $sf_e$  when  $sf_s$  is 0.015, 0.03, 0.06 and 0.09, respectively.<sup>1</sup>The orange arrow in **b** corresponds to the sizing factor combination offering the smallest splitting of edge states.

First we calculate eigenfrequencies as a function of a single quantity  $sf = sf_s = sf_e$  and plot these in Fig. 4.7a. The red markers correspond to the edge modes and the blue markers denote the bulk modes. The sizing factor in the samples that we used in the experiments is indicated by a green arrow in the horizontal axis ( $sf_e = sf_s = 0.09$ ). We can see that the splitting between edge states reduces as we reduce the sizing factor. However, this simultaneously reduces the bandgap width (blue shaded region). This would correspond to a smaller transverse confinement of the edge mode, requiring larger waveguide footprints. To find if spin-spin scattering can be reduced without decreasing confinement, we widen the parameter space by varying  $sf_e$  and  $sf_s$  separately. Plotted in Fig. 4.7b–e are calculated eigenfrequencies at the  $\Gamma$  point as a function of  $sf_e$  when  $sf_s$  is 0.015, 0.03, 0.06 and 0.09 respectively. We find in fact that very small splitting ( $\sim 0.01$  THz) occurs at finite gap size, when  $sf_e = 0.075$  and  $sf_s = 0.03$ , indicated by the orange arrow, in Fig. 4.7c.

<sup>1</sup>Some eigenfrequencies are not found by the solver; in particular, the first Bloch mode above the gap in c–e. Given the general dependence of states with  $sf$ , it however does not affect our conclusions.

Further studies should uncover the nature of this apparent closing of the spin-spin scattering gap, and prove its absence experimentally.

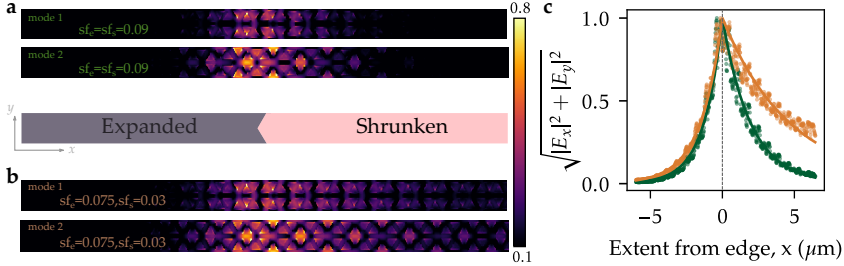


**Figure 4.8: Transverse extent of the edge modes:** **a, b.** Calculated norm of the in-plane electric field for edge modes when the combinations of sizing factors correspond to  $(sf_e, sf_s) = (0.09, 0.09)$  and  $(0.075, 0.03)$ , respectively, (corresponding to the green and orange arrows in Fig. 4.7). **c.** Integrated norm along  $y$  against transverse extent calculated for the second edge modes in **a** (green markers) and **b** (orange markers). Green and orange solid lines indicate an exponential decay fit to the data.

Figure 4.8 shows the FEM-calculated transverse extent of the edge mode fields for sizing factor combinations denoted by green and orange arrows in Fig. 4.7. The norm of the in-plane electric field components,  $(|E_x|^2 + |E_y|^2)^{1/2}$ , calculated at the surface of the photonic crystal with  $sf_e = sf_s = 0.09$  for the two edge states are plotted in Fig. 4.8a. A schematic of the simulation box with the location of the edge is shown in the bottom panel of Fig. 4.8a. Comparing to the edge modes for sizing factors of  $sf_e = 0.075$  and  $sf_s = 0.03$  (Fig. 4.8b), the modes in Fig. 4.8a have less extent to the bulk lattices.

We also notice an asymmetry in the mode extent. The fields leak more into the shrunk region than into the expanded. This becomes more obvious if we plot the integrated electric field norm value along the  $y$  direction as a function of transverse direction  $x$ , as shown in Fig. 4.8c. Green and orange markers correspond to the integrated norm values of the second mode in Fig. 4.8a and b, respectively. Fitted to the data are single exponential decay curves (solid green and orange lines) to find the decay lengths in the shrunk and expanded lattices. For the sizing factor combination with more spin-spin scattering ( $sf_e = sf_s = 0.09$ ), the decay length in the expanded and shrunk lattices are  $\sim 1.3 \mu\text{m}$  and  $\sim 2 \mu\text{m}$ , respectively. For the orange combination ( $sf_e = 0.075$ ,  $sf_s = 0.03$ ), the decay lengths are  $\sim 1.5 \mu\text{m}$  and  $\sim 4.7 \mu\text{m}$ , respectively. The asymmetry in the mode extent for a given mode arises from the difference between bandgaps of shrunk and expanded lattices. The mode decays more into the lattice with smaller bandgap (shrunk in this case). Thus, we can conclude that there is a certain trade-off between the spin-spin scattering and the transverse mode extent. However, the reduced confinement is modest compared to the  $\sim 100$ -fold decrease in spin-spin scattering for these parameters. It would be interesting to explore how other strategies in

reducing the spin-spin scattering, including design of microscopic structure, allow minimizing loss and backscattering while simultaneously optimizing the confinement.

## 4.6. Conclusions

To conclude, we have directly observed topologically-protected edge states for light at telecom wavelengths in a silicon photonic platform. We characterized their dispersion, loss and polarization. We demonstrated that the pseudospin of the states is inherently encoded in the circular polarization of their far fields. The employed Fourier spectroscopy technique makes it possible to quantify the inherent spin-spin scattering of the system, opening doors to further understanding and control of topological protection in QSHE systems, as well as the connections between chirality and topology [155]. It establishes a straightforward yet versatile path for testing and optimizing novel topological systems for a wide variety of applications in optics, including components for integrated photonic chips, quantum optical interfaces, enantiomeric sensing, and lasing at the nanoscale, as well as in other bosonic domains.

## APPENDICES

### 4.A. Experimental methods

#### 4.A.1. Sample design and FEM simulations

We used finite element method (FEM) simulations (COMSOL Multiphysics 5.2) to optimize the design parameters such that the system can offer topological protection at telecom wavelengths, with both expanded and shrunk lattices exhibiting bandgaps around 1550nm. A fillet of 25nm radius was added to the triangular corners to account for the roundedness of holes in fabrication. The periodicity of the photonic crystal was 800nm. As indicated in Fig. 4.A.1, equilateral triangles of 250nm side were arranged in hexagonal clusters, with the distance from the center of the cluster to the center of the triangle being 243nm for shrunk and 291nm for the expanded lattice. Simulations were done for a slab of 220nm with a silicon refractive index of 3.48. Perfectly matched layers were added above the simulation box so that simulations of the (quasinormal) eigenmodes also yield their linewidth, which we define as two times the imaginary part of the complex eigenfrequency.

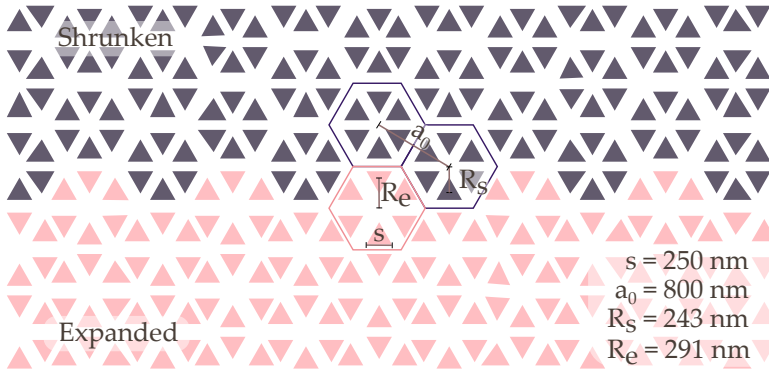


**Figure 4.A.1: Design parameters for shrunk and expanded lattices:** The unit cell period  $a_0 = 800$  nm and the length of the triangle sides  $s$  are the same for both lattices. The distance from the center of the unit cell to the center of the triangle was different for shrunk ( $R_s = 243$  nm) and expanded ( $R_e = 291$  nm) lattices.

Figure 4.A.1 shows different geometric parameters of the simulated systems. The radial positions of triangular holes in expanded and shrunk lattices with respect to the centre of the unit cell are defined as  $R_e = (1 + sf_e)a/3$  and  $R_s = (1 - sf_s)a/3$ , respectively. Figure 4.A.1 shows the values when  $sf_e = sf_s = 0.09$ . These parameters were employed in the design of the samples used for experiments.

### 4.A.2. Sample Fabrication

The samples were fabricated from a silicon on insulator wafer with a 220nm silicon device layer on top of a 3 $\mu$ m buried oxide layer which sits on a 700 $\mu$ m thick substrate. A positive tone electron beam (e-beam) resist, AR-P 6209, was spin-coated on top of the waferchips to form a 250nm thick resist layer. The photonic crystal designs were patterned in the resist using e-beam lithography (Raith Voyager, 50kV). The resist was developed with Pentyl-acetate/O-xylene/MIBK(9):IPA(1)/IPA. The designed pattern was transferred into the Si device layer using HBr/O<sub>2</sub> inductively coupled plasma etching (Oxford Instruments Plasmalab 100 Cobra). Anisole (5 min) was used to remove the left-over resist and the sample was cleaned using base piranha (H<sub>2</sub>O(5):NH<sub>4</sub>OH(1):H<sub>2</sub>O<sub>2</sub>(1)) treatment for 15 minutes at 75°C. To obtain free-standing photonic crystal membranes, the oxide layer was wet-etched with HF, followed by critical point drying.

The main sample had an armchair-like edge of  $\sim 380\mu\text{m}$  length which separates shrunken and expanded lattices having widths of  $\sim 196\mu\text{m}$  each. Figure 4.B.1b shows an optical micrograph of this sample.

### 4.A.3. Experimental Details

#### Dispersion Measurements

A 200mW supercontinuum source (Fianium WhiteLase Micro) generates light with a broadband spectrum. Its output is filtered by a long pass filter with cutoff wavelength at 1150nm and coupled into a single mode optical fibre. The infrared light from the fibre is collimated by an achromatic lens and passed through an OD:1 neutral density filter, a linear polarizer (LP) and an achromatic quarter-wave plate (QWP), which together define the polarization of the input beam. A beamsplitter (BS) steers the input light to an aspheric objective (Newport 5721-C-H, 60x, NA=0.6) which focuses light on the sample. Reflected light is collected by the same objective and passed through the beamsplitter to the Fourier lens placed in the output path. This lens, together with a tube lens, images the objective back-focal plane (BFP) onto the entrance slit of a spectrometer (Acton SpectraPro SP-2300i). Optional custom spatial filters are placed in the image plane between the Fourier lens and tube lens to define the sample area from which light is collected. The (vertical) entrance slit of the spectrometer, aligned with the optical axis, chooses  $k_x = 0$  in the reciprocal plane, confirmed using a test grating sample. With the help of two parabolic mirrors for focusing and collection, the spectrometer grating then disperses the broadband infrared light orthogonal to the slit, such that the InGaAs infrared camera (AVT Goldeye G-008 SWIR) placed at the spectrometer output records images of frequency versus  $k_y/k_0$ , where  $k_0$  is the free-space wavevector. The spectral resolution is 81.5GHz, and the wavevector resolution  $\Delta k_y/k_0 \approx 0.011$ . The wavevector axis was calibrated by observing the diffraction of a gold transmission grating with known pitch placed at the

sample position. The frequency axis was calibrated using laser sources of known wavelength. Reflectometry images taken at different centre frequencies of the grating are stitched together in post-processing to plot dispersion over a wide range of frequencies.

### Polarimetry Measurements

We use the ‘rotating QWP’ scheme outlined in Ref. [153] to measure the Stokes polarization parameters. We place a QWP and LP after the Fourier lens so that the reflected beam passes through them sequentially. For a given rotation angle  $\theta$  of the QWP, the detected intensity can be written in the form of a truncated Fourier series

$$I(\theta) = \frac{1}{2}(A + B\sin 2\theta + C\cos 4\theta + D\sin 4\theta), \quad (4.A.1)$$

where the Fourier coefficients  $A, B, C$  and  $D$  are related to the measured Stokes parameters as  $S'_0 = A - C$ ,  $S'_1 = 2C$ ,  $S'_2 = 2D$  and  $S'_3 = B$ . For our polarimetry measurements, we take 12 successive measurements rotating the QWP from  $\theta_1 = 0^\circ$  to  $\theta_{12} = 165^\circ$  in steps of  $15^\circ$  to find these coefficients as:

$$\begin{aligned} A &= \frac{2}{12} \sum_{n=1}^{12} I(\theta_n), & B &= \frac{4}{12} \sum_{n=1}^{12} I(\theta_n) \sin 2\theta_n, \\ C &= \frac{4}{12} \sum_{n=1}^{12} I(\theta_n) \cos 4\theta_n, & D &= \frac{4}{12} \sum_{n=1}^{12} I(\theta_n) \sin 4\theta_n. \end{aligned} \quad (4.A.2)$$

The LP after the QWP is fixed at  $0^\circ$  with respect to the  $\hat{x}$  axis in all these measurements.

The collected light is not fully polarized. The polarized component for a given output is defined as  $I_p = \sqrt{S_1'^2 + S_2'^2 + S_3'^2}$ . We normalize the measured Stokes parameters to the maximum value of the polarized component in the output as  $S_i = S_i' / \max(I_p)$  for  $i = 1, 2, 3$ . Results of full polarization tomography of the edge states is given in Supplementary Fig. S5.

Contributions from background reflections can be important while studying the Stokes parameters of a resonant mode’s radiation, as the observed polarization of the superposition of both fields can depend strongly on their (uncontrollable) relative phase. We isolate the edge-mode radiation in the far field from the direct reflection components by altering the spatial filter. Figure 4.A.2 shows sketches of the employed spatial filters, determining the collection area during edge state dispersion measurements without and with a center-block. With the latter, collection of direct reflections from the illumination spot is prevented, but radiation from edge states that propagate out of the center spot is detected.

### Spatial filtering

Figure 4.A.2a and b show schematic representations of the collection area at the sample in real space without and with the spatial filter, respectively.

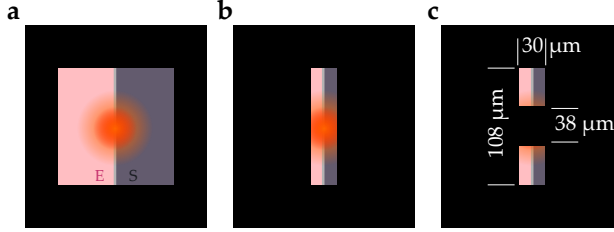


**Figure 4.A.2:** The modification of the spatial filter placed in a real-space image plane in the detection path to isolate the contribution from edge modes for the  $S_3$  measurement: **a.** A cartoon of the real-space plane without the slit. The illumination spot is indicated in orange. **b.** The slit defines the sample area from which light is collected. **c.** Putting a central block across the slit blocks most of the illumination spot, only allowing light originating from the edges to pass. Dimensions of the effective collection area at the sample as well as the dimension of the blocked region are marked along the sides.

For polarimetry measurements on the edge, the collection area was modified by putting a block at the centre of the slit, as shown in Fig. 4.A.2c.

#### 4.A.4. Extraction of modes from dispersion crosscut

To the normalized reflection obtained from the cross-cut in Fig. 4.6a, we fit a set of complex Lorentzians of the form:

$$R(\omega) = \left| A_0 + \sum_{j=1}^3 A_j e^{i\phi_j} \frac{\gamma_j}{\omega - \omega_{0j} + i\gamma_j} \right|^2, \quad (4.A.3)$$

where  $A_0$  is a constant background amplitude;  $A$ ,  $\phi$  and  $\omega_0 - i\gamma$  are the amplitude, phase and complex frequency of three individual Lorentzians. Quality factors are defined as  $Q_j = \omega_{0j} / (2\gamma_j)$ . Two of these Lorentzians model the edge modes, while the third (broad) Lorentzian accounts for the slowly varying background reflection.

## 4.B. Direct Fabry-Pérot reflections and reflectometry of an ordinary lattice

Here we comment on the broad low-reflection fringes in our dispersion measurements. The  $3\mu\text{m}$  air cavity formed between the suspended photonic crystal and the Si substrate can effectively act as a Fabry-Pérot cavity and can contribute to the measured reflected intensity of the sample.

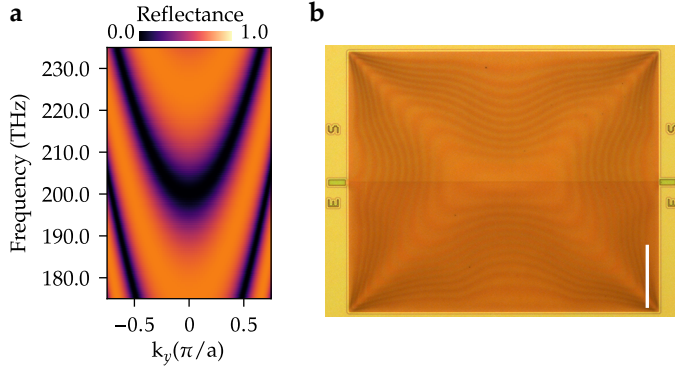


**Figure 4.B.1:** **a.** Analytically calculated Fabry-Pérot-like fringes for an air cavity between two Si layers. **b.** Optical micrograph of the fabricated sample. The scalebar corresponds to 100  $\mu\text{m}$  on the sample.

To confirm this, we analytically calculate the reflection of an air cavity between two Si surfaces. As shown in Fig. 4.B.1a, the resulting parabolic dispersion curves are comparable to what we observe in the reflection measurements shown in the main text. The position of these curves shift in frequency as a function of height of the air layer. In our sample, the height of air cavity below the suspended membrane is different at different points in the photonic crystal. We see this buckling from the colour contrast in the optical micrograph as shown in Fig. 4.B.1b. This results in spectral shifting of the low-reflection fringes when we take dispersion measurements at expanded, shrunk and edge locations.

## 4.C. Orthogonal linear polarization of bulk modes

Here, we observe that the bulk modes are linearly polarized with orthogonal polarizations in the far-field. They can be selectively excited with vertical and horizontal polarizations.

Figure 4.C.1 shows photonic band dispersion in shrunk and expanded lattices when those are excited with light of different linear polarizations. Figure 4.3a and c of the main text is reproduced here as Fig. 4.C.1a and d, and shows the reflected light intensities as a function of the reciprocal lattice vector  $k_y$  when diagonally polarized light is incident on the sample. Here the bandgap region extends from 197 THz to 208 THz. Let us have a closer look at the two bands (marked as band-1 and band-2 in the figure) directly below the gap for shrunk and expanded lattices. These are bright modes for the shrunk and dark modes for the expanded lattices. Now, if we excite the sample with horizontally polarized light, we can see that the incident light excites only one of these two modes (band-1) as shown in Fig. 4.C.1b and e.



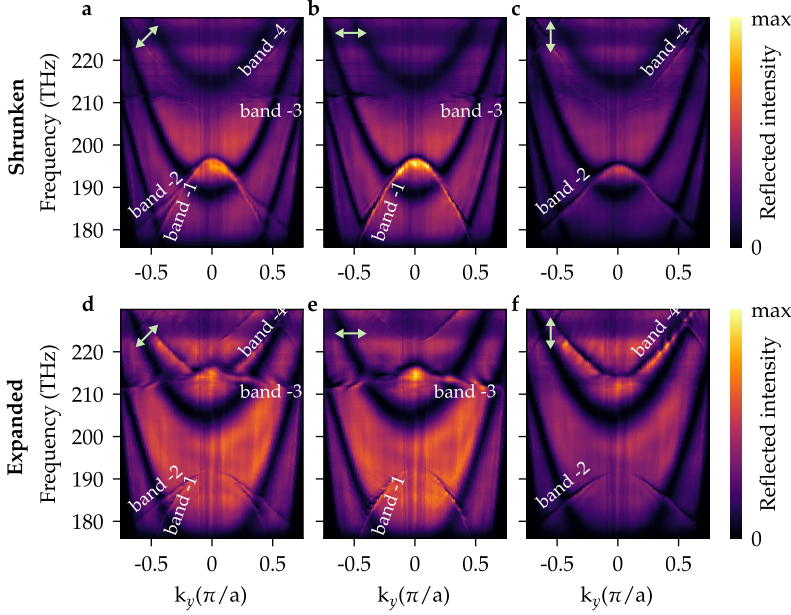


**Figure 4.C.1: Dispersion of bulk modes for orthogonally polarized incidences:** a-c. Far-field reflection as a function of  $k_y/k_0$  at the shrunk lattice, excited with light that is linearly polarized along  $45^\circ$  with respect to  $x$  (a), along  $x$  (b), and along  $y$  (c). d-e. Corresponding dispersion measurements on the expanded lattice. The four linearly polarized bulk modes are marked as band-1 to band-4 in a and d.

However, for vertically polarized incidence, it is the other mode (band-2) that is getting excited as we see in Fig. 4.C.1c and f. This suggests that band-1 is horizontally polarized and band-2 is vertically polarized. Thus, the two bands below the gap are linearly polarized, orthogonal to each other.

We see a similar behaviour also in the bands above the gap. As we see in Fig. 4.C.1b and e, band-3 is excited for horizontally polarized incidence. And for vertically polarized incidence, band-4 is excited, as can be seen from Fig. 4.C.1c and f.

## 4.D. Tight-binding model

Here we extend the tight-binding model outlined in Ref. [142] to support our experimental observations. In the existing model, the Hamiltonian of the system is calculated with a nearest neighbour approximation, making a linear approximation in reciprocal lattice vectors  $k_x$  and  $k_y$ . The model also restricts the six-dimensional basis to a four-dimensional system. These two assumptions, however, result in the prediction of fully degenerate bulk states and gapless edge states. We expand the theory by going beyond these

assumptions.

We consider a six-dimensional vector  $|\psi\rangle$ , where each component represents one of the six sites in a hexagonal unit cell. We observe that in order to get results in agreement with the experiments, it is required to include next-neighbour interaction up to third order in the model. The tight-binding Hamiltonian reads:

$$H = - \begin{pmatrix} 0 & t_1 + W_1 & t_2 + V_1 & t_3 + U_1 & t_2 + V_5 & t_1 + W_6 \\ 0 & 0 & t_1 + W_2 & t_2 + V_2 & t_3 + U_2 & t_2 + V_6 \\ 0 & 0 & 0 & t_1 + W_3 & t_2 + V_3 & t_3 + U_3 \\ 0 & 0 & 0 & 0 & t_1 + W_4 & t_2 + V_4 \\ 0 & 0 & 0 & 0 & 0 & t_1 + W_5 \\ 0 & 0 & 0 & 0 & 0 & 0 \end{pmatrix} + H. c., \quad (4.D.1)$$

where, for the sake of compactness, we define the auxiliary vectors

$$U = s_1(e^{ik \cdot a_1}, e^{ik \cdot a_2}, e^{ik \cdot (a_2 - a_1)})^\top, \quad (4.D.2)$$

$$V = s_2(e^{ik \cdot a_1} + e^{ik \cdot (a_1 - a_2)}, e^{ik \cdot a_1} + e^{ik \cdot a_2}, e^{ik \cdot a_2} + e^{ik \cdot (a_2 - a_1)}, \\ e^{-ik \cdot a_1} + e^{ik \cdot (a_2 - a_1)}, e^{ik \cdot a_1} + e^{ik \cdot a_2}, e^{ik \cdot a_2} + e^{ik \cdot (a_2 - a_1)})^\top, \quad (4.D.3)$$

$$W = s_3(e^{ik \cdot (a_1 - a_2)}, e^{ik \cdot a_1}, e^{ik \cdot a_2}, e^{ik \cdot (a_2 - a_1)}, e^{-ik \cdot a_1}, e^{ik \cdot a_2})^\top, \quad (4.D.4)$$

and the lattice unit vectors  $\mathbf{a}_1 = (a, 0)^\top$  and  $\mathbf{a}_2 = a/2(1, \sqrt{3})^\top$ . Here,  $H. c.$  stands for the Hermitian conjugate and  $a$  is the lattice periodicity. We also designate the intra-cell coupling coefficients for first-, second-, and third-nearest neighbours as  $t_1$ ,  $t_2$ , and  $t_3$ , respectively. Similarly, we indicate with  $s_1$ ,  $s_2$ , and  $s_3$  the inter-cell coupling coefficients.

The modes in the photonic crystal are mostly TE polarized. Therefore, we assume that the six components of  $|\psi\rangle$  correspond to the field component  $H_z$  at the six lattice sites. For a TE mode, the in-plane electric field components are proportional to:

$$E_x \propto -\frac{\partial H_z}{\partial y}, \quad E_y \propto \frac{\partial H_z}{\partial x}. \quad (4.D.5)$$

We assume that inside each hexagonal unit cell, the field varies mostly along the angular dimension  $\theta$ , i.e.,  $H_z \simeq H_z(\theta)$  and that the variation of  $H_z$  between one site and another is such that the variable can be considered continuous. Thus, moving to cylindrical coordinates, the electric field components become:

$$E_x \simeq \cos(\theta) \frac{\partial H_z}{\partial \theta}, \quad E_y \simeq \sin(\theta) \frac{\partial H_z}{\partial \theta}, \quad (4.D.6)$$

so that we can write  $E \simeq \hat{\mathbf{R}} \partial_\theta H_z$ , where  $\hat{\mathbf{R}}$  is the radial unit vector from the centre of the unit cell.

The polarization density is proportional to the electric field:  $\mathbf{P} = \chi \mathbf{E}$ . We are interested in the total dipole moment inside the unit cell

$$\mathbf{p} = \int_{\text{cell}} d\mathbf{r} \mathbf{P}(\mathbf{r}). \quad (4.D.7)$$

Using the previous assumptions, we can approximate the total dipole moment as follows:

$$\mathbf{p} \propto \int_0^{2\pi} d\theta \hat{\mathbf{R}}(\theta) \frac{\partial H_z}{\partial \theta}. \quad (4.D.8)$$

By partial integration, this becomes

$$\mathbf{p} \propto \int_0^{2\pi} d\theta \frac{\partial \hat{\mathbf{R}}(\theta)}{\partial \theta} H_z(\theta) \propto \int_0^{2\pi} d\theta \hat{\boldsymbol{\theta}} H_z(\theta). \quad (4.D.9)$$

where  $\hat{\boldsymbol{\theta}}$  is the unit vector along the azimuthal direction.

Now we can go back to the discretized system and replace the integral over  $\theta$  with the sum over the six sites of the hexagon. In this way, we obtain the following estimation for the total dipole moment inside the unit cell

$$\mathbf{p} \propto \sum_{i=1}^6 \hat{\boldsymbol{\theta}}_i \psi_i, \quad (4.D.10)$$

where  $\hat{\boldsymbol{\theta}}_i$  is the azimuthal unit vector of the  $i^{\text{th}}$  site in the unit cell, assuming the origin to be located at the centre of the hexagon. In practice,  $\hat{\boldsymbol{\theta}}_i = (-\sin[(i-1)\pi/3], \cos[(i-1)\pi/3])^\top$ , with  $i = 1, \dots, 6$ .

We fitted the parameters  $t_1, t_2, t_3$  and  $s_1, s_2, s_3$  of the Hamiltonian to reproduce the bandstructure calculated with the FEM for both the expanded and the reduced crystals. In Fig. 4.D.1, we compare the FEM results with the tight-binding method. We observe that including higher-order-interaction terms into the tight-binding Hamiltonian is essential for correctly reproducing the splitting of the bands away from the  $\Gamma$  point. Moreover, the dipole moment calculated from Eq. (4.D.10) confirms that the bulk modes are linearly polarized in the far field, in full agreement with our experiment.

We can also use the tight-binding model to calculate the edge states. In order to do so, we consider the following system: two regions of space,  $A$  and  $B$ , separated by an edge at  $x = 0$ . In regions  $A$  and  $B$  we have the shrunken and expanded crystals with the Hamiltonians  $H_A$  and  $H_B$ , respectively. Both Hamiltonians have the form in Eq. (4.D.1), but each with a different set of parameters. Each Hamiltonian is a function of  $k_x$  and  $k_y$ . Since the model is still translation-invariant along  $y$ ,  $k_y$  is conserved. However,  $k_x$  is not conserved and, therefore, needs to be replaced with a corresponding differential

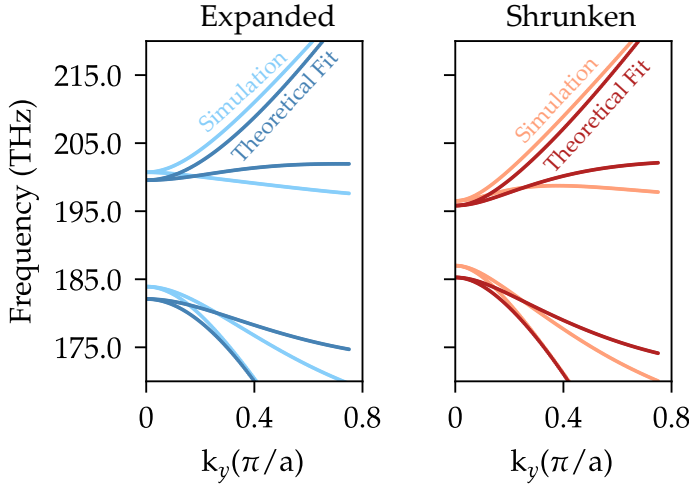


**Figure 4.D.1: Comparison of bandstructure calculations for bulk lattices:** Finite element method (FEM) simulation vs tight-binding model. The lighter lines correspond to dispersion calculated by FEM simulation whereas the darker lines correspond to dispersion predicted analytically by our tight-binding model. The left and right panels show the dispersion in the expanded and the shrunkun lattice, respectively.

operator, according to the substitution  $k_x = -i\partial_x$ . For simplicity, we expand both Hamiltonians  $H_A(k_x, k_y)$  and  $H_B(k_x, k_y)$  to first order in Taylor series

$$\begin{aligned}
 H_{A,B} &\simeq H_{A,B}(\mathbf{0}) \\
 &+ k_x \left. \frac{\partial H_{A,B}}{\partial k_x} \right|_{k_x=0, k_y=0} \\
 &+ k_y \left. \frac{\partial H_{A,B}}{\partial k_y} \right|_{k_x=0, k_y=0}.
 \end{aligned} \tag{4.D.11}$$

For the edge states, we consider only the frequencies inside the bandgap of the bulk modes. Therefore, there are no propagating solutions for the Schrödinger equation of the Hamiltonians  $H_A$  and  $H_B$ . However, there are evanescent solutions, which are defined by the (generalized) eigenvalue problems for  $k_x = i\delta^{(A)}$  and  $k_x = i\delta^{(B)}$  in the two regions separately:

$$\left[ \omega - H_A(\mathbf{0}) - k_y \left. \frac{\partial H_A}{\partial k_y} \right|_0 \right] |\psi_m^{(A)}\rangle = i\delta_m^{(A)} \left. \frac{\partial H_A}{\partial k_x} \right|_0 |\psi_m^{(A)}\rangle, \tag{4.D.12}$$

$$\left[ \omega - H_B(\mathbf{0}) - k_y \left. \frac{\partial H_B}{\partial k_y} \right|_0 \right] |\psi_m^{(B)}\rangle = i\delta_m^{(B)} \left. \frac{\partial H_B}{\partial k_x} \right|_0 |\psi_m^{(B)}\rangle. \tag{4.D.13}$$

Here, the index  $m$  runs over the different eigenvalues and eigenvectors of the two equations. These eigenvalue equations imply that the solutions of the

Schrödinger equation for  $|\psi\rangle$  can be written as

$$|\psi(x)\rangle = \sum_{m=1}^3 \alpha_m^{(A)} |\psi_m^{(A)}\rangle \exp(|\delta_m^{(A)}| x) \quad (4.D.14)$$

in region  $A$  (say,  $x < 0$ ), and

$$|\psi(x)\rangle = \sum_{m=1}^3 \alpha_m^{(B)} |\psi_m^{(B)}\rangle \exp(-|\delta_m^{(B)}| x) \quad (4.D.15)$$

in region  $B$  ( $x > 0$ ). In both cases,  $\alpha_m^{(A,B)}$  are expansion coefficients.

In order to find the frequencies of the edge states, we have to enforce a continuity condition at the point  $x = 0$ :

$$\sum_{m=1}^3 \alpha_m^{(A)} |\psi_m^{(A)}\rangle = \sum_{m=1}^3 \alpha_m^{(B)} |\psi_m^{(B)}\rangle. \quad (4.D.16)$$

This condition leads to the characteristic equation for the determinant of a  $6 \times 6$  matrix, which we solve numerically. The solutions of the characteristic equation correspond to the frequencies of the edge states for a given value of  $k_y$ .

Moreover, from the coefficients  $\alpha_m^{(A)}$  and  $\alpha_m^{(B)}$  we can reconstruct the profile of the edge state along the  $x$  axis. Using Eq. (4.D.10), we can compute the local cell-averaged dipole moment,  $\mathbf{p}(x)$ . Finally, the total dipole moment of the edge state is calculated by integrating along  $x$ , i.e.,

$$\mathbf{p}_{\text{tot}} = \int dx \mathbf{p}(x). \quad (4.D.17)$$

The frequencies of the edge states calculated with this method and the  $S_3$  parameter derived from the corresponding total dipole moments are shown in Fig. 4.5d in the main text.

## 4.E. Polarization tomography of edge states

For the sake of completeness, in Fig. 4.E.1 we show the full polarization tomography of the edge states for horizontally and vertically polarized incidences.

Figure 4.E.1 shows the measured Stokes parameter  $S'_0$ , the intensity of the polarized component in the reflected signal  $I_p = (S_1'^2 + S_2'^2 + S_3'^2)^{1/2}$ , and the normalized values  $S_1$ ,  $S_2$  and  $S_3$  (normalized to the maximum value of the polarized component  $I_p$ , as mentioned in appendix 4.A.3). The predominantly circularly polarized nature of the edge states, exhibiting opposite handedness,

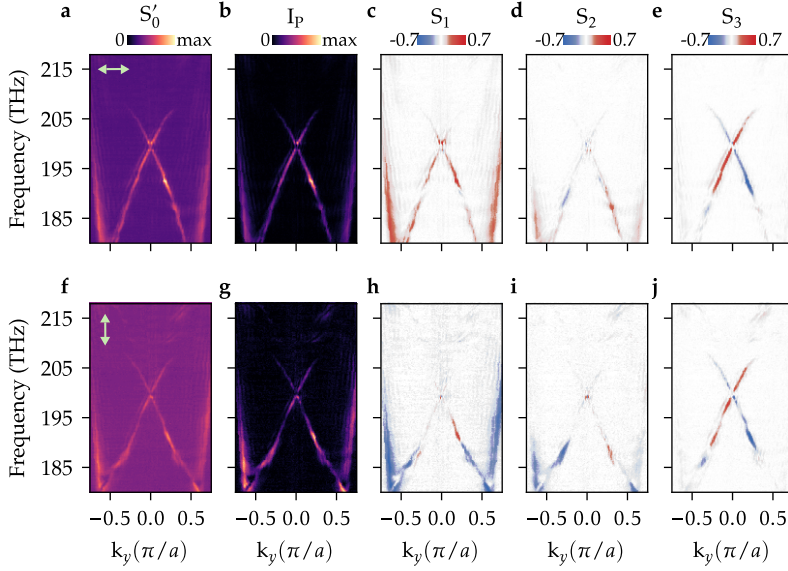


**Figure 4.E.1: Polarization tomography of the edge states:** Intensity of the polarized reflected field and various Stokes parameters of the edge states for incident light linearly polarized along  $\hat{x}$  (a-e) and  $\hat{y}$  (f-j).

is clear from panels e and j. The anticrossing region, in contrast, is characterized by linear polarization (panels c, d, h and i). We attribute the remaining linear polarization for lower frequencies in panels c, d, h and i to experimental imperfection and to the fact that the observed dispersion curves merge there with bulk states below the lower band edge.

# 5

## CONFINING AND GUIDING LIGHT IN TOPOLOGICAL PHOTONIC CRYSTALS

*“Don’t adventures ever have an end? I suppose not.  
Someone else always has to carry on the story.”*

— J. R. R. Tolkien, *The Fellowship of the Ring*, 1954

*We image the propagation of topological photonic crystal edge states through their far-field radiation as well as using near-field scanning probe microscopy. We study the polarization and position-dependent local excitation of edge states with a focused laser beam. We investigate the routing of edge states in sharp junctions between different topological domains. We show that edge states can be confined in ring cavities, and that these can be effectively coupled to waveguides while conserving optical spin. Finally, we demonstrate the potential of phase-resolved near-field microscopy in analysing edge state dispersion and fields at the nanoscale.*

---

Parts of this chapter have been reported in the preprint arXiv:1811.10739 (2018) [120].  
The (unpublished) near-field measurements in Sec. 5.6 were done in collaboration with T.A. Bauer and S. Arora at Delft University of Technology.

## 5.1. Introduction

The development of systems to guide and manipulate light on-chip has received a lot of attention in the past decades, in particular in the context of integrated silicon photonics [9, 156]. In the previous chapter, we saw the existence of a new class of photonic waveguides formed by the interface between two photonic crystals, which host topological states that feature spin to direction locking. These states could be interesting candidates for controlling and guiding light in photonic chips owing to their topological nature. This includes passive guiding [157–162], routing [163–166], confining (in cavities) [167–170] or coupling (or filtering) [171, 172] of light. Traditionally, this is achieved in high index media surrounded by low index media using the principle of total internal reflection [173, 174]. However, this approach suffers from losses and backscattering around bends and corners [21, 159, 175, 176]. To a certain degree, losses are also observed in photonic crystal waveguides such as single-row-defect (W1) waveguides [177–179], in particular due to the existence of backward-propagating modes to which light can easily scatter. Given the special origin of topological states and the principle of topological protection, it is interesting to see how their nature affects their propagation properties – including loss, confinement, and backscattering. The robustness of topological protection in this context can be potentially probed by making topological structures that form corners, junctions, cavities and (add-drop) filters/couplers.

To study the propagation of topological states in various structures, it is beneficial to be able to image the states in real space. Topological states have previously been imaged in various systems using a variety of techniques. Near-field techniques were employed to see the propagation of edge states around defects in the microwave domain [180–182]. In the optical domain, previous efforts for visualization of edge states include the use of scattered light from the individual sites in ring resonator arrays by Hafezi et al. [39], diffracted light at output facets of ‘straw’ waveguides by Rechtsman et al. [124, 132, 134], photoluminescence as polariton emission in coupled micropillars by Amo et al. [131] and nonlinear harmonic generation in nanopillar arrays by Kivshar et al. [183]. However, topological photonic crystals so far have only been characterized by input-output measurements at the waveguide ends [146, 148, 149]. The far-field nature of the states that we have seen in the previous chapter provides a direct means to visualize them and map their propagation inside waveguides and devices.

In this chapter, we demonstrate the imaging of protected edge states and use it to characterize topological waveguides, routing junctions, cavities and couplers for light. We show that it is possible to selectively launch a state in a topological edge waveguide by focusing polarized light at the edge. Using a chiral waveguide in combination with the pseudospin of the state, we present the possibility of effectively routing optical signals. Topological cav-



ities of different sizes and shapes are fabricated and directly characterized. We retrieve the cavity mode properties using dispersion measurements and reveal that while their quality factor does not depend much on size and shape, the free spectral range does. Employing polarized spectroscopy, we discover mode splitting for some of the modes, signalling limitations to topological protection. We create a cavity-waveguide coupling system and demonstrate add/drop filtering functionality in the topological photonic domain. This shows the important role of spin conservation in the coupling between waveguides and cavities. Finally, we demonstrate the near-field imaging of topological edge states using phase-resolved scanning near-field optical microscopy, and use it to analyze their dispersion.

## 5.2. Imaging guided light in topological waveguides

The radiation field of edge states encountered in the previous chapter enables mapping their propagation in real space, upon locally and selectively exciting them with polarized light. To visualize the propagation of edge states in real space, we image the interface between the shrunk and expanded lattices in a topological photonic crystal using a simple microscopy system consisting of an objective and a tube lens. A schematic diagram of the experimental setup used for microscopic imaging of guided light in topological waveguides is shown in Fig. 5.1. Details of the components used in the setup can be found in appendix 5.A.2.

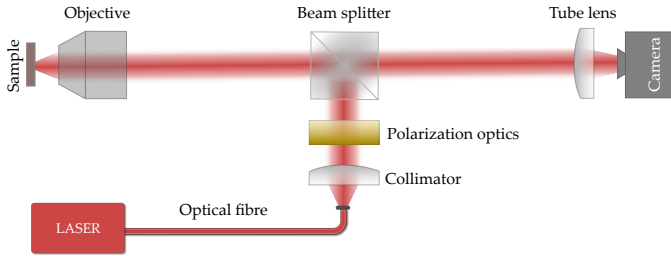


**Figure 5.1: Experimental setup for real-space imaging:** Collimated, polarized light from a monochromatic laser is focused onto the sample using an objective. The sample plane is imaged onto the camera. See appendix 5.A.2 for more details.

We have seen in Sec. 4.3 that the edge states follow a linear dispersion in the bulk bandgap. Choosing a single frequency from this range, we focus light from a monochromatic continuous-wave laser on an armchair interface between expanded and shrunk lattices. Figures 5.2b-d shows images taken with the infrared camera, when polarized laser light at 1512 nm is focused onto the edge. Exciting the sample using focused light ensures that the incident light contains a continuum of angles of incidence within the numerical aperture of the objective. On the one hand, this maximizes the chance of excitation

of a state at the supplied frequency (since there should be at least one angle for which an edge state exists at the supplied frequency) and creates a localized source. On the other hand, since only one angle out of the entire numerical aperture excites the state, this is not a very efficient way of excitation. Light from the rest of incident angles cannot couple to any state, and contributes to the reflection back from the surface of the sample, which is recorded as a high-intensity area around the excitation spot in reflection images. However, the edge states have a quality factor of  $\sim 450$  (as we saw in Sec. 4.5) and can propagate tens of micrometres away from the excitation spot. This helps us to still image their propagation along the edge.

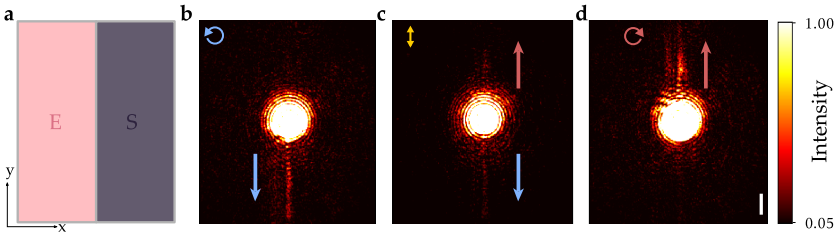


**Figure 5.2: Real-space images of edge state propagation:** **a.** A schematic diagram showing the edge between expanded (E) and shrunk (S) lattices, where a focused monochromatic laser excites the sample. **b-d.** Real space camera images when the incident light is left-circularly, linearly and right-circularly polarized, respectively. Images are normalized to the maximum pixel value among the three. The scalebar corresponds to 10  $\mu\text{m}$ . The camera was saturated in the central region.

We observe that the states show a high selectivity to the incident polarization. As we see in Fig. 5.2b, left-circularly polarized light excites only the positive pseudospin mode which propagates only in the downward direction. The upward-propagating negative pseudospin mode gets excited when the incident light is right-circularly polarized as Fig. 5.2d shows. It can be seen in Fig. 5.2c that propagation has equal preference for each direction when the edge is excited with linearly polarized light.

To study the transverse extent of the propagating mode, we scan the excitation spot across the armchair edge by moving the sample in the horizontal direction. Two images for right- and left-circularly polarized incident light are taken for each 250nm step in the movement of the excitation spot across an armchair edge between shrunk and expanded lattices. Figure 5.3b shows two such images when the sample position corresponds to approximately maximal excitation of the edge states (the horizontal axis of Fig. 5.3a is zeroed at this point). For either polarization  $R$  or  $L$ , we then define two areas  $U$  and  $D$  above and below the excitation spot as shown in Fig. 5.3a, in which we integrate the imaged intensity to estimate the edge state intensity launched to the top and bottom, respectively. For each polarization handedness, the difference of integrated intensities from the top and bottom areas,  $I_U - I_D$ , is plotted as

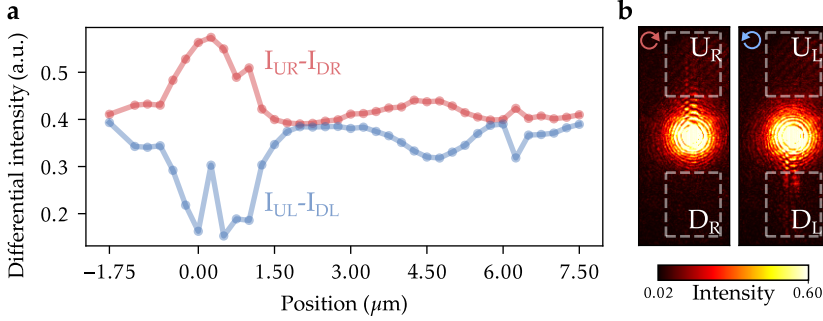


**Figure 5.3: Transverse extent of the edge modes:** **a.** The difference between integrated intensities in two areas  $U$  and  $D$  as defined in each panel of **b**, when a right- (red) and a left-circularly (blue) polarized excitation spot is moved across an armchair edge. The excitation position at  $0\mu\text{m}$  corresponds to an approximate centre of the waveguide. **b.** Images recorded for the excitation position  $0\mu\text{m}$ . The dashed rectangles correspond to the areas under which the intensity is integrated.

5

a function of different sample positions in Fig. 5.3a. Red markers correspond to right-circularly polarized incidence and blue markers correspond to left-circularly polarized incidence. The constant offset to the differential intensity ( $\sim 0.4$  on this scale) is due to some background light in the measurement. We first note that the direction into which topological edge states are launched (up or down) does not depend on the excitation spot position, but only on the incident polarization. Right circularly polarized incident light always excites states in the upwards direction and left circularly polarized excitation leads to downward guidance, as seen from the opposite behaviour of the red and blue curves. Thus, the spin-orbit coupling as evidenced in the far field is independent of the position in the mode field, in contrast to the spin-orbit coupling that leads to preferential emission directions for spin-polarized quantum dots [146]. The difference can be related to the fact that the emitters act as near-field point sources, which couple not only to the fundamental Bloch harmonic of the edge state field.

The excitation probability shows a strong position dependence across the edge. In comparison to the single-peaked exponential mode profile we observed in Fig. 4.8, here we see a rather complex mode profile. Peaks in excitation probability can be observed at positions labelled  $0\mu\text{m}$ ,  $4.5\mu\text{m}$  and  $6.25\mu\text{m}$ , with negligible excitation probability at positions in between. This complex excitation profile may be related to the fact that often several closely spaced ‘lines’ are observed in the microscope images of edge states, most pronouncedly in Figs. 5.2d and 5.3b. It could potentially be associated with a nontrivial angular distribution of the emission transverse to the propagation direction, which is a topic of future study.

### 5.3. Routing light around a topological junction

To demonstrate the routing of topological edge states at sharp corners, we fabricate a junction between an armchair and a zigzag edge that separates four distinct photonic crystal regions, as depicted in Fig. 5.4a.

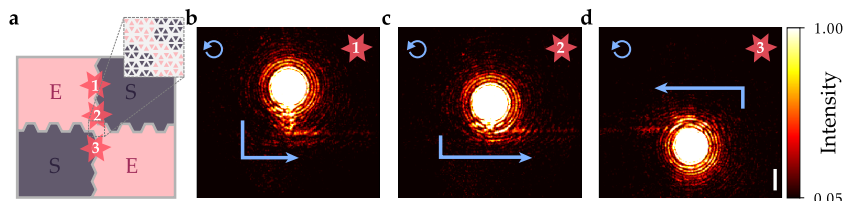


**Figure 5.4: Routing of light around a topologically protected chiral junction:** **a.** A schematic diagram showing a junction formed by four topological edges. The inset shows a zoomed-in image of the chiral junction. **b-d.** Real-space images showing light propagation when the sample is excited by a left-circularly polarized monochromatic laser at positions 1, 2 and 3, respectively, marked in **a**. All three images **b-d** are normalized to the maximum pixel value among the three. The scalebar corresponds to  $10\mu\text{m}$ .

The edges form a total of four topological waveguides emanating from the junction, of two different classes: For positive pseudospin, the two vertical edges support propagation towards the junction, whereas the horizontal edges allow propagation away from the junction. For negative pseudospin, the directions are reversed.

Figures 5.4b-d show images taken for various excitation points on the vertical edge marked in Fig. 5.4a. We can see in Fig. 5.4b that the positive pseudospin edge state excited with left CP at position 1 propagates downward towards the junction, but not further, as propagation in the bottom waveguide is forbidden for this pseudospin. Had the junction been perfectly symmetric, this pseudospin could have propagated in both the left and right horizontal waveguides. However, the light appears to propagate only into the right waveguide. This is even more clear when the state is excited at position 2, only a few micrometres away from the junction (Fig. 5.4c). The pronounced observed preference for taking a turn to the right waveguide must be related to the microscopic structural asymmetry of the junction, visible in the inset of Fig. 5.4a. The junction exhibits a chiral character, where we can recognize two continuous interfaces between the expanded and shrunken lattice unit cells that do not cross. Indeed, the light is efficiently routed along the interface that connects the top and right waveguides, even though it is separated from the other interface by sub-unit-cell distance — much smaller than the transverse extent of the modes. In a control experiment (Fig. 5.4d), we see that the same pseudospin excited in the bottom waveguide follows the other interface, into the left waveguide. Importantly, we also observe neither backreflection nor an enhancement of out-of-plane scattering at the junction. Together, these

observations suggest the important role of spin-momentum locking in the routing of the edge states, allowing them to take sharp corners and protect them from scattering to other modes.

## 5.4. Cavities formed by topological edges

### 5.4.1. Cavity modes in topological ring resonators

Optical cavities are components that can confine light for multiple oscillation periods. Ring resonators are a special class of optical cavities which trap light around the circumference of a structure. Well-known examples are whispering gallery mode (WGM) cavities, which confine light by the principle of total internal reflection [168, 184]. It is possible to form ring resonators in topological photonic crystals by making finite-sized ‘patches’ of expanded (shrunk) unit cells in a shrunken (expanded) lattice, where the outer edge of the patches constitutes a topological edge that can support topological edge states. Since the edge closes in the form of a ring, we can expect discrete cavity modes in these structures, possibly with characteristics relating to the topological nature of the crystals. There have been a theoretical discussion [185]<sup>1</sup> and a microwave experimental realization of such cavities [186] which evidence the existence of these topological states.

Here, we demonstrate two types of photonic topological cavities: One where finite-sized expanded lattice patches are formed inside a large shrunken lattice (which we call *ER* cavities) and vice versa (which we call *SR* cavities). In both cases, the topological edge around the finite-sized lattices forms a hexagonal ‘ring’. For each type, we fabricate four cavities that have different sizes, so that the effect of total round trip length on the cavity modes can be studied.

Figure 5.5 shows measured reflection of horizontally polarized light as a function of frequency and  $k_y$  for cavities having different circumferences. Shown above each of the dispersion plots are the designs of the corresponding cavities. As we have seen in Ch. 4, when expanded and shrunken lattices are brought together, the edge between them supports topologically protected states. In contrast to the edge modes having continuous dispersion throughout the bulk bandgap, here we see them to appear as resonant states with discrete frequencies and a distribution of wavevectors (emission angles), as evidenced by the horizontal lines within the bandgaps in Fig. 5.5. It must be noted that which mode we excite depends strongly on the excitation position of the focused incident beam. For each measurement, we choose it such that a maximum number of modes is observed in reflection. As we can see in Fig. 5.5a, replacing even a single unit cell of the shrunken lattice with an ex-

<sup>1</sup>In this work, the cavities were referred to as photonic topological ‘particles’, similar to the topological insulator particles in condensed matter physics, since they are formed by finite-sized crystals.

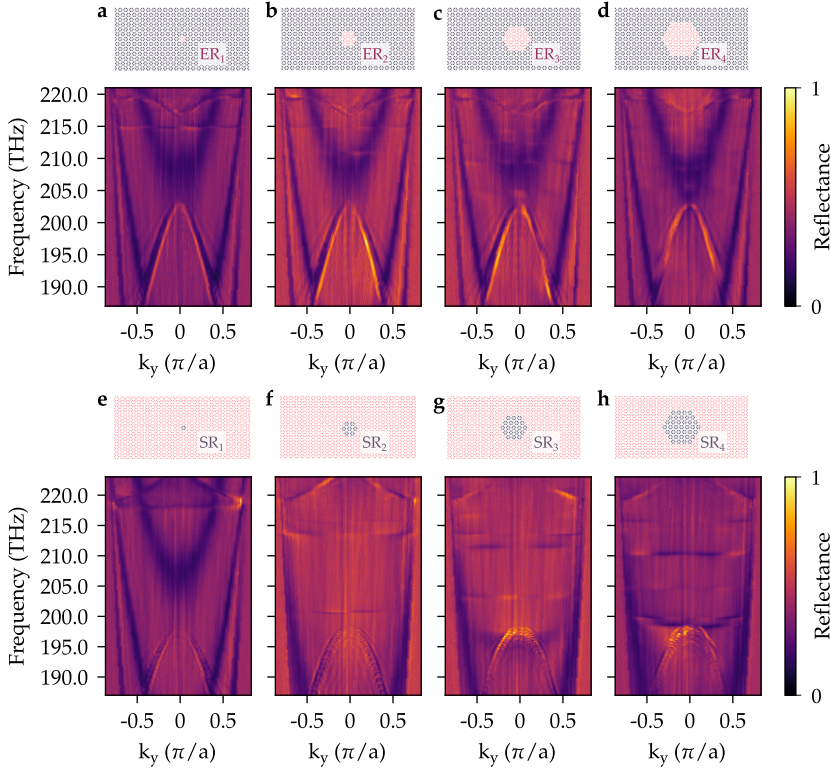


**Figure 5.5: Dispersion measurements on cavity modes: a-d (e-h).** Measured dispersion of cavities having different circumferences, formed by expanded (shrunk) unit cells in a shrunken (expanded) lattice, for horizontally polarized light incidence.

panded one creates a confined mode around 215 THz having  $Q \approx 616$ . Starting from a single unit cell in Fig. 5.5a (length around the cavity perimeter  $l_{ER_1} = 2.77 \mu\text{m}$ ), we go on increasing the circumference of the rings and as we can see in Figs. 5.5b ( $l_{ER_2} = 8.31 \mu\text{m}$ ), c ( $l_{ER_3} = 13.86 \mu\text{m}$ ) and d ( $l_{ER_4} = 19.40 \mu\text{m}$ ), the number of states within the bandgap increases. The results for the shrunken in expanded case follow the same trend, as shown in Figs. 5.5e-h.

After observing that the free-spectral range of the cavity modes reduces as the size increases, it would also be interesting to study the effect of cavity circumference on the optical losses of the modes. To illustrate the variation of the modes' quality factor as the cavity circumference changes, we choose a single mode near 215 THz that is common to all the cavities  $ER_{1-4}$  that we showed in Figs. 5.5a-d. For each of the cavities, we take seven crosscuts in the corresponding dispersion diagrams and fit a model to the normalized reflection to extract the resonance frequency and linewidth in each crosscut (see appendix 5.A.3). The mean extracted quality factors for each cavity are

plotted as red circles in Fig. 5.6. The blue error bars correspond to the standard error of the mean. If bending losses (scattering at corners) dominate, one may expect smaller quality factors for smaller cavities. Here, we observe that the quality factor of the cavity modes does not change significantly for different perimeter lengths of the cavities. This suggests that scattering due to the finite size (curvature) of the cavities is not the dominant loss mechanism for these cavities, even for the smallest sizes. As the experimental cavity linewidths are comparable to those of the edge state dispersion curves, it seems likely that intrinsic radiation dominates losses also in ring resonators. It would be interesting to investigate loss mechanisms in topological photonic crystal cavities with lower intrinsic radiation losses, such as those based on the valley Hall effect [147–149], in order to elucidate the role of topological protection in the reduction of scattering.

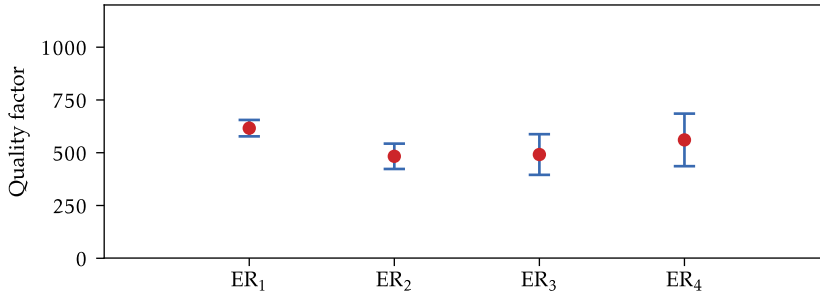


**Figure 5.6: Variation of quality factor of a cavity mode for different topological cavities:** Mean values obtained from six datasets are shown as red circles and the blue lines correspond to the standard error of the mean values.

A perfectly circular WGM resonator supports degenerate cavity modes that propagate in opposite directions. In conventional WGM resonators, these are called clockwise and counter-clockwise propagating modes. As we have seen in Ch. 4, for a given frequency within the bulk bandgap, the edge between shrunken and expanded lattices can always support two counter-propagating states having opposite pseudospin at  $\pm k$ , meaning that we expect doubly degenerate cavity modes here as well. Let us denote the modal amplitudes of the counter-propagating states in the ring as  $\tilde{a}_{\sigma+}$  and  $\tilde{a}_{\sigma-}$ . In a perfect ring, the eigenmodes  $\tilde{a}_{\pm} = \frac{1}{\sqrt{2}}(\tilde{a}_{\sigma+} \pm \tilde{a}_{\sigma-})$  that are even and odd superpositions of the counterpropagating fields have equal frequencies  $\omega_{\pm}$ . One can expect lifting of the degeneracy and splitting of degenerate modes in a WGM resonator when the ring is not perfectly circular or in presence of impurities [187–189]. This effect is usually interpreted as a coupling (scattering) between clockwise and counter-clockwise modes, with the splitting  $|\omega_{+} - \omega_{-}|$  equal to the backscattering rate. The splitting has to be larger than the intrinsic linewidth of the individual cavity mode in order



to see that in measurements. Thus, the investigation of mode splitting is especially interesting in the context of topological photonic resonators, where backscattering is potentially mitigated due to topological protection.

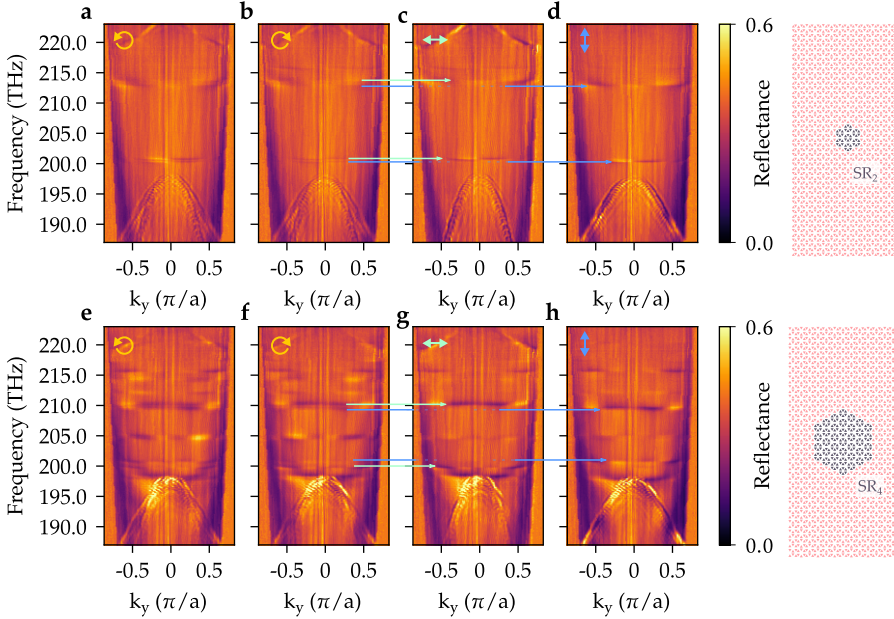


**Figure 5.7: Cavity mode splitting: a-d (e-h).** Mode splitting illustrated in an  $SR_2$  ( $SR_4$ ) cavity with dispersion measurements for incident light that is left-circularly, right-circularly, horizontally and vertically polarized, respectively. The green and the blue arrows depict mode doublets, which have predominantly vertical and horizontal polarization, respectively.

Figure 5.7 shows dispersion measurements on the cavities  $SR_2$  and  $SR_4$ , where we clearly see splitting for certain modes. The frequencies of these mode doublets are indicated by blue and green arrows. We have seen in Sec. 4.4 that the positive and negative pseudospins contribute to the far field as left and right circular polarizations, respectively. The odd and even superpositions,  $\tilde{a}_{\sigma-}$  and  $\tilde{a}_{\sigma+}$ , should thus exhibit vertically and horizontally polarized far fields. When the incident light is left- (Fig. 5.7a) or right-circularly polarized (Fig. 5.7b), pairs of closely situated modes around 199 THz and around 214 THz can be identified for  $SR_2$ . As expected, only one among each pair is excited for incident light of horizontal polarization (marked by the green arrow from Fig. 5.7b to c) and the opposite one gets excited for vertically polarized incidence (marked by the blue arrow from Fig. 5.7b to d). Similarly, also for  $SR_4$  we can identify two pairs of orthogonally-polarized split modes around 200 THz and 210 THz, as seen in Fig. 5.7e-h. We have seen in Sec. 4.5 that the topological states in our system



have an inherent spin-spin scattering due to the  $C_6$  symmetry breaking which induces a splitting in the edge state dispersion. The splitting caused by inherent  $C_6$  symmetry breaking and the splitting that we see here in some of the cavity modes are of the same order of magnitude ( $\lesssim 1$  THz). The fact that we do not observe larger splittings means that backscattering at the corners is likely not to be significant. Moreover, we note that in fact not all resonances exhibit observable mode splitting. These observations motivate more in-depth studies to explain the origin of splitting and the role of backscattering.

### 5.4.2. Comparison to a simple cavity model

A cavity resonance in ring resonators occurs when the phase acquired by light in one round trip equals an integer multiple of  $2\pi$ . If phase accrual along the ring can be described by an effective wavevector  $k_{\text{eff}}$ , the resonant condition reads:

$$k_{\text{eff}}L = m2\pi, \quad (5.1)$$

where  $L$  is the round trip length around the cavity, and  $m \in \mathbb{Z}$ .

For large, circular rings,  $k_{\text{eff}}$  can be approximated by the wavevector  $k$  of a straight waveguide. Knowledge of the waveguide dispersion relation  $\omega(k)$  then allows to predict the resonance frequencies  $\omega_m$  for each integer  $m$ . Even though we recognize that the considered cavities are far from large (i.e., the transverse extent of waveguide fields is larger than the cavity radius), we will compare our results to the predictions of such a “toy” model in the following. The dispersion of edge states can be approximated as a linear relation between  $\omega$  and  $k$ :

$$\omega = \omega_0 + v_g k, \quad (5.2)$$

where  $\omega_0$  is the angular frequency at which edge states cross each other (at  $k = 0$ ) and  $v_g$  is the group velocity of the states. The topological rings that we consider in this chapter are (mostly) constituted of zigzag edges between shrunken and expanded lattices. These states feature a measured group velocity  $v_g \sim c/6$  (found by fitting a linear dispersion to Fig. 4.6b) and crossing frequency  $\omega_0 \sim 1.31 \times 10^{15} \text{ rad/s}$ .

From Eqs. (5.1) and (5.2), the toy model predicts topological cavity frequencies:

$$\omega_m = \omega_0 + m \frac{2\pi v_g}{L}. \quad (5.3)$$

In Fig. 5.8, we show the cavity mode frequencies found by taking a crosscut in the measured dispersion in Fig. 5.5 along with the frequencies predicted by Eq. (5.3) for rings of different lengths  $L$ , as measured by the length of the edge when recognizing it as being composed of parts of straight edge waveguides. Blue and red markers correspond to measured and predicted

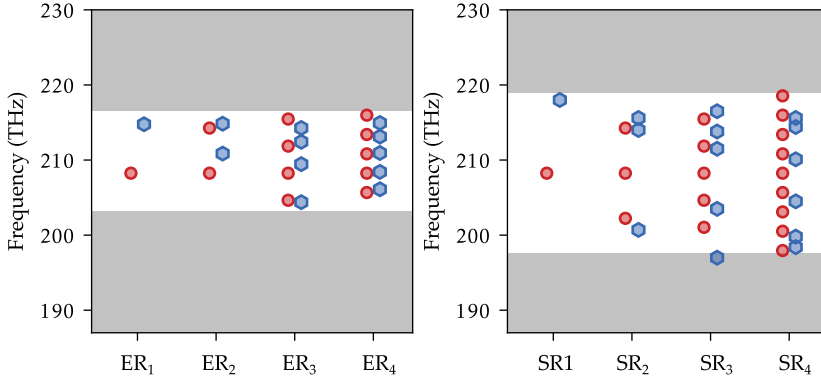


**Figure 5.8: Topological cavity modes for different cavities:** Predicted (red circles) and measured (blue hexagons) cavity modes in **a.**  $ER$  and **b.**  $SR$  cavities. The white region indicates the bulk bandgap.

5

values, respectively, and the grey-shaded region denotes the bulk frequencies. We can recognize from Fig. 5.8a that the number of modes predicted by our toy model within the bandgap of the surrounding crystal matches the measured number of modes within the bandgap for expanded cavities in shrunk lattice ( $ER_{1-4}$ ). This is true for the case of shrunk cavities in expanded lattice as well, except for the widest cavity ( $SR_4$ ) as seen in Fig. 5.8b. We note that it may be that not all modes are observed experimentally due to alignment. Thus, the model qualitatively predicts the number of modes and their approximate frequency spacing. However, the exact frequencies are not predicted well by the toy model. In particular, it predicts an  $m=0$  mode in the centre of the bandgap (where  $k=0$ ) for the  $ER_1$  and  $SR_1$  cavities, whereas the experiments reveal single modes near the upper band edge. Thus, the strong curvature of the ring is understood to alter the actual phase accrual with respect to that in the toy model. As such, a more advanced analysis is needed to fully understand the mode spectrum.

### 5.4.3. Effect of cavity shape on frequencies and losses

Compared to the conventional WGMs, topological counterparts have the advantage of being robust against sharp corners. This allows us to design topological WGM resonators having arbitrary shapes. To test the topological robustness of the cavities, we fabricate a cavity having the same length as one of the cavities we considered earlier ( $ER_3$ ) but a much less-close-to-circular shape ( $EX_3$ ), and compare their dispersion.

The shape of the fabricated cavity is that of a distorted diamond and is significantly different from  $ER_3$ . Figure 5.9 shows a comparison of their dispersion measurements. The measured dispersion for the cavities are shown in Fig. 5.9a and d. By taking a crosscut in the dispersion diagram, we extract the

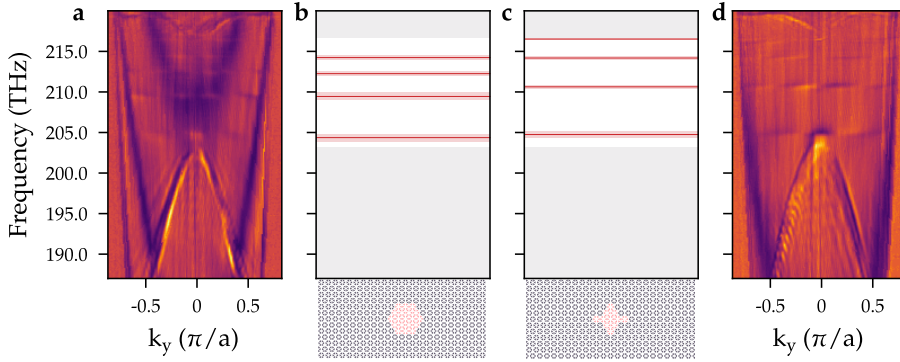


**Figure 5.9: Comparison of cavities having different shapes:** **a, d.** Dispersion measurements on cavities  $ER_3$  and  $EX_3$ , having same circumference but different shapes. **b, c.** Shape (bottom row) and the extracted cavity modes (red solid lines) of the respective cavities. Cavity mode linewidths are shown as red shaded regions. The white region corresponds to the bulk bandgap.

frequencies and linewidths of both cavity modes and show them as red lines and shaded regions, respectively, in Fig. 5.9b and c. The number of modes remains the same for the two cavities. However, there is an overall increase in the free-spectral range. The quality factor of the modes of diamond-shaped cavity are slightly higher compared to  $ER_3$ , but of the same order of magnitude. The existence of the same number of modes with similar features in both cavities evidences their topological origin and robustness.

## 5.5. Topological coupling of confined light

Coupling of light into/out of cavities from/to waveguides (add-drop functionality) is a desirable feature in integrated optics. Here, we look at the coupling of light in an optical system formed by topological edges. We observe that the topological system of cavity and waveguide coupler features an important distinction compared to traditional ring-waveguide couplers. In the conventional WGM couplers, the mechanism behind the coupling of light from the cavity to the waveguide or vice versa is momentum conservation within the finite coupling region where waveguide and cavity boundary run parallel.

We consider a whispering gallery mode resonator system with two waveguides on each side as shown in Fig. 5.10a and b. The resonator supports degenerate clockwise and counter-clockwise propagating modes. As illustrated in Fig. 5.10a, the clockwise propagating mode inside the cavity can only couple to the rightward propagating mode in the top waveguide and leftward propagating mode in the bottom waveguide. It cannot couple to a leftward (rightward) propagating wave in the top (bottom) waveguide due

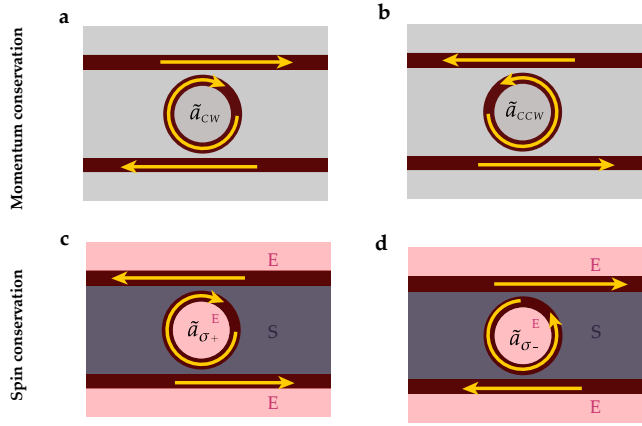


**Figure 5.10:** Difference between cavity-waveguide couplers operating with momentum (a,b) and spin (c,d) conservation. See the text for details.

5

to momentum mismatch. However, as we see in Fig. 5.10b, the momentum of the counter-clockwise mode matches the leftward (rightward) propagating wave in the top (bottom) waveguide and can couple to it.

For the topological cavity-waveguide coupler systems that we consider, the coupling is governed by spin conservation, as we will see below. Figures 5.10c and d illustrate the mechanism of coupling in our system. The topological edge forming the cavity ring as well as the waveguides support counter-propagating positive pseudospin ( $\sigma_+$ ) and negative pseudospin ( $\sigma_-$ ) modes. As we have seen earlier in Sec. 4.4, there exists a spin-to-direction coupling for a given edge. Thus  $\sigma_+$  is always associated with modes propagating:

- (i) clockwise along the edge of an expanded cavity in shrunken lattice,
- (ii) leftward in an expanded (top) -shrunken (bottom) interface, and
- (iii) rightward in a shrunken (top) -expanded (bottom) interface.

This causes a clockwise-propagating mode inside the cavity to couple to leftward-propagating waves in the top waveguide and to rightward-propagating waves in the bottom waveguide, in contrast to the conventional couplers, as illustrated in Fig. 5.10c. Similarly, the counter-clockwise propagating  $\sigma_-$  mode couples to the rightward- (leftward-) propagating mode in the top (bottom) waveguide (Fig. 5.10d). We experimentally verify this by selective excitation of the counter-propagating cavity modes using right- or left-circularly polarized light incidence in a system of topological waveguide couplers. As we will show later, the cavity has degenerate modes such that a specific handedness can be excited with circular polarization.

Figure 5.11b shows a schematic of the system that we fabricated. A zoomed-in version of the cavity-waveguide coupler is shown in the inset. Two armchair edges are created on two sides of an  $ER_4$  cavity. Edges between

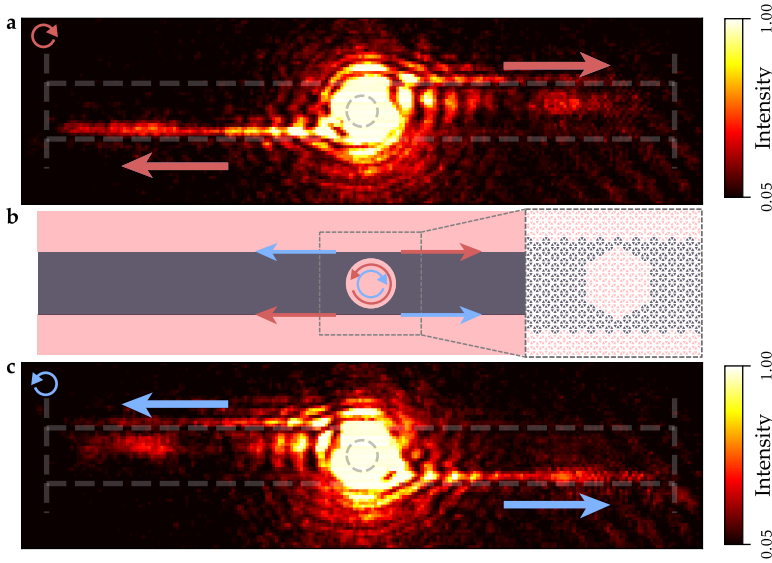


**Figure 5.11: Coupling light from the cavity to the waveguide:** **a, c.** Real-space images, taken when a right- or left-circularly polarized laser at 1470 nm is focused onto the cavity. Depending on the input polarization, light chooses two out of the four possible paths. **b.** A schematic of the experimental scheme (inset: the actual geometry at the coupling sites). The distance between the waveguides is  $\sim 7.2 \mu\text{m}$ .

shrunk and expanded lattices and the physical extent of the structure are designated by dashed lines in Fig. 5.11a and c. We excite the cavity with a focused beam of right circularly polarized light at 1470 nm and image light propagation in real space using the experimental setup laid out in Fig. 5.1. As we see in Fig. 5.11a, light from the cavity gets coupled to the right-propagating mode in the upper waveguide and the left-propagating mode in the lower waveguide. Now, if we change the incidence to left circularly polarized light, light from the cavity gets coupled to the left-propagating mode in the upper waveguide and the right-propagating mode in the lower waveguide (Fig. 5.11c). As right (left) circularly polarized light excites waves that travel counter-clockwise (clockwise) in the ring, these observations confirm that spin is conserved in coupling from cavity to waveguide. We note that, irrespective of the input polarization, there is always some leakage into the bulk shrunk region when light is coupled to the upper waveguide, contrary to the case when it gets coupled to the lower waveguide, where it propagates well-confined. The reason for this difference is not understood, although it could be related to the fact that the top and bottom coupling region differ microscopically (see Fig. 5.11b).

Next, keeping the incident polarization right-circular, we move the excitation spot away from the cavity to eight different positions around it and image

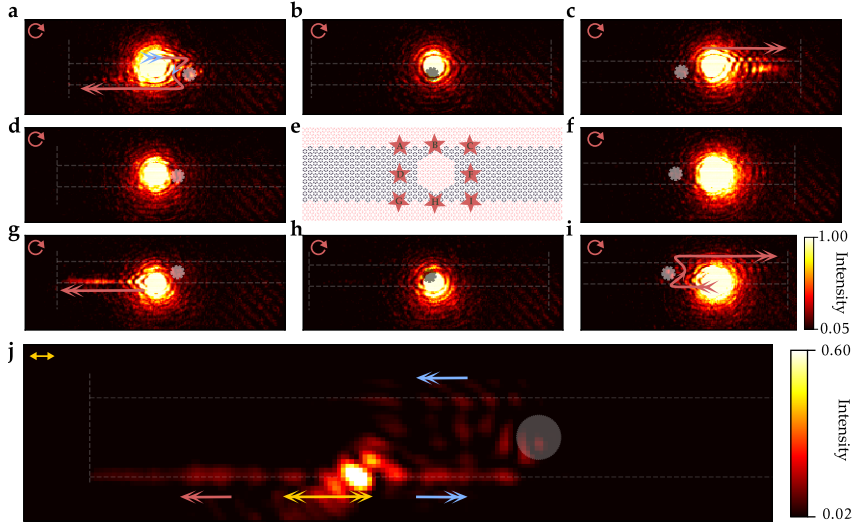


**Figure 5.12: Influence of excitation position on coupling:** a-d, f-i. Real-space images, taken when left-circularly polarized light at 1470nm is incident onto different locations, as marked in e. j. In- and out-coupling of light between waveguides and cavity, for linearly polarized light incident at position G. A cross-polarized linear polarizer is placed in the reflected path for this particular measurement. The distance between the waveguides is  $\sim 7.2\mu\text{m}$ .

the reflected light in real space. A schematic of the excitation positions relative to the cavity is shown in Fig. 5.12e. To record the exact excitation positions, a separate white-light image of the system was taken for each measurement. The cavity edge, the two waveguides and the boundaries of the photonic crystal that can be recognized from the white light images are overlaid as dashed lines in Fig. 5.12a-d, f-i.

Excitation at positions C and G is equivalent to excitation of standalone waveguides. This simply causes the  $\sigma_-$  edge mode in the respective waveguides to travel away from the cavity. However, if we excite the system at position A, we can observe coupling of light from the entry waveguide to the cavity and from there to the exit waveguide. It can be seen in Fig. 5.12a that the  $\sigma_-$  edge mode is excited, travels rightward in the upper edge till the coupling point, is coupled into the cavity, and travels leftward in the lower edge after coupling out of the cavity. A similar behaviour in the opposite direction can be observed when we excite at position I (Fig. 5.12i). As a control experiment to see the out-coupling more clearly, we excite the structure again at position G with linearly polarized light and image the propagation after placing a cross-polarized linear polarizer in the reflected path. The cross-polarizer suppresses direct scattering. The recorded image is shown in Fig. 5.12j. When excited with linearly polarized light, both  $\sigma_+$  and  $\sigma_-$  modes are excited in the

lower waveguide. While the  $\sigma_-$  mode travels leftward, the  $\sigma_+$  mode travels rightward but does not proceed past the cavity. Instead, it is coupled out of the cavity into the upper waveguide and travels leftward from there.

We see no coupling of light into either waveguide when the incident light is focused at positions *D* or *F* (Fig. 5.12d and f). This suggests that it is not possible to simultaneously excite the upper and lower edges by choosing an excitation position equidistant from these two edges. This confirms that the results we see in Fig. 5.11 are indeed the coupling from cavity to waveguide. We also excite at two positions *B* and *H* that are on the waveguide in the middle of the coupling region. Surprisingly, we see neither propagation nor coupling into the cavity at these excitation points (Fig. 5.12b and h, respectively). The observation indicates the presence of a node in the cavity mode field at these points. Further explorations like a systematic study on the spatial dependence of cavity modes in the presence of nearby waveguides for structures with different coupling geometries might be needed for a conclusive remark on this observation.

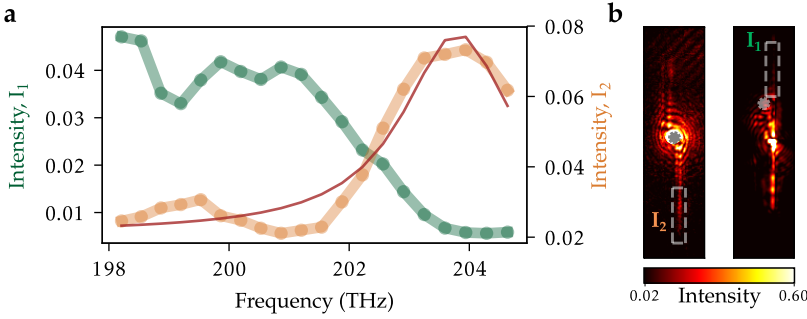


**Figure 5.13: Frequency dependence of light coupling between cavity and waveguide:** **a.** Green markers indicate transmission in the input waveguide, measured as integrated intensity over an area indicated in the right panel of **b**, as a function of frequency. Orange markers indicate the outcoupling from cavity to waveguide, measured as the integrated intensity over an area of pixels as indicated in the left panel of **b**, as a function of frequency. Green and orange lines are guides to the eye. A simple Lorentzian with a constant offset fitted to the data is shown as brown solid line. **b.** Area over which light intensity is integrated for the two cases, marked as dashed rectangles.

We also note that, whenever light couples to the cavity, we see that almost all the light from the waveguide gets coupled, observing an absence of propagation past the in-coupling point (Figs. 5.12a, i and j). This suggests that the cavity is coupled to the two waveguides with rates that exceed the intrinsic cavity decay, i.e., that it is strongly ‘overcoupled’. If this is the case, the cavity linewidth should be significantly larger than the intrinsic linewidth observed before. To get an approximate measure of the total cavity linewidth, we perform a wavelength sweep to see the dependence of coupling on frequency of incident light. We repeat the measurement shown in Fig. 5.12j



for different laser frequencies. To record the transmission of light past the cavity, we integrate the imaged intensity past the coupling point in the area indicated in Fig. 5.13b. The green markers in Fig. 5.13a show the transmission in the input waveguide as a function of incident frequency. The transmission drops to minimum when the input light is fully coupled to the cavity, in agreement with the hypothesis that the cavity is overcoupled. We also record the coupling to the other waveguide as a function of laser frequency (repeating the measurement shown in Fig. 5.12a). The integrated intensity of out-coupled light in an area indicated in the left panel of Fig. 5.13b is plotted as orange markers in Fig. 5.13a. Both maximum out-coupling and minimum transmission (maximum in-coupling) occur around 204 THz. Fitting a simple Lorentzian with a constant offset (solid brown line in the figure), we find that the cavity quality factor is not larger than 91. Comparing this value to the intrinsic  $Q \sim 400$  of the edge modes shows that the cavity losses are indeed dominated by coupling to the waveguides. This broad linewidth also explains why the cavity supports degenerate modes (i.e., splitting is smaller than linewidth), and why we were not able to distinguish the cavity modes in far-field spectroscopy.

## 5.6. Near-field study of topological photonic crystals

### 5.6.1. Scanning near-field optical microscopy

While the study of the far field of topological photonic crystals provides a wide range of information about their properties, their fields are necessarily structured at scales significantly smaller than the wavelength. It is therefore of interest to gain access to the evanescently decaying near fields within the first tens or hundreds of nanometres from the photonic crystal surface. These fields often contain important information about the behaviour of light in nanostructures, and can pave the way to potential applications. Due to its evanescent nature, the near field is typically not accessible using common imaging techniques. Scanning near-field optical microscopy (SNOM) offers direct access to these sub-wavelength features [190]. This includes nanoscale mapping of electric and magnetic fields at the surface of the structure [191], imaging higher order Bloch harmonics that otherwise carry zero weight on the far-field-detectable fundamental Bloch harmonic [192], and quantifying polarization of light at the nanoscale [193]. In this section, we present first results on the near-field imaging of the topological photonic crystals that we developed. We demonstrate the potential to image and analyse the near field of photonic topological edge states, and study their Fourier spectrum and dispersion through phase- and polarization-resolved near-field microscopy. This provides the potential for future studies of the full structure of topological light fields at the nanoscale.

The SNOM technique we employ consists of scanning a nanoscale aperture



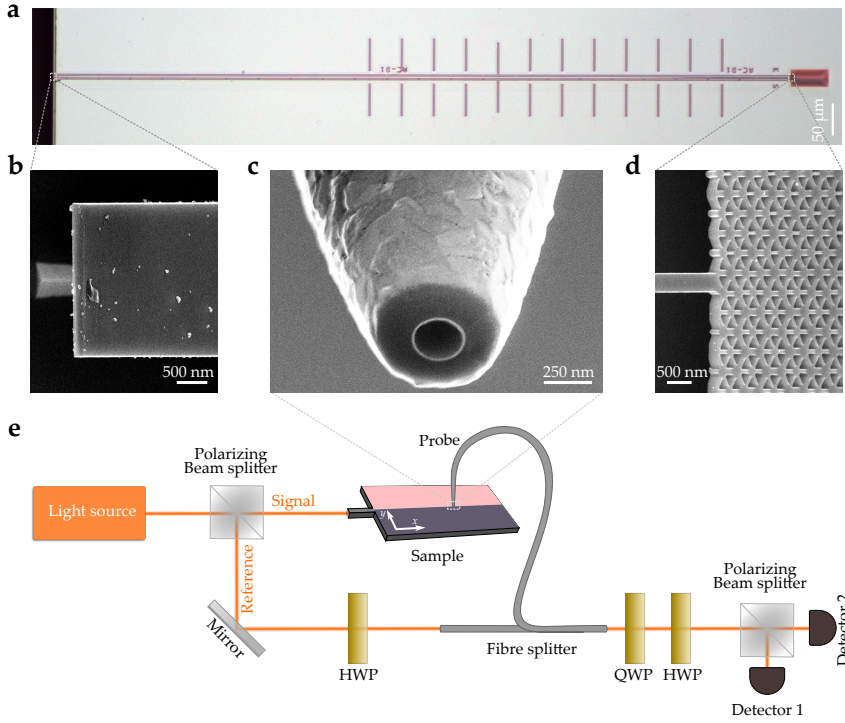


**Figure 5.14: Sample and experimental setup:** **a.** An optical microscope image of the sample fabricated on a silicon-on-insulator chip. A  $\sim 1.15\text{ mm}$  long waveguide carries light from free-space to the photonic crystal with a topological edge. The free-standing waveguide is supported by  $100\text{ nm}$  wide tethers on each side (see appendix 5.A.1). **b, d.** Scanning electron microscope (SEM) images of the entrance facet and incoupling point, respectively. **c.** A SEM image of the aperture of the near-field probe used, having an aperture diameter of  $\sim 259\text{ nm}$ . **d.** A simplified schematic diagram of the scanning near-field optical microscope setup. Light sensed by the scanning near-field probe interferes with a reference signal at the output, providing heterodyne detection of the evanescent fields above the sample surface. One quarter wave plate and two half-wave plates provide a polarization-resolved detection in two quadrature detectors.

probe over the photonic crystal surface, while collecting the evanescent optical fields through the probe. The probe itself is a pulled optical fibre, coated with aluminum [190]. The tip of the fibre is removed to produce an aperture with a diameter of the order of  $100\text{ nm}$  (Fig. 5.14c shows a scanning electron microscope image of such an aperture). A shear-force feedback mechanism keeps the scanning probe at a fixed height ( $\sim 20\text{ nm}$ ) from the surface [194]. Figure 5.14e shows a simplified schematic diagram of the SNOM experimental setup. The setup employs a heterodyne detection scheme that allows phase-sensitive detection. The input light is split into a reference arm and a signal arm. A pair of acousto-optic modulators (not shown in the figure) shifts

the frequency of light in the reference arm. The frequency-shifted light in the reference arm later interferes with the signal collected by the near-field probe, producing a beating. This is subsequently detected using lock-in amplifiers, which give access to both quadratures of the light field [195]. Moreover, the polarization optics employed in the reference and output arms provide a polarization-resolved detection [193] of two orthogonal polarizations simultaneously [191], with which in principle a full vectorial mapping of the detected field can be achieved [196]. The near-field signal is measured over two calibrated detectors such that each separately collects one of the two orthogonal polarizations along the  $x$  and  $y$  Cartesian coordinates of the field at the surface, so that the in-plane electric field vector can be given by:

$$E_{\parallel} = \hat{x} E_x + \hat{y} E_y, \quad (5.4)$$

where  $E_x = E_{x_1} + iE_{x_2}$  and  $E_y = E_{y_1} + iE_{y_2}$  are the complex electric fields<sup>2</sup> detected by the two detectors. The polarization optics have to be properly calibrated in order to provide a one-to-one mapping of the  $x$ - and  $y$ -polarizations of the field in the sample plane to the polarizations  $E_x$  and  $E_y$  in the detectors. The calibration can be performed by imaging fields above a waveguide with known field distributions. We use the free-standing single-mode entrance waveguide of the fabricated photonic crystal for this purpose.

Figure 5.14a shows optical and scanning electron microscope images of the fabricated sample in top view. The sample consists of a topological photonic crystal similar to the ones that we have seen in Ch. 4 and an attached tapered waveguide to couple light into the topological waveguide in the photonic crystal. We fabricate the sample on a silicon-on-insulator chip following the same procedures as described in appendix 4.A.2. However, to have a cleaved waveguide facet for incoupling light to the photonic crystal from the side, we follow an extra step after reactive-ion etching, before the wet etching: The sample is cleaved using a diamond pen by placing it between two glass slides [198]. As seen in Fig. 5.14b, the facet is not perfectly cleaved; however, this does not affect our incoupling significantly.

### 5.6.2. Near-field imaging of edge state propagation

To excite the waveguide modes, collimated light from a continuous-wave infrared laser is focused onto the entrance facet using an objective lens. Light propagates through the entrance waveguide to the incoupling point (Fig. 5.14d shows a scanning electron microscope image of the incoupling point). During focusing of light onto the entrance waveguide, light can unnecessarily get coupled into the bulk silicon and affect collection of

<sup>2</sup>Even though the detected signal by the probe can contain both electric and magnetic fields, as the probe is sensitive to both [191], distinguishing them is not relevant for our current analysis, and the detected signal in our system can always be expressed as an equivalent electric field [197].

photonic crystal modes using the probe. To minimize the amount of bulk-coupled light reaching the photonic crystal, we fabricate a series of rectangular trenches on either sides of the entrance waveguide (see Fig. 5.14a). Light travelling through the entrance waveguide finally reaches the incoupling point and gets coupled into the topological waveguide, if its frequency lies within the bandgap of the topological photonic crystals.

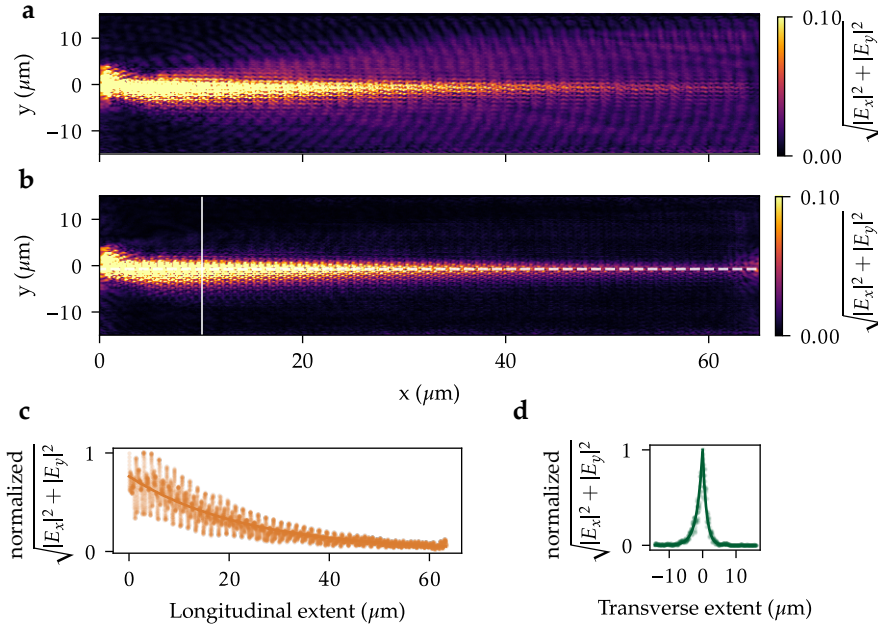


**Figure 5.15: Near-field map of a photonic crystal with an armchair edge:** **a.** The measured amplitude  $(|E_x|^2 + |E_y|^2)^{1/2}$  of the in-plane electric field at a few nanometres above the surface of the photonic crystal, excited by a continuous-wave laser at 1560 nm. Light is guided in the armchair edge right to the incoupling point ( $x \sim 1.5 \mu\text{m}$  and  $y \sim 0 \mu\text{m}$ ). **b.** The field-map after Fourier-filtering the stray light picked up by the probe (as described in Sec. 5.6.3). **c.** Normalized amplitude (orange markers) along a longitudinal cross-cut, indicated by the white horizontal dashed line in **b**. The solid orange line corresponds to an exponential decay fit to the data. **d.** Normalized integrated amplitude from a transverse area indicated by the vertical white line in **b**.

After exciting the sample with light at 1560 nm, we raster-scan the near-field probe over a  $66 \mu\text{m} \times 30 \mu\text{m}$  area at a height of  $\sim 20 \text{ nm}$  above the surface around the topological edge. Figure 5.15a shows the amplitude of the total measured field  $|E_{\parallel}| = (|E_x|^2 + |E_y|^2)^{1/2}$  from this area. The incoupled light excites one of the edge states which travels along the armchair waveguide. We notice that the probe also picks up some free-space light which interferes with the evanescent light from the guided mode (parabolic interference patterns in the figure). It is possible to filter out this contribution up to a certain extent in Fourier space, as we will see in Sec. 5.6.3. Figure 5.15b shows the filtered

data. We can clearly see the propagation of the confined mode along the edge. Plotted in Fig. 5.15c is a longitudinal crosscut taken in Fig. 5.15b (indicated by the white dashed horizontal line at  $y = 0$ ). We fit a single exponential function to this data to extract the decay length of the mode. The obtained  $1/e$  amplitude decay length  $L$  of  $\sim 23.41 \mu\text{m}$  corresponds to a quality factor  $Q = \omega L / 2 v_g \approx 283$ , assuming a group velocity  $v_g \approx c/6$ . We also take a crosscut in the transverse direction (over an area indicated by the white solid vertical line in Fig. 5.15b), and fit two exponentials to each side of the edge as shown in Fig. 5.15d. Compared to its decay in the expanded region (decay length  $\sim 1.1 \mu\text{m}$ ), the mode decays more slowly into the shrunken region (decay length  $\sim 1.7 \mu\text{m}$ ), following the trend that we observed earlier in Fig. 4.8.

### 5.6.3. Visualizing higher-order Bloch harmonics of edge states

The underlying Bloch components of the propagating state can be observed if we analyse the near-field of edge modes in Fourier space. Here we examine the measured field in reciprocal space by taking a two-dimensional Fourier transform of the measured field components such that the intensity of the field in reciprocal space can be represented by

$$I(k_x, k_y) = (|\mathcal{F}(E_x(x, y))|^2 + |\mathcal{F}(E_y(x, y))|^2), \quad (5.5)$$

where  $\mathcal{F}$  is the discrete two-dimensional spatial Fourier transform.

Figure 5.16 shows the obtained Fourier images corresponding to real-space measurements of edge state propagation in an armchair edge and a zigzag edge. In Fig. 5.16a, we show the Fourier transform of the measured field above an armchair edge. We observe peaks at specific wavevectors that follow the triangular reciprocal lattice of the underlying crystal. The white dashed circle around the  $\Gamma$  point marks the light cone in air. The centre peak that lies within the light cone corresponds to the fundamental Bloch harmonic. We also notice that all peaks are more narrow in the  $k_x$  than in the  $k_y$  direction. This is related to the transverse confinement of the edge mode that we observe in Fig. 5.15a. The Fourier-transform of the electric field distribution on a zigzag edge at the same frequency is shown in Fig. 5.16c. We recognize the  $90^\circ$  rotation between the reciprocal lattice of the photonic crystals with zigzag and armchair edges.

Examining the figures closely, we observe a partly circular feature at the wavevector  $k_x \sim 2\pi/1.38 \mu\text{m}^{-1}$ , as well as faint copies displaced by the reciprocal lattice vector in Fig. 5.16c. These components of the image are not fully understood, but could potentially be due to stray light that partly feels the index of the silicon slab and is picked up by the probe. As we believe these fields are not related to the topological edge state, we filter out such components by removing Fourier components within an area defined by a ring having a radius of  $\sim 2\pi/1.38 \mu\text{m}^{-1}$  and a  $\sim 0.2\pi/1.38 \mu\text{m}^{-1}$  wide Gaussian profile on its perimeter. The advantage of such an operation is that, by taking the inverse Fourier transform of the filtered images, the quality of field maps can

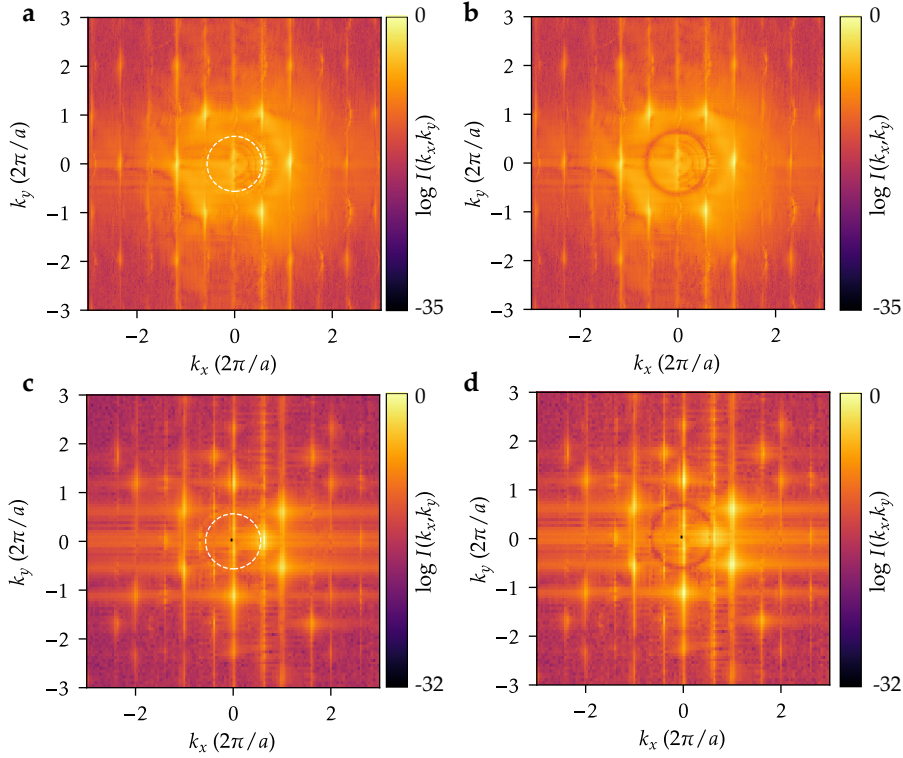


**Figure 5.16: Fourier filtering amplitude measurements:** **a.** A two-dimensional Fourier transform of the measured electric field amplitudes (calculated by Eq. (5.5)) on an armchair edge, in logarithmic scale. The reciprocal lattice vectors  $k_x$  and  $k_y$  are shown in units of  $2\pi/a$ , where  $a$  is the lattice constant of the bulk lattice. The white dashed circle corresponds to the light cone in air. In addition to the peaks corresponding to the underlying triangular lattice, circular features are seen close to the light cone, indicating some stray light picked up by the probe. **b.** A Fourier filter (a ring of radius  $a/1.38$  around the  $\Gamma$  point with a Gaussian profile of width  $\sim a/13.8$ ), defined to isolate this extra light. **c, d.** Similar unfiltered and filtered Fourier intensities corresponding to electric field measurements on a zigzag edge, respectively. The peaks are rotated by  $90^\circ$  with respect to the peaks in the Fourier map for an armchair measurement due to the  $90^\circ$  rotation between the armchair and the zigzag reciprocal lattices.

be considerably improved, isolating the edge state of interest. Figures 5.16b and d correspond to filtered Fourier space intensities in armchair and zigzag edges, respectively. Figure 5.15b shows the amplitude of the electric field distribution above an armchair edge after applying a Fourier filter as described in Fig. 5.16b and performing the inverse Fourier transform.

Next, by scanning the frequency of the incident laser for armchair and zigzag samples and stacking the Fourier-filtered one-dimensional Fourier

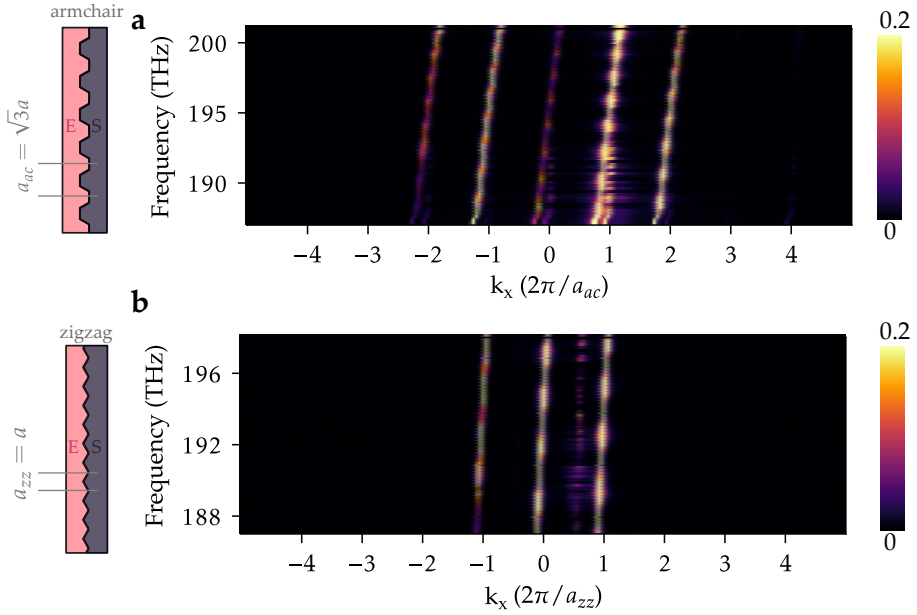


**Figure 5.17: Bloch harmonics of modes in armchair and zigzag edges:** **a.** Dispersion of armchair edge states along the  $x$  direction, computed from Fourier-filtered field measurements. Different Bloch harmonics are separated in the reciprocal space by  $2\pi/a_{ac}$ , where  $a_{ac}$  is the periodicity of an armchair edge, as indicated in the side panel. **b.** Dispersion of edge states calculated from Fourier-filtered amplitudes of the measured field above a zigzag edge. The Bloch harmonics of the zigzag edge state are separated by  $2\pi/a_{zz}$ . The periodicity of a zigzag edge is the same as the periodicity of the bulk lattice,  $a$ . Faint Bloch harmonics at  $k_x = 2\pi/a_{ac}$  in **a** and at  $k_x = \pi/a_{zz}$  in **b** correspond to stray light that was not filtered out.

transform (along  $x$ ) of the measured fields for each frequency, we construct dispersion diagrams for the armchair and zigzag edge states. Figures 5.17a and b show the constructed dispersion diagrams for an armchair and a zigzag edge, respectively. Sketches of the corresponding edges are shown in the left panels. As can be identified from the sketch, the periodicity of an armchair edge formed between shrunken and expanded lattices with a periodicity  $a$  is  $a_{ac} = a\sqrt{3}$  while the periodicity of a zigzag edge  $a_{zz}$  is the same as the bulk lattice periodicity  $a_{zz} = a$ . This explains the different separation of Bloch harmonics for the two types of edges. This difference can be understood also from the  $90^\circ$  rotation that we observed in Fig. 5.16. In Fig. 5.17a we observe only forward propagating Bloch components (with a group velocity of  $\sim c/6$ ) at an armchair edge. We also notice that the fundamental Bloch harmonic (at  $k_x = 0$ ) is weak as compared to the second (at  $k_x = \pm 2\pi/a_{ac}$ ) and third (at  $k_x = \pm 2 \times 2\pi/a_{ac}$ ) harmonics. This explains that while the states radiate to the far field, they still exhibit considerable optical quality factors. Also



for the zigzag edge, we mainly observe the Bloch components with positive group velocity (Fig. 5.17b). While the fundamental harmonic at  $k_x = 0$  is now stronger, comparison to Fig. 5.16c shows that this is mainly due to nonradiating components with large  $k_y$ . We also note that our filtering is not ideal, as we can see a faint harmonic of stray light at  $k_x a_{zz}/2\pi \approx 0.5$ . Still, the fact that we can identify each of these harmonics separately makes the technique a powerful tool to analyse the edge state properties. For example, comparing Figs. 5.16 and 5.17, we realize that some of the components have a transverse dependence that is nontrivial, as they are dominated by their non-zero contributions along  $k_y$ . Notably, we do not observe backreflected edge states with opposite phase and group velocity. This indicates that backscattering, e.g. at the end of the  $60\ \mu\text{m}$  long waveguide, is negligible. Further studies of edges and defects at the nanoscale could shed new light on the degree of topological protection in these systems.

In the far-field measurements that we had seen earlier in other sections of this chapter and Ch. 4, we only had access to a small region in the reciprocal space (marked by the white circle in Fig. 5.16). The fact that now we can access a large number of Bloch harmonics that lie out of the light cone widens the horizon of our understanding of these states. For example, it will be interesting to analyse and compare the polarization of each Bloch harmonic in a similar fashion to our analysis of the fundamental harmonic in the far field. Our access to the vector components of these fields at subwavelength scales opens a new range of opportunities to study topological states of light.

## 5.7. Conclusions and outlook

In this chapter, we demonstrated the capabilities of real-space imaging in characterization of a variety of topological systems. Using circularly polarized light, we selectively excited edge states and tracked their propagation in topological waveguides, routers and cavity-waveguide systems. The existence of degenerate as well as split discrete states in cavities formed by topological edges of different sizes and shapes was experimentally observed. We realized a cavity-waveguide coupling system and demonstrated the add-drop functionality operated by the principle of spin-conservation. Our results show that the magnitude of scattering loss and splitting in topological cavities as small as single unit cell defects are small compared to the intrinsic loss and backscattering in the straight topological waveguides. Further studies to elucidate the strength of topological protection in practical systems will be valuable. In the last section, we saw how the measurements in the near-field of the topological states can bring about new directions of investigations on them. Using a phase- and polarization-sensitive scanning near-field optical microscope, we observed the higher Bloch harmonics of topological edge states, which were not accessible using the far-field measurement techniques. Further analyses of the sub-wavelength-scale vectorial maps that we can obtain could uncover

valuable information on the nature, origin and properties of the topological edge states. It could shed light on the helicity of light fields at the nanoscale, the polarization of each of the Bloch harmonics, and the local flow of optical energy. Such studies are particularly important to judge the use of these states for selectively coupling to spin-polarized quantum emitters [105, 146, 199].

The excellent selectivity in excitation and the robustness of topological edge states make them promising candidates for manipulating light on a chip. A fresh line of research is evolving rapidly in the field of integrated photonics with incorporation of topological characteristics to the existing photonic devices including, not limited to, lasers, couplers, isolators and circulators [140, 200]. The fact that we can visualize the propagation, routing and coupling of topological edge states at the nanoscale at telecommunication wavelengths will strengthen these advancements. New studies should prove the applicability of such states in functional devices, and the ability to use them to control light-matter interaction in new ways.



## APPENDICES

### 5.A. Experimental methods

#### 5.A.1. Sample design and fabrication

##### Samples for far-field measurements

For the measurements presented in sections 5.2-5.5, we used the same design parameters given in appendix 4.A.1 of Ch. 4 for the shrunken and expanded lattices. The samples were fabricated using the protocol outlined in appendix 4.A.2 of Ch. 4.

The sample used for the experiment in Sec. 5.2 had an armchair edge of  $\sim 380\mu\text{m}$  length which separates shrunken and expanded lattices, having widths of  $\sim 196\mu\text{m}$  each. The sample used for the experiment in Sec. 5.3 contained two armchair-like edges of  $\sim 55\mu\text{m}$  and two zigzag-like edges of  $\sim 80\mu\text{m}$ , forming a four-way junction separating two sets of expanded and shrunken lattices. Samples used in Sec. 5.4 contain patches of expanded or shrunken unit cells which form single cavities of circumference varying from  $\sim 6$  to  $20\mu\text{m}$ , centred in the shrunken or expanded lattices having dimensions  $\sim 80\times 80\mu\text{m}$  each. The cavity-waveguide coupler system discussed in Sec. 5.5 is fabricated as a photonic crystal consisting of a rectangular shrunken lattice of  $\sim 8\times 80\mu\text{m}$  area, replacing expanded unit cells of the same area in the centre of an expanded lattice having dimensions  $\sim 80\times 80\mu\text{m}$ , thus essentially forming two armchair edges. Placed exactly in the centre of the shrunken lattice is a cavity of diameter  $\sim 5.6\mu\text{m}$ , formed by expanded unit cells. The exact design is shown in Fig. 5.12e.

##### Samples for near-field measurements

The samples used for the near-field measurements presented in Sec. 5.6 were fabricated on silicon-on-insulator chips. Figure 5.A.1 shows the design of the photonic crystals employed in experiments in top view. The light grey areas correspond to the top-layer silicon and the dark grey areas correspond to the etched regions. To perform near-field measurements on the sample, light has to be coupled in from the side of the photonic crystal slab. A  $1.15\text{mm}$  long waveguide was fabricated next to the photonic crystal for this purpose. At the entrance facet, the waveguide had a width of  $2.5\mu\text{m}$ . It was adiabatically tapered to a  $0.41\mu\text{m}$  single-mode waveguide over a tapering length of  $200\mu\text{m}$ . This single-mode waveguide of  $\sim 50\mu\text{m}$  length is attached to the incoupling point of the silicon photonic crystal. Since the waveguide cannot be left free-hanging over the total distance of  $1.25\text{mm}$ , a few tether structures of  $\sim 100\text{nm}$  width were fabricated, supporting the waveguide from either side. A series of rectangular trenches fabricated on either side of the waveguide scatter any light that gets coupled to the bulk silicon slab. Two photonic crystals were used in the experiment: One with an armchair edge and one with a zigzag edge. The photonic crystals used in the experiment were of dimensions

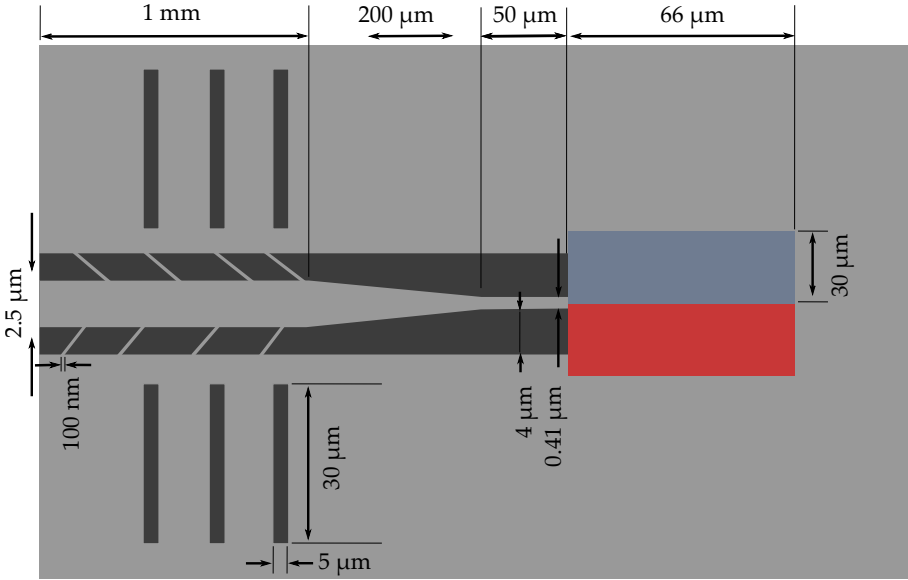


**Figure 5.A.1: Design of the samples used for near-field measurements:** The light grey area corresponds to the top silicon layer and the dark grey area corresponds to etched regions. Blue and red regions correspond to the expanded and shrunken lattices, respectively. The drawings are not to scale.

30  $\mu\text{m}$   $\times$  60  $\mu\text{m}$ . To have operation around 1550 nm wavelength, all the design parameters (size of the holes, distance between them, lattice periodicity, etc.) were scaled by a factor of 1.1 compared to the values presented in Fig. 4.A.1. The final fabricated bulk lattices had a lattice periodicity of 880 nm.

### 5.A.2. Experimental setup details

Here, we provide details on the experimental setup (Fig. 5.1) that we use for far-field real-space imaging of the edge states. We use a monochromatic continuous-wave laser (Toptica CTL) as the excitation source. Light from the laser is delivered to the setup using an infrared (IR) fibre. The IR light from the fibre is collimated by an achromatic lens and passed through an OD:1 neutral density filter. The polarization optics at the input include a quarter wave plate and a linear polarizer. The light is steered into an aspheric objective (Newport 5721-C-H, 60x, NA=0.6) using a beam splitter. The objective lens focuses light onto the sample and collects reflected light. The sample plane is finally imaged onto an infrared camera (AVT Goldeye P-008 SWIR) using a tube lens. A separate source (Thorlabs fibre illuminator, not shown in the diagram) is used for white light imaging of the sample.

To produce the dispersion maps in Figs. 5.5, 5.7 and 5.9, we used the same experimental procedure described under the title ‘dispersion measurements’

in appendix 4.A.3.

### 5.A.3. Extraction of cavity mode quality factors

To illustrate the variation of the quality factor of modes as we change the circumference of cavities, we choose a single mode around 215 THz that is common to all the cavities  $ER_{1-4}$  that we consider in Fig. 5.5a-d. For each of the cavities, we take six crosscuts in the corresponding dispersion diagrams. To find the quality factor of the cavity modes, we fit a model to the normalized reflection obtained from cross cuts in the dispersion diagram. The model is of the form:

$$R(\omega) = \left| A_0 + \sum_{j=1}^2 A_j e^{i\phi_j} \frac{\gamma_j}{\omega - \omega_{0_j} + i\gamma_j} \right|^2, \quad (5.A.1)$$

where  $A_0$  is a constant background amplitude;  $A$ ,  $\phi$  and  $\omega_0 - i\gamma$  are the amplitude, phase and complex frequency, respectively, of two individual Lorentzians. Quality factors are defined as  $Q_j = \omega_{0_j} / (2\gamma_j)$ . One Lorentzian models the cavity mode, while the other (broad) Lorentzian accounts for the slowly varying background reflection in the range of frequencies that we consider.



# BIBLIOGRAPHY

1. S. Battersby, *News Feature: The solar cell of the future*, Proc. Natl. Acad. Sci. U.S.A. **116**, 7 (2019).
2. S. Sukumaran and K. Sudhakar, *Fully solar powered airport: A case study of Cochin International airport*, J. Air Transp. Manag. **62**, 176 (2017).
3. J. Hecht, *City of Light: The Story of Fiber Optics* (Oxford University Press, 2004).
4. G. P. Agrawal, *Fiber-Optic Communication Systems* (John Wiley & Sons, 2012).
5. A. G. Bell, *On the production and reproduction of sound by light*, Am. J. Sci. **20**, 305 (1880).
6. L. Novotny and B. Hecht, *Principles of Nano-Optics* (Cambridge University Press, 2006).
7. H. J. Caulfield and S. Dolev, *Why future supercomputing requires optics*, Nat. Photonics **4**, 261 (2010).
8. J. L. O'Brien, A. Furusawa, and J. Vučković, *Photonic quantum technologies*, Nat. Photonics **3**, 687 (2009).
9. M. Lipson, *Guiding, modulating, and emitting light on Silicon-challenges and opportunities*, J. Lightwave Technol. **23**, 4222 (2005).
10. R. Won and M. Paniccia, *Integrating silicon photonics*, Nat. Photonics **4**, 498 (2010).
11. G. R. Fowles, *Introduction to Modern Optics* (Courier Corporation, 2012).
12. G. A. Reider, *Photonics: An Introduction* (Springer, 2016).
13. E. Hecht, *Optics* (Pearson Education, Incorporated, 2017).
14. M. Born and E. Wolf, *Principles of Optics: Electromagnetic Theory of Propagation, Interference and Diffraction of Light* (Cambridge University Press, 2000).
15. E. Wolf, *Introduction to the Theory of Coherence and Polarization of Light* (Cambridge University Press, 2007).
16. C. Kittel, *Introduction to Solid State Physics* (Wiley, 1976).
17. E. Yablonovitch, *Inhibited Spontaneous Emission in Solid-State Physics and Electronics*, Phys. Rev. Lett. **58**, 2059 (1987).
18. S. John, *Strong localization of photons in certain disordered dielectric superlattices*, Phys. Rev. Lett. **58**, 2486 (1987).
19. E. Yablonovitch and T. J. Gmitter, *Photonic band structure: The face-centered-cubic case*, Phys. Rev. Lett. **63**, 1950 (1989).

20. S. G. Johnson, *Photonic Crystals - From Theory to Practice*, Ph.D. thesis, MIT (2001).
21. J. D. Joannopoulos, S. G. Johnson, J. N. Winn, and R. D. Meade, *Photonic Crystals: Molding the Flow of Light - Second Edition* (Princeton University Press, 2011).
22. J. D. Jackson, *Classical Electrodynamics* (Wiley, 1999).
23. P. S. J. Russell, *Optics of Floquet-Bloch waves in dielectric gratings*, Appl. Phys. B **39**, 231 (1986).
24. G. B. Arfken, H.-J. Weber, and F. E. Harris, *Mathematical Methods for Physicists* (Elsevier, 2005).
25. S. G. Johnson, S. Fan, P. R. Villeneuve, J. D. Joannopoulos, and L. A. Kolodziejski, *Guided modes in photonic crystal slabs*, Phys. Rev. B **60**, 5751 (1999).
26. E. Chow, S. Lin, S. Johnson, P. Villeneuve, J. Joannopoulos, J. Wendt, G. Vawter, W. Zubrzycki, H. Hou, and A. Alleman, *Three-dimensional control of light in a two-dimensional photonic crystal slab*, Nature **407**, 983 (2000).
27. W. T. B. Kelvin, *Baltimore Lectures on Molecular Dynamics and the Wave Theory of Light* (C.J. Clay and Sons, 1904).
28. M. Asorey, *Space, matter and topology*, Nat. Phys. **12**, 616 (2016).
29. L. Lu, J. D. Joannopoulos, and M. Soljačić, *Topological Photonics*, Nat. Photonics **8**, 821 (2014).
30. T. Ozawa, H. M. Price, A. Amo, N. Goldman, M. Hafezi, L. Lu, M. C. Rechtsman, D. Schuster, J. Simon, O. Zilberberg, and I. Carusotto, *Topological photonics*, Rev. Mod. Phys. **91** (2019).
31. K. v. Klitzing, G. Dorda, and M. Pepper, *New Method for High-Accuracy Determination of the Fine-Structure Constant Based on Quantized Hall Resistance*, Phys. Rev. Lett. **45**, 494 (1980).
32. M. Z. Hasan and C. L. Kane, *Colloquium: Topological Insulators*, Rev. Mod. Phys. **82**, 3045 (2010).
33. C. L. Kane and E. J. Mele, *Quantum Spin Hall Effect in Graphene*, Phys. Rev. Lett. **95**, 226801 (2005).
34. B. A. Bernevig, T. L. Hughes, and S.-C. Zhang, *Quantum Spin Hall Effect and Topological Phase Transition in HgTe Quantum Wells*, Science **314**, 1757 (2006).
35. M. König, S. Wiedmann, C. Brüne, A. Roth, H. Buhmann, L. W. Molenkamp, X.-L. Qi, and S.-C. Zhang, *Quantum Spin Hall Insulator State in HgTe Quantum Wells*, Science **318**, 766 (2007).
36. D. J. Griffiths, *Introduction to Quantum Mechanics* (Cambridge University Press, 2016).
37. K. Y. Bliokh and Y. P. Bliokh, *Conservation of Angular Momentum*,

- Transverse Shift, and Spin Hall Effect in Reflection and Refraction of an Electromagnetic Wave Packet*, Phys. Rev. Lett. **96**, 073903 (2006).
38. O. Hosten and P. Kwiat, *Observation of the Spin Hall Effect of Light via Weak Measurements*, Science **319**, 787 (2008).
  39. M. Hafezi, S. Mittal, J. Fan, A. Migdall, and J. M. Taylor, *Imaging topological edge states in silicon photonics*, Nat. Photonics **7**, 1001 (2013).
  40. K. Y. Bliokh, D. Smirnova, and F. Nori, *Quantum Spin Hall Effect of Light*, Science **348**, 1448 (2015).
  41. W. P. Su, J. R. Schrieffer, and A. J. Heeger, *Solitons in Polyacetylene*, Phys. Rev. Lett. **42**, 1698 (1979).
  42. W. P. Su, J. R. Schrieffer, and A. J. Heeger, *Soliton excitations in polyacetylene*, Phys. Rev. B **22**, 2099 (1980).
  43. N. W. Ashcroft and N. D. Mermin, *Solid State Physics* (Saunders College, 1976).
  44. J. K. Asbóth, L. Oroszlány, and A. Pályi, *A Short Course on Topological Insulators: Band Structure and Edge States in One and Two Dimensions*, Lecture Notes in Physics (Springer International Publishing, 2016).
  45. M. Esmann and N. D. Lanzillotti-Kimura, *A Topological View on Optical and Phononic Fabry–Perot Microcavities through the Su–Schrieffer–Heeger Model*, Appl. Sci. **8**, 527 (2018).
  46. M. S. Rider, S. J. Palmer, S. R. Pocock, X. Xiao, P. Arroyo Huidobro, and V. Giannini, *A perspective on topological nanophotonics: Current status and future challenges*, J. Appl. Phys. **125**, 120901 (2019).
  47. F. Alpeggiani, N. Parappurath, E. Verhagen, and L. Kuipers, *Quasinormal-mode expansion of the scattering matrix*, Phys. Rev. X **7**, 021035 (2017).
  48. D. M. Pozar, *Microwave Engineering*, 4th ed. (Wiley, 2012).
  49. C. Bohren and D. Huffman, *Absorption and Scattering of Light by Small Particles* (Wiley, New York, 1983).
  50. D. M. Whittaker and I. S. Culshaw, *Scattering-matrix treatment of patterned multilayer photonic structures*, Phys. Rev. B **60**, 2610 (1999).
  51. M. Liscidini, D. Gerace, L. C. Andreani, and J. E. Sipe, *Scattering-matrix analysis of periodically patterned multilayers with asymmetric unit cells and birefringent media*, Phys. Rev. B **77**, 035324 (2008).
  52. P. Lalanne, W. Yan, K. Vynck, C. Sauvan, and J.-P. Hugonin, *Light Interaction with Photonic and Plasmonic Resonances*, Laser Photonics Rev. **12** (2018).
  53. M. Nevière, R. Reinisch, and E. Popov, *Electromagnetic resonances in linear and nonlinear optics: Phenomenological study of grating behavior through the poles and zeros of the scattering operator*, J. Opt. Soc. Am. A **12**, 513 (1995).
  54. S. G. Tikhodeev, A. L. Yablonskii, E. A. Muljarov, N. A. Gippius, and

- T. Ishihara, *Quasiguidded modes and optical properties of photonic crystal slabs*, Phys. Rev. B **66** (2002).
55. S. Fan, W. Suh, and J. D. Joannopoulos, *Temporal coupled-mode theory for the Fano resonance in optical resonators*, J. Opt. Soc. Am. A **20**, 569 (2003).
56. C. W. Hsu, B. G. DeLacy, S. G. Johnson, J. D. Joannopoulos, and M. Soljčić, *Theoretical Criteria for Scattering Dark States in Nanostructured Particles*, Nano Lett. **14**, 2783 (2014).
57. R. Alaee, D. Lehr, R. Filter, F. Lederer, E.-B. Kley, C. Rockstuhl, and A. Tünnermann, *Scattering Dark States in Multiresonant Concentric Plasmonic Nanorings*, ACS Photonics **2**, 1085 (2015).
58. L. Verslegers, Z. Yu, Z. Ruan, P. B. Catrysse, and S. Fan, *From Electromagnetically Induced Transparency to Superscattering with a Single Structure: A Coupled-Mode Theory for Doubly Resonant Structures*, Phys. Rev. Lett. **108** (2012).
59. M. Decker, I. Staude, M. Falkner, J. Dominguez, D. N. Neshev, I. Brener, T. Pertsch, and Y. S. Kivshar, *High-Efficiency Dielectric Huygens' Surfaces*, Adv. Opt. Mat. **3**, 813 (2015).
60. S. Fan and J. D. Joannopoulos, *Analysis of guided resonances in photonic crystal slabs*, Phys. Rev. B **65** (2002).
61. K. X. Wang, Z. Yu, S. Sandhu, and S. Fan, *Fundamental bounds on decay rates in asymmetric single-mode optical resonators*, Opt. Lett. **38**, 100 (2013).
62. D. A. Bykov and L. L. Doskolovich, *Spatiotemporal coupled-mode theory of guided-mode resonant gratings*, Opt. Express **23**, 19234 (2015).
63. W. Suh, Z. Wang, and S. Fan, *Temporal coupled-mode theory and the presence of non-orthogonal modes in lossless multimode cavities*, IEEE J. Quantum Elect. **40**, 1511 (2004).
64. E. Waks and J. Vuckovic, *Coupled mode theory for photonic crystal cavity-waveguide interaction*, Opt. Express **13**, 5064 (2005).
65. R. E. Hamam, A. Karalis, J. D. Joannopoulos, and M. Soljčić, *Coupled-mode theory for general free-space resonant scattering of waves*, Phys. Rev. A **75**, 053801 (2007).
66. Z. Ruan and S. Fan, *Temporal coupled-mode theory for light scattering by an arbitrarily shaped object supporting a single resonance*, Phys. Rev. A **85**, 043828 (2012).
67. P. T. Leung, S. Y. Liu, and K. Young, *Completeness and orthogonality of quasinormal modes in leaky optical cavities*, Phys. Rev. A **49**, 3057 (1994).
68. R.-C. Ge, P. T. Kristensen, J. F. Young, and S. Hughes, *Quasinormal mode approach to modelling light-emission and propagation in nanoplasmonics*, New J. Phys. **16**, 113048 (2014).
69. Q. Bai, M. Perrin, C. Sauvan, J.-P. Hugonin, and P. Lalanne, *Efficient and intuitive method for the analysis of light scattering by a resonant nanostructure*, Opt. Express **21**, 27371 (2013).



70. B. Vial, F. Zolla, A. Nicolet, and M. Commandré, *Quasimodal expansion of electromagnetic fields in open two-dimensional structures*, Phys. Rev. A **89**, 023829 (2014).
71. E. A. Muljarov, W. Langbein, and R. Zimmermann, *Brillouin–Wigner perturbation theory in open electromagnetic systems*, Europhys. Lett. **92**, 50010 (2010).
72. P. T. Kristensen, C. V. Vlack, and S. Hughes, *Generalized effective mode volume for leaky optical cavities*, Opt. Lett. **37**, 1649 (2012).
73. C. Sauvan, J. P. Hugonin, I. S. Maksymov, and P. Lalanne, *Theory of the Spontaneous Optical Emission of Nanosize Photonic and Plasmon Resonators*, Phys. Rev. Lett. **110**, 237401 (2013).
74. E. A. Muljarov and W. Langbein, *Resonant-state expansion of dispersive open optical systems: Creating gold from sand*, Phys. Rev. B **93**, 075417 (2016).
75. F. Ruesink, M.-A. Miri, A. Alù, and E. Verhagen, *Nonreciprocity and magnetic-free isolation based on optomechanical interactions*, Nat. Commun. **7**, 13662 (2016).
76. D. C. Brody, *Biorthogonal quantum mechanics*, J. Phys. A: Math. Theor. **47**, 035305 (2013).
77. O. Bretscher, *Linear Algebra with Applications*, 4th ed. (Pearson, 2009).
78. V. Liu and S. Fan, *S4: A free electromagnetic solver for layered periodic structures*, Comput. Phys. Commun. **183**, 2233 (2012).
79. J. Yang, J.-P. Hugonin, and P. Lalanne, *Near-to-Far Field Transformations for Radiative and Guided Waves*, ACS Photonics **3**, 395 (2016).
80. S. Jahani and Z. Jacob, *All-dielectric metamaterials*, Nat. Nanotech. **11**, 23 (2016).
81. A. B. Klemm, D. Stellinga, E. R. Martins, L. Lewis, G. Huyet, L. O’Faolain, and T. F. Krauss, *Experimental high numerical aperture focusing with high contrast gratings*, Opt Lett **38**, 3410 (2013).
82. N. Yu and F. Capasso, *Flat optics with designer metasurfaces*, Nat. Mater. **13**, 139 (2014).
83. D. Lin, P. Fan, E. Hasman, and M. L. Brongersma, *Dielectric gradient metasurface optical elements*, Science **345**, 298 (2014).
84. P. Moitra, Y. Yang, Z. Anderson, I. I. Kravchenko, D. P. Briggs, and J. Valentine, *Realization of an all-dielectric zero-index optical metamaterial*, Nat. Photonics **7**, 791 (2013).
85. V. A. Fedotov, P. L. Mladyonov, S. L. Prosvirnin, A. V. Rogacheva, Y. Chen, and N. I. Zheludev, *Asymmetric propagation of electromagnetic waves through a planar chiral structure*, Phys. Rev. Lett. **97** (2006).
86. C. Menzel, C. Helgert, C. Rockstuhl, E.-B. Kley, A. Tünnermann, T. Pertsch, and F. Lederer, *Asymmetric transmission of linearly polarized light at optical metamaterials*, Phys. Rev. Lett. **104** (2010).

87. A. Alù and N. Engheta, *Multifrequency Optical Invisibility Cloak with Layered Plasmonic Shells*, Phys. Rev. Lett. **100**, 113901 (2008).
88. A. Vázquez-Guardado, A. Safaei, S. Modak, D. Franklin, and D. Chanda, *Hybrid Coupling Mechanism in a System Supporting High Order Diffraction, Plasmonic, and Cavity Resonances*, Phys. Rev. Lett. **113**, 263902 (2014).
89. H. M. Doeleman, E. Verhagen, and A. F. Koenderink, *Antenna–Cavity Hybrids: Matching Polar Opposites for Purcell Enhancements at Any Linewidth*, ACS Photonics **3**, 1943 (2016).
90. S. R. K. Rodriguez, J. Feist, M. A. Verschuuren, F. J. Garcia Vidal, and J. Gómez Rivas, *Thermalization and Cooling of Plasmon-Exciton Polaritons: Towards Quantum Condensation*, Phys. Rev. Lett. **111**, 166802 (2013).
91. N. Parappurath, F. Alpeggiani, L. Kuipers, and E. Verhagen, *The origin and limit of asymmetric transmission in chiral resonators*, ACS Photonics **4**, 884 (2017).
92. T. Vallius, K. Jefimovs, J. Turunen, P. Vahimaa, and Y. Svirko, *Optical activity in subwavelength-period arrays of chiral metallic particles*, Appl. Phys. Lett. **83**, 234 (2003).
93. A. Papakostas, A. Potts, D. M. Bagnall, S. L. Prosvirnin, H. J. Coles, and N. I. Zheludev, *Optical manifestations of planar chirality*, Phys. Rev. Lett. **90** (2003).
94. M. Kuwata-Gonokami, N. Saito, Y. Ino, M. Kauranen, K. Jefimovs, T. Vallius, J. Turunen, and Y. Svirko, *Giant optical activity in quasi-two-dimensional planar nanostructures*, Phys. Rev. Lett. **95** (2005).
95. W. L. Barnes, A. Dereux, and T. W. Ebbesen, *Surface plasmon subwavelength optics*, Nature **424**, 824 (2003).
96. L. Novotny and N. van Hulst, *Antennas for light*, Nat. Photonics **5**, 83 (2011).
97. S. Fan, J. D. Joannopoulos, J. N. Winn, A. Devenyi, J. C. Chen, and R. D. Meade, *Guided and defect modes in periodic dielectric waveguides*, J. Opt. Soc. Am. B **12**, 1267 (1995).
98. J. B. Pendry, D. Schurig, and D. R. Smith, *Controlling electromagnetic fields*, Science **312**, 1780 (2006).
99. M. R. Watts and H. A. Haus, *Integrated mode-evolution-based polarization rotators*, Opt. Lett. **30**, 138 (2005).
100. K. Bayat, S. K. Chaudhuri, and S. Safavi-Naeini, *Ultra-compact photonic crystal based polarization rotator*, Opt. Express **17**, 7145 (2009).
101. N. Yu, F. Aieta, P. Genevet, M. A. Kats, Z. Gaburro, and F. Capasso, *A broadband, background-free quarter-wave plate based on plasmonic metasurfaces*, Nano Lett. **12**, 6328 (2012).
102. B. Shen, P. Wang, R. Polson, and R. Menon, *An integrated-nanophotonics polarization beamsplitter with  $2.4 \times 2.4 \mu\text{m}^2$  footprint*, Nat. Photonics **9**, 378 (2015).

103. H. Zhou, B. Zhen, C. W. Hsu, O. D. Miller, S. G. Johnson, J. D. Joannopoulos, and M. Soljačić, *Perfect single-sided radiation and absorption without mirrors*, *Optica* **3**, 1079 (2016).
104. K. Konishi, M. Nomura, N. Kumagai, S. Iwamoto, Y. Arakawa, and M. Kuwata-Gonokami, *Circularly polarized light emission from semiconductor planar chiral nanostructures*, *Phys. Rev. Lett.* **106** (2011).
105. B. le Feber, N. Rotenberg, and L. Kuipers, *Nanophotonic control of circular dipole emission*, *Nat. Commun.* **6**, 6695 (2015).
106. K. Y. Bliokh, F. J. Rodríguez-Fortuño, F. Nori, and A. V. Zayats, *Spin-orbit interactions of light*, *Nat. Photonics* **9**, 796 (2015).
107. Y. Tang and A. E. Cohen, *Enhanced enantioselectivity in excitation of chiral molecules by superchiral light*, *Science* **332**, 333 (2011).
108. A. S. Schwanecke, V. A. Fedotov, V. V. Khardikov, S. L. Prosvirnin, Y. Chen, and N. I. Zheludev, *Nanostructured metal film with asymmetric optical transmission*, *Nano Lett.* **8**, 2940 (2008).
109. A. Drezet, C. Genet, J.-Y. Laluet, and T. W. Ebbesen, *Optical chirality without optical activity: How surface plasmons give a twist to light*, *Opt. Express* **16**, 12559 (2008).
110. R. Singh, E. Plum, C. Menzel, C. Rockstuhl, A. K. Azad, R. A. Cheville, F. Lederer, W. Zhang, and N. I. Zheludev, *Terahertz metamaterial with asymmetric transmission*, *Phys. Rev. B* **80** (2009).
111. E. Plum, V. A. Fedotov, and N. I. Zheludev, *Planar metamaterial with transmission and reflection that depend on the direction of incidence*, *Appl. Phys. Lett.* **94**, 131901 (2009).
112. K. Konishi, B. Bai, X. Meng, P. Karvinen, J. Turunen, Y. P. Svirko, and M. Kuwata-Gonokami, *Observation of extraordinary optical activity in planar chiral photonic crystals*, *Opt. Express* **16**, 7189 (2008).
113. X. Meng, B. Bai, P. Karvinen, K. Konishi, J. Turunen, Y. Svirko, and M. Kuwata-Gonokami, *Experimental realization of all-dielectric planar chiral metamaterials with large optical activity in direct transmission*, *Thin Solid Films* **516**, 8745 (2008).
114. C. Menzel, C. Rockstuhl, and F. Lederer, *Advanced Jones calculus for the classification of periodic metamaterials*, *Phys. Rev. A* **82** (2010).
115. M. Mutlu, A. E. Akosman, A. E. Serebryannikov, and E. Ozbay, *Diodelike asymmetric transmission of linearly polarized waves using magnetoelectric coupling and electromagnetic wave tunneling*, *Phys. Rev. Lett.* **108**, 213905 (2012).
116. Z. Li, M. Gokkavas, and E. Ozbay, *Manipulation of asymmetric transmission in planar chiral nanostructures by anisotropic loss*, *Adv. Opt. Mater.* **1**, 482 (2013).
117. D.-j. Liu, Z.-y. Xiao, X.-l. Ma, and Z.-h. Wang, *Broadband asymmetric transmission and multi-band 90° polarization rotator of linearly polarized wave based on multi-layered metamaterial*, *Opt. Commun.* **354**, 272 (2015).

118. G. Kenanakis, A. Xomalis, A. Selimis, M. Vamvakaki, M. Farsari, M. Kafesaki, C. M. Soukoulis, and E. N. Economou, *Three-dimensional infrared metamaterial with asymmetric transmission*, ACS Photonics **2**, 287 (2015).
119. M. Hamermesh, *Group Theory and Its Application to Physical Problems* (Courier Corporation, 1962).
120. N. Parappurath, F. Alpeggiani, L. Kuipers, and E. Verhagen, *Direct Observation of Topological Edge States in Silicon Photonic Crystals: Spin, Dispersion, and Chiral Routing*, arXiv:1811.10739 (2018).
121. K. von Klitzing, *The Quantized Hall Effect*, Rev. Mod. Phys. **58**, 519 (1986).
122. Z. Wang, Y. Chong, J. D. Joannopoulos, and M. Soljačić, *Observation of unidirectional backscattering-immune topological electromagnetic states*, Nature **461**, 772 (2009).
123. A. B. Khanikaev, S. Hossein Mousavi, W.-K. Tse, M. Kargarian, A. H. MacDonald, and G. Shvets, *Photonic topological insulators*, Nat. Mater. **12**, 233 (2013).
124. M. C. Rechtsman, J. M. Zeuner, Y. Plotnik, Y. Lumer, D. Podolsky, F. Dreisow, S. Nolte, M. Segev, and A. Szameit, *Photonic Floquet topological insulators*, Nature **496**, 196 (2013).
125. W.-J. Chen, S.-J. Jiang, X.-D. Chen, B. Zhu, L. Zhou, J.-W. Dong, and C. T. Chan, *Experimental realization of photonic topological insulator in a uniaxial metacrystal waveguide*, Nat. Commun. **5**, 5782 (2014).
126. M. Bellec, U. Kuhl, G. Montambaux, and F. Mortessagne, *Manipulation of Edge States in Microwave Artificial Graphene*, New J. Phys. **16**, 113023 (2014).
127. A. P. Slobozhanyuk, A. N. Poddubny, A. E. Miroshnichenko, P. A. Belov, and Y. S. Kivshar, *Subwavelength Topological Edge States in Optically Resonant Dielectric Structures*, Phys. Rev. Lett. **114**, 123901 (2015).
128. R. Fleury, A. B. Khanikaev, and A. Alù, *Floquet topological insulators for sound*, Nat. Commun. **7**, 11744 (2016).
129. C. He, X. Ni, H. Ge, X.-C. Sun, Y.-B. Chen, M.-H. Lu, X.-P. Liu, and Y.-F. Chen, *Acoustic Topological Insulator and Robust One-Way Sound Transport*, Nat. Phys. **12**, 1124 (2016).
130. X. Cheng, C. Jouvaud, X. Ni, S. H. Mousavi, A. Z. Genack, and A. B. Khanikaev, *Robust reconfigurable electromagnetic pathways within a photonic topological insulator*, Nat. Mater. **15**, 542 (2016).
131. M. Milićević, T. Ozawa, G. Montambaux, I. Carusotto, E. Galopin, A. Lemaître, L. Le Gratiet, I. Sagnes, J. Bloch, and A. Amo, *Orbital Edge States in a Photonic Honeycomb Lattice*, Phys. Rev. Lett. **118**, 107403 (2017).
132. J. Noh, S. Huang, K. P. Chen, and M. C. Rechtsman, *Observation of Photonic Topological Valley Hall Edge States*, Phys. Rev. Lett. **120**, 063902 (2018).

133. Y. Lumer, M. A. Bandres, M. Heinrich, L. J. Maczewsky, H. Herzig-Sheinfux, A. Szameit, and M. Segev, *Light guiding by artificial gauge fields*, Nat. Photonics , 339 (2019).
134. S. Stützer, Y. Plotnik, Y. Lumer, P. Titum, N. H. Lindner, M. Segev, M. C. Rechtsman, and A. Szameit, *Photonic topological Anderson insulators*, Nature **560**, 461 (2018).
135. C. Brendel, V. Peano, O. Painter, and F. Marquardt, *Snowflake Phononic Topological Insulator at the Nanoscale*, Phys. Rev. B **97**, 020102 (2018).
136. V. G. Sala, D. D. Solnyshkov, I. Carusotto, T. Jacqmin, A. Lemaître, H. Terças, A. Nalitov, M. Abbarchi, E. Galopin, I. Sagnes, J. Bloch, G. Malpuech, and A. Amo, *Spin-Orbit Coupling for Photons and Polaritons in Microstructures*, Phys. Rev. X **5**, 011034 (2015).
137. S. Mittal, J. Fan, S. Faez, A. Migdall, J. M. Taylor, and M. Hafezi, *Topologically Robust Transport of Photons in a Synthetic Gauge Field*, Phys. Rev. Lett. **113**, 087403 (2014).
138. S. Mittal, S. Ganeshan, J. Fan, A. Vaezi, and M. Hafezi, *Measurement of topological invariants in a 2D photonic system*, Nat. Photonics **10**, 180 (2016).
139. S. Mittal, E. A. Goldschmidt, and M. Hafezi, *A topological source of quantum light*, Nature **561**, 502 (2018).
140. M. A. Bandres, S. Wittek, G. Harari, M. Parto, J. Ren, M. Segev, D. N. Christodoulides, and M. Khajavikhan, *Topological Insulator Laser: Experiments*, Science **359**, eaar4005 (2018).
141. L.-H. Wu and X. Hu, *Scheme for Achieving a Topological Photonic Crystal by Using Dielectric Material*, Phys. Rev. Lett. **114**, 223901 (2015).
142. S. Barik, H. Miyake, W. DeGottardi, E. Waks, and M. Hafezi, *Two-Dimensionally Confined Topological Edge States in Photonic Crystals*, New J. Phys. **18**, 113013 (2016).
143. P. D. Anderson and G. Subramania, *Unidirectional Edge States in Topological Honeycomb-Lattice Membrane Photonic Crystals*, Opt. Express **25**, 23293 (2017).
144. S. Yves, R. Fleury, T. Berthelot, M. Fink, F. Lemoult, and G. Lerosey, *Crystalline metamaterials for topological properties at subwavelength scales*, Nat. Commun. **8**, 16023 (2017).
145. Y. Yang, Y. F. Xu, T. Xu, H.-X. Wang, J.-H. Jiang, X. Hu, and Z. H. Hang, *Visualization of a Unidirectional Electromagnetic Waveguide Using Topological Photonic Crystals Made of Dielectric Materials*, Phys. Rev. Lett. **120**, 217401 (2018).
146. S. Barik, A. Karasahin, C. Flower, T. Cai, H. Miyake, W. DeGottardi, M. Hafezi, and E. Waks, *A Topological Quantum Optics Interface*, Science **359**, 666 (2018).
147. T. Ma and G. Shvets, *All-Si Valley-Hall Photonic Topological Insulator*, New J. Phys. **18**, 025012 (2016).

- 148. M. I. Shalaev, W. Walasik, A. Tsukernik, Y. Xu, and N. M. Litchinitser, *Robust topologically protected transport in photonic crystals at telecommunication wavelengths*, Nat. Nanotech. **14**, 31 (2018).
- 149. X.-T. He, E.-T. Liang, J.-J. Yuan, H.-Y. Qiu, X.-D. Chen, F.-L. Zhao, and J.-W. Dong, *A silicon-on-insulator slab for topological valley transport*, Nat. Commun. **10**, 872 (2019).
- 150. M. A. Gorlach, X. Ni, D. A. Smirnova, D. Korobkin, D. Zhirihin, A. P. Slobozhanyuk, P. A. Belov, A. Alù, and A. B. Khanikaev, *Far-field probing of leaky topological states in all-dielectric metasurfaces*, Nat. Commun. **9**, 909 (2018).
- 151. P. St-Jean, V. Goblot, E. Galopin, A. Lemaître, T. Ozawa, L. L. Gratiet, I. Sagnes, J. Bloch, and A. Amo, *Lasing in Topological Edge States of a One-Dimensional Lattice*, Nat. Photonics **11**, 651 (2017).
- 152. T. H. Taminiau, S. Karaveli, N. F. van Hulst, and R. Zia, *Quantifying the Magnetic Nature of Light Emission*, Nat. Commun. **3**, 979 (2012).
- 153. B. Schaefer, E. Collett, R. Smyth, D. Barrett, and B. Fraher, *Measuring the Stokes polarization parameters*, Am. J. Phys. **75**, 163 (2007).
- 154. L. Xu, H.-X. Wang, Y.-D. Xu, H.-Y. Chen, and J.-H. Jiang, *Accidental Degeneracy in Photonic Bands and Topological Phase Transitions in Two-Dimensional Core-Shell Dielectric Photonic Crystals*, Opt. Express **24**, 18059 (2016).
- 155. T. Fösel, V. Peano, and F. Marquardt, *L lines, C points and Chern numbers: Understanding band structure topology using polarization fields*, New J. Phys. **19**, 115013 (2017).
- 156. V. R. Almeida, C. A. Barrios, R. R. Panepucci, and M. Lipson, *All-optical control of light on a silicon chip*, Nature **431**, 1081 (2004).
- 157. R. A. Soref, J. Schmidtchen, and K. Petermann, *Large single-mode rib waveguides in GeSi-Si and Si-on-SiO<sub>2</sub>*, IEEE J. Quantum Elect. **27**, 1971 (1991).
- 158. J. Schmidtchen, A. Splett, B. Schuppert, K. Petermann, and G. Burbach, *Low loss singlemode optical waveguides with large cross-section in silicon-on-insulator*, Electron. Lett. **27**, 1486 (1991).
- 159. K. K. Lee, *Transmission and Routing of Optical Signals in On-Chip Waveguides for Silicon Microphotonics*, Ph.D. thesis, MIT (2001).
- 160. S. G. Johnson, P. R. Villeneuve, S. Fan, and J. D. Joannopoulos, *Linear waveguides in photonic-crystal slabs*, Phys. Rev. B **62**, 8212 (2000).
- 161. M. Lončar, D. Nedeljković, T. Doll, J. Vučković, A. Scherer, and T. P. Pearsall, *Waveguiding in planar photonic crystals*, Appl. Phys. Lett. **77**, 1937 (2000).
- 162. M. Lončar, T. Doll, J. Vuckovic, and A. Scherer, *Design and fabrication of silicon photonic crystal optical waveguides*, J. Lightwave Technol. **18**, 1402 (2000).



163. A. Mekis, J. C. Chen, I. Kurland, S. Fan, P. R. Villeneuve, and J. D. Joannopoulos, *High Transmission through Sharp Bends in Photonic Crystal Waveguides*, Phys. Rev. Lett. **77**, 3787 (1996).
164. T. Baba, N. Fukaya, and J. Yonekura, *Observation of light propagation in photonic crystal optical waveguides with bends*, Electron. Lett. **35**, 654 (1999).
165. M. Tokushima, H. Kosaka, A. Tomita, and H. Yamada, *Lightwave propagation through a 120° sharply bent single-line-defect photonic crystal waveguide*, Appl. Phys. Lett. **76**, 952 (2000).
166. T. Baba and N. Fukaya, *Light Propagation Characteristics of Defect Waveguides in a Photonic Crystal Slab*, in *Photonic Crystals and Light Localization in the 21st Century*, NATO Science Series, edited by C. M. Soukoulis (Springer, 2001) pp. 105–116.
167. P. R. Villeneuve, S. Fan, and J. D. Joannopoulos, *Microcavities in photonic crystals: Mode symmetry, tunability, and coupling efficiency*, Phys. Rev. B **54**, 7837 (1996).
168. K. J. Vahala, *Optical microcavities*, Nature **424**, 839 (2003).
169. D. K. Armani, T. J. Kippenberg, S. M. Spillane, and K. J. Vahala, *Ultra-high-Q toroid microcavity on a chip*, Nature **421**, 925 (2003).
170. M. Aspelmeyer, T. J. Kippenberg, and F. Marquardt, *Cavity optomechanics*, Rev. Mod. Phys. **86**, 1391 (2014).
171. S. Fan, P. R. Villeneuve, J. D. Joannopoulos, and H. A. Haus, *Channel drop filters in photonic crystals*, Opt. Express **3**, 4 (1998).
172. K. Vahala, *Optical Microcavities* (World Scientific, 2004).
173. H. A. Haus, *Waves and Fields in Optoelectronics* (Prentice-Hall, 1984).
174. B. E. A. Saleh and M. C. Teich, *Fundamentals of Photonics* (Wiley, 2007).
175. B. E. Little and S. T. Chu, *Estimating surface-roughness loss and output coupling in microdisk resonators*, Opt. Lett. **21**, 1390 (1996).
176. Y. A. Vlasov and S. J. McNab, *Losses in single-mode silicon-on-insulator strip waveguides and bends*, Opt. Express **12**, 1622 (2004).
177. M. Notomi, A. Shinya, K. Yamada, J. Takahashi, C. Takahashi, and I. Yokohama, *Structural tuning of guiding modes of line-defect waveguides of silicon-on-insulator photonic crystal slabs*, IEEE J. Quantum Elect. **38**, 736 (2002).
178. S. J. McNab, N. Moll, and Y. A. Vlasov, *Ultra-low loss photonic integrated circuit with membrane-type photonic crystal waveguides*, Opt. Express **11**, 2927 (2003).
179. D. Gerace and L. C. Andreani, *Disorder-induced losses in photonic crystal waveguides with line defects*, Opt. Lett. **29**, 1897 (2004).
180. A. P. Slobozhanyuk, A. B. Khanikaev, D. S. Filonov, D. A. Smirnova, A. E. Miroshnichenko, and Y. S. Kivshar, *Experimental demonstration of topological effects in bianisotropic metamaterials*, Sci. Rep. **6**, 22270 (2016).

181. X. Wu, Y. Meng, J. Tian, Y. Huang, H. Xiang, D. Han, and W. Wen, *Direct observation of valley-polarized topological edge states in designer surface plasmon crystals*, Nat. Commun. **8**, 1304 (2017).
182. A. Slobozhanyuk, A. V. Shchelokova, X. Ni, S. Hossein Mousavi, D. A. Smirnova, P. A. Belov, A. Alù, Y. S. Kivshar, and A. B. Khanikaev, *Near-field imaging of spin-locked edge states in all-dielectric topological metasurfaces*, Appl. Phys. Lett. **114**, 031103 (2019).
183. D. Smirnova, S. Kruk, D. Leykam, E. Melik-Gaykazyan, D.-Y. Choi, and Y. Kivshar, *Nonlinear mapping of photonic topological edge states*, arXiv:1811.12130 (2018).
184. S. Yang, Y. Wang, and H. Sun, *Advances and Prospects for Whispering Gallery Mode Microcavities*, Adv. Opt. Mater. **3**, 1136 (2015).
185. G. Siroki, P. A. Huidobro, and V. Giannini, *Topological photonics: From crystals to particles*, Phys. Rev. B **96**, 041408 (2017).
186. Y. Yang and Z. H. Hang, *Topological whispering gallery modes in two-dimensional photonic crystal cavities*, Opt. Express **26**, 21235 (2018).
187. T. J. Kippenberg, S. M. Spillane, and K. J. Vahala, *Modal coupling in traveling-wave resonators*, Opt. Lett. **27**, 1669 (2002).
188. A. Mazzei, S. Götzinger, L. de S. Menezes, G. Zumofen, O. Benson, and V. Sandoghdar, *Controlled Coupling of Counterpropagating Whispering-Gallery Modes by a Single Rayleigh Scatterer: A Classical Problem in a Quantum Optical Light*, Phys. Rev. Lett. **99**, 173603 (2007).
189. J. Zhu, S. K. Ozdemir, Y.-F. Xiao, L. Li, L. He, D.-R. Chen, and L. Yang, *On-chip single nanoparticle detection and sizing by mode splitting in an ultrahigh-Q microresonator*, Nat. Photonics **4**, 46 (2010).
190. N. Rotenberg and L. Kuipers, *Mapping nanoscale light fields*, Nat. Photonics **8**, 919 (2014).
191. B. le Feber, N. Rotenberg, D. M. Beggs, and L. Kuipers, *Simultaneous measurement of nanoscale electric and magnetic optical fields*, Nat. Photonics **8**, 43 (2014).
192. H. Gersen, T. J. Karle, R. J. P. Engelen, W. Bogaerts, J. P. Korterik, N. F. van Hulst, T. F. Krauss, and L. Kuipers, *Direct Observation of Bloch Harmonics and Negative Phase Velocity in Photonic Crystal Waveguides*, Phys. Rev. Lett. **94**, 123901 (2005).
193. M. Burrelli, R. J. P. Engelen, A. Opheij, D. van Oosten, D. Mori, T. Baba, and L. Kuipers, *Observation of Polarization Singularities at the Nanoscale*, Phys. Rev. Lett. **102**, 033902 (2009).
194. K. Karrai and R. D. Grober, *Piezoelectric tip-sample distance control for near field optical microscopes*, Appl. Phys. Lett. **66**, 1842 (1995).
195. M. L. M. Balistreri, J. P. Korterik, L. Kuipers, and N. F. van Hulst, *Local Observations of Phase Singularities in Optical Fields in Waveguide Structures*, Phys. Rev. Lett. **85**, 294 (2000).



196. B. le Feber, J. E. Sipe, M. Wulf, L. Kuipers, and N. Rotenberg, *A full vectorial mapping of nanophotonic light fields*, *Light: Sci. Appl.* **8**, 28 (2019).
197. L. De Angelis, F. Alpeggiani, and L. Kuipers, *Spatial Bunching of Same-Index Polarization Singularities in Two-Dimensional Random Vector Waves*, *Phys. Rev. X* **8**, 041012 (2018).
198. C. P. Reardon, I. H. Rey, K. Welna, L. O’Faolain, and T. F. Krauss, *Fabrication And Characterization Of Photonic Crystal Slow Light Waveguides And Cavities*, *J. Vis. Exp.* **69**, e50216 (2012).
199. P. Lodahl, S. Mahmoodian, S. Stobbe, A. Rauschenbeutel, P. Schneeweiss, J. Volz, H. Pichler, and P. Zoller, *Chiral quantum optics*, *Nature* **541**, 473 (2017).
200. Y. Wu, C. Li, X. Hu, Y. Ao, Y. Zhao, and Q. Gong, *Applications of Topological Photonics in Integrated Photonic Devices*, *Adv. Opt. Mater.* **5**, 1700357 (2017).



# SUMMARY

## Chiral flow of light in photonic crystals with broken symmetries

Light forms an integral part of our existence in this planet. In one way or another, it continues to assist, amaze and inspire us everyday. It plays a crucial role in the advancement of science and technology, supporting a great number of applications to enhance the quality of our daily lives. The interaction of light with matter plays a significant role in these applications. One can bring about diverse novel effects by making light interact with matter at scales smaller than the wavelength. Tailoring this interaction can be made possible by structuring materials in smart ways and by making use of inherent properties of light. An important attribute of light is the fact that electromagnetic fields are *vectorial* in nature, giving light waves the ability to carry distinct polarizations.

Photonic crystals are structures featuring a periodic arrangement of materials at the nanoscale. In this thesis, employing concepts like chirality and topology, we explore the interaction of polarized light with photonic crystals of different geometries. We utilize different structural symmetries — and the breaking of these — to achieve interesting effects like asymmetric transmission and back-scattering-free transport of light.

We introduce a few key concepts in the lead-in chapter (Ch. 1). A discussion of the vectorial nature of light is presented with a focus on different means for representation and quantification of polarized light, e.g., Stokes parameters. We then introduce photonic crystals, emphasizing the physics of propagation of light in the form of Bloch waves, the relations between optical frequencies and wave vectors that feature photonic bandgaps, and the confinement and guiding of light with the help of photonic crystal slabs.

*Chiral* photonic crystals, which lack mirror symmetry, are of special interest in this thesis. The possibilities for manipulation of polarized light through interaction with general chiral objects is briefly presented. The introductory chapter concludes with a short review of the concept of *topology* in photonics, which plays an important role in the second part of the thesis. We concentrate on the physics of states living at the edges of topological systems. The propagation of such states can be protected against backscattering from defects. This thesis describes the realization of an optical analogue of the quantum spin Hall effect for electrons (where in our case light waves of different “spin”, like opposite-spin electrons, feature backscattering-free transport in opposite directions). In the final section of the chapter, we look at the origin

of topological edge states from symmetry breaking and band inversion in a physical system, considering an intuitive theoretical model called the Su-Schrieffer-Heeger model.

The first part of this thesis investigates resonances in photonic systems in connection with their scattering properties. The theoretical studies presented in the two chapters of this part provide methods for realization, tailoring and optimization of attractive properties in nanophotonic systems. The response of physical systems to external light waves is dictated mainly by the interaction of light with the eigenmodes that can leak out of the system. Such modes are called quasinormal modes. A mathematical tool called the scattering matrix offers a convenient method to quantify the response of the system to external light. We develop a theoretical formalism based on coupled-mode theory in chapter 2 to predict the scattering matrix of optical systems from the far-field properties of their quasinormal modes. In contrast to the existing theoretical approaches, we show that our formalism can be scaled to a wider range of frequencies and a larger number of incoming and outgoing channels, to predict the scattering response from the properties of a select number of calculated modes.

A better understanding of the optical response of physical systems helps us to realize compact polarization manipulation devices at the nanoscale. In chapter 3, we apply the developed theoretical formalism in the context of interaction of polarized light with chiral systems, to investigate a distinct form of chiral response: asymmetric transmission (AT). Asymmetric transmission is the difference in transmittances of a polarized light wave incident on a system from opposite directions. We reveal the connection between this resonant chiral response and the non-resonant properties of the system, and use our theoretical formalism to predict AT for any given system. We discover that the principle of reciprocity imposes a fundamental limit to the maximum possible AT in physical systems. Finally, we show a design route towards optimized structures that can offer the maximum possible AT in dielectric structures, demonstrating this route in the example of a strongly chiral photonic crystal slab.

Owing to its promising applications in routing and manipulation of light in the classical and quantum regime, the concept of topology has recently attracted significant interest in the photonic domain. The second part of the thesis is devoted to the physics, realization, and experimental investigations of topological edge states in silicon photonic crystals. In chapter 4, we fabricate a topological photonic system consisting of an interface between two photonic crystals of slightly different geometries on a silicon-on-insulator chip. The two photonic crystals feature different band structure topologies, and can support topologically-protected edge states at their interface. The system displays a photonic analogue of the quantum spin Hall effect, and supports two states at the edge between the photonic crystals, propagating in opposite directions. Using a Fourier-space reflectometric experimental setup, we access the far

fields of the edge states. Our experiments reveal that the far-field signals emanating from the oppositely propagating edge states carry unique, opposite circular polarizations which we identify as a signature of the underlying photonic spin-orbit coupling. We find that there exists a spin-spin scattering in the system due to an inherent symmetry-breaking, and quantify it using dispersion measurements.

The results and findings of chapter 4 are used to visualize the real-space propagation of these states in chapter 5. Using polarized monochromatic laser light, we selectively excite these states and visualize their propagation. Topological waveguides, sharp junctions, topological ring cavities, and topological cavity-waveguide coupler systems were fabricated on silicon photonic crystals to explore the potential and limitations of topological transport in this platform. We study the effect of shape and size of the topological cavities on the confinement, scattering and splitting of the cavity modes. We observe that the conservation of spin dominates the coupling from waveguides to cavities, in contrast to the usual principle of momentum conservation that governs their traditional counterparts. Finally, we present first results of near-field measurements on these photonic crystals. Our near-field microscopy setup consists of an aperture probe which picks up the evanescently decaying optical fields above the topological edges. In this experiment, we visualize the near-field propagation of the edge states in real and Fourier space, and observe various Bloch harmonics that constitute the edge-state near fields. Our access to the phase and polarization information of these components could potentially lay another stepping stone towards a complete understanding of the nature of these states, aiding the realization of novel nanodevices that control light in fascinating ways.



# SAMENVATTING

Licht vormt een integraal onderdeel van ons bestaan op deze planeet. Op vele verschillende manieren blijft het ons elke dag verbazen, inspireren en ondersteunen. Het speelt een sleutelrol in de vooruitgang van wetenschap en technologie en heeft daarnaast vele toepassingen die onze kwaliteit van leven verbeteren. De wisselwerking tussen licht en materie is een belangrijk mechanisme in deze toepassingen. Diverse nieuwe effecten komen voort uit de interactie tussen licht en materie op een schaal kleiner dan de golflengte. Deze interactie laat zich naar gelang aanpassen door materialen op ingenieuze wijze te structureren en door de inherente eigenschappen van licht te gebruiken. Een belangrijke eigenschap van licht is het feit dat electromagnetische velden vectorieel van aard zijn, hetgeen lichtgolven in staat stelt om verschillende polarisaties aan te nemen.

Fotonische kristallen zijn structuren met een periodieke schikking van materialen op de nanoschaal – kleiner dan de golflengte van licht. In dit proefschrift onderzoeken we, met behulp van concepten als chiraliteit en topologie, de interactie tussen gepolariseerd licht en fotonische kristallen met verschillende geometrieën. We gebruiken verschillende ruimtelijke symmetrieën van nanostructuren — en het breken van die symmetrieën — om interessante effecten zoals asymmetrische transmissie en verstrooiingsvrij transport van licht te bewerkstelligen.

We introduceren een aantal sleutelconcepten in het inleidingshoofdstuk (hfdst. 1). Een bespreking van de vectoriële aard van licht wordt opgevoerd, met bijzondere aandacht voor methoden om gepolariseerd licht uit te drukken en te kwantificeren, waaronder het gebruik van Stokes-parameters. Vervolgens introduceren we fotonische kristallen, met nadruk op de natuurkunde van de voortplanting van licht in de vorm van Blochgolven; dispersierelaties - verbanden tussen optische frequenties en golfvectoren - die een bandkloof laten zien; en de opsluiting en geleiding van licht in plakken materiaal voorzien van een fotonisch-kristalstructuur.

Chirale fotonische kristallen, die niet spiegelsymmetrisch zijn, zijn van bijzonder belang in dit proefschrift. We bespreken de mogelijkheden tot manipulatie van gepolariseerd licht door interactie met chirale voorwerpen. Het inleidingshoofdstuk besluit met een kort overzicht van het concept 'topologie' in de fotonica, hetgeen een belangrijke rol speelt in het tweede deel van het proefschrift. We concentreren ons daarbij op de natuurkunde van toestanden die leven aan de randen van topologische systemen. De voortplanting van zulke toestanden kan beschermd worden tegen terugverstrooiing door onef-

fenheden. In dat kader beschrijven we in dit proefschrift de verwezenlijking van een optisch analogon van het kwantum-spin-Halleffect voor elektronen, waarbij in ons geval lichtgolven van verschillende “spin” terugverstrooiingsvrij transport in tegengestelde richtingen vertonen, net zoals het geval is voor elektronen met tegengestelde spin. In het laatste deel van het hoofdstuk bestuderen we het ontstaan van topologische randtoestanden uit symmetriebrekingen en bandomkering in een fysiek systeem. Dit doen we aan de hand van een intuïtief theoretisch model: het Su-Schrieffer-Heegermodel.

In het eerste deel van dit proefschrift wordt de relatie tussen resonanties in fotonische systemen en hun verstrooiingseigenschappen onderzocht. Het theoretische kader dat geschetst wordt in de twee hoofdstukken van dit deel voorziet ons van methoden om nanofotonische systemen met interessante eigenschappen te ontwerpen. De respons van fysieke systemen op lichtgolven van buitenaf wordt grotendeels bepaald door de interactie van licht met de natuurlijke resonanties van de systemen, d.w.z. de eigenmodi van lichtvelden die deels het systeem uit kunnen lekken als straling. Zulke modi worden quasinormale modi genoemd. De verstrooiingsmatrix kwantificeert de respons van een systeem op licht van buitenaf. In hoofdstuk 2 ontwikkelen we een theoretisch formalisme om de verstrooiingsmatrix van optische systemen te voorspellen uit de verre-veldeigenschappen van hun quasinormale modi. We laten zien dat, in tegenstelling tot bestaande theoretische benaderingen, ons formalisme over een breder frequentiebereik en groter aantal in- en uitgangskanalen geschaald kan worden, zodat de verstrooiing voorspeld kan worden uit de eigenschappen van slechts een beperkt aantal berekende modi.

Een beter begrip van de optische respons van fysieke systemen helpt ons om compacte polarisatiemanipulators te verwezenlijken. In hoofdstuk 3 passen we het ontwikkelde formalisme toe op de interactie van gepolariseerd licht met chirale systemen. We beschouwen een specifiek type chirale respons: asymmetrische transmissie (AT). Asymmetrische transmissie is het verschil in doorlating van gepolariseerde lichtgolven die vanuit tegengestelde richtingen op een systeem vallen. We laten het verband zien tussen deze resonante chirale respons en de niet-resonante eigenschappen van het systeem, en we gebruiken ons theoretisch formalisme om AT voor elk gegeven systeem te kunnen bepalen. We ontdekken dat het beginsel van reciprociteit een fundamentele limiet stelt aan de maximale sterkte van AT in fysieke systemen. Tenslotte demonstreren we een methode om geoptimaliseerde structuren te ontwerpen die de maximaal haalbare AT voor diëlektrische structuren kunnen bereiken. We demonstreren deze methode door een sterk chirale fotonisch-kristalplak te ontwerpen als voorbeeld.

Het concept ‘topologie’ heeft recentelijk veel belangstelling gewekt in de fotonica door veelbelovende toepassingen in het sturen en manipuleren van licht in zowel het klassieke als het kwantumdomein. Het tweede deel van dit proefschrift is gewijd aan de bestudering van topologische randtoestanden in silicium fotonische kristallen. In hoofdstuk 4 fabriceren we een topologisch



fotonisch systeem, bestaande uit een grensvlak tussen twee fotonische kristallen met licht verschillende geometrieën op een ‘silicium-op-isolator’ chip. De twee fotonische kristallen verschillen in de topologische eigenschappen van hun bandstructuren, en kunnen topologisch beschermde randtoestanden onderhouden op hun grensvlak. Het systeem vertoont een fotonisch analogon van het kwantum-spin-Hall-effect, met twee toestanden van licht die zich in tegengestelde richting voortplanten op de rand tussen de fotonische kristallen. Met behulp van een hoek-opgeloste reflectometrische experimentele opstelling detecteren we de verre-veldstraling van de randtoestanden. Ons experiment laat zien dat de verre-veldsignalen die voortkomen uit zich tegengesteld voortplantende randtoestanden afzonderlijke, tegengestelde circulaire polarisaties voeren. Dit herkennen we als een teken van de onderliggende fotonische spin-baankoppeling. We merken op dat er een spin-spinverstrooiing in het systeem plaatsvindt door een inherente symmetriebreking en we kwantificeren dit aan de hand van dispersiemetingen.

De resultaten en bevindingen van hoofdstuk 4 worden in hoofdstuk 5 gebruikt om de voorplanting van deze toestanden te visualiseren. Met behulp van monochromatisch gepolariseerd laserlicht slaan we deze toestanden aan en beelden we hun voortplanting af. Topologische golfgeleiders, scherpe bochten, en ringvormige topologische trilholtes werden gefabriceerd in silicium fotonische kristallen om de mogelijkheden en de beperkingen van topologisch transport in dit platform te bestuderen. We onderzoeken het effect van vorm en grootte van de topologische trilholten op de opsluiting, verstrooiing en ontlasting van de trilholtemodi. We bemerken dat het behoud van spin de koppeling van golfgeleider naar topologische trilholte bepaalt, in tegenstelling tot het mechanisme van impulsbehoud dat de bepalende factor is in de koppeling naar traditionele trilholtes. Tenslotte presenteren we eerste metingen van het nabije veld van deze fotonische kristallen. Onze nabije-veldmicroscopie bestaat uit een spitse naald die het evanescent afvallende optische veld boven de topologische randen oppikt. In dit experiment visualiseren we de nabije-veldvoortplanting van de randtoestanden met hoge resolutie, en observeren meerdere Bloch-overtonen die het nabije veld van de randtoestanden vormen. De mogelijkheid om de fase en de polarisatie van deze componenten te bepalen is een springplank om een volledig begrip te vormen van de aard van topologische toestanden. Dit kan een belangrijke bijdrage zijn aan de ontwikkeling van vernieuwende nanostructuren die licht op fascinerende wijze controleren.



# ACKNOWLEDGEMENTS

A climb up the mountain is one of the most overused metaphors for life. It's for a good reason; took me four wonderful years to realize that. It was a hell of a climb, and I was fortunate enough to have been surrounded by a bunch of amazing companions throughout the journey — people who believe in you and guide you to the right directions, who shed light when it is dark, who pick you up when you fall down, who act as a breath of fresh air, and who inspire, motivate, and cheer for you no matter how the climb goes. Here, I would like to express my immense feeling of gratitude to the people who were with me during the climb.

Not many doctoral students have the special privilege of having two supervisors. Ewold and Kobus, thank you for providing me this marvellous opportunity and the faith that you had when hiring an engineer with a limited physics background to an applied physics Ph.D. programme. Such a diverse thesis would not have been possible without your flexibility and the freedom you gave to choose the topics for research. I used to thoroughly enjoy our weekly meetings. Your vast knowledge and expertise have been instrumental in my scientific growth. Ewold, I know I could never say this enough: thank you for your patience, dedication, motivation and all the time that you spent for teaching me. I am so lucky to have an advisor who is as enthusiastic as me about the work I do. Thank you for all your help with the thesis preparation. Kobus, I am grateful for the delightful teaching moments. Your wisdom and attitude towards life have had a good influence in the development of not only my scientific temper, but also my emotional intelligence.

I had to encounter a great deal of theoretical work during my Ph.D. life. I still remember the first time approaching Filippo, seeking help with the prediction of asymmetric transmission in systems with overlapping modes. Although it seemed to be a trivial problem then, it later evolved into a strong, long-lasting, and fruitful collaboration. Filippo, you were almost a third advisor for me, and you showed tremendous amount of patience towards my stupid questions and countless requests for help. I am so thankful for all of it. Another important collaboration that I was fortunate to be part of was the one on near-field experiments at the Delft University of Technology. Thomas and Sonakshi, thank you for the beautiful near-field measurements. Sonakshi, I also appreciate your support during the final days of the submission of my thesis. Aron, I am grateful to you for introducing the near-field setup to me and for staying late hours in the lab for our preliminary measurements on the topological photonic crystals.

A “shape-shifting” optical experimental setup which we call *Mystique* is at the heart of the far-field results presented in this thesis. Building an optical experimental setup from scratch was not an easy task. One of the perks of being employed at a great institute like AMOLF is the abundant availability of excellent technical support. Jan Bonne, I learnt much from you about the cleaning and alignment of optical components. I value your support in maintaining *Mystique* in a running condition. Special thanks to Hugo and Thomas for their help and suggestions in designing and building the setup. Dirk-Jan and all the amazing people at the engineering workshop, thank you for the mechanical design and manufacturing of the sample holder for *Mystique*. I would like to thank Wiebe and the rest of the ICT department for numerous timely PC supports. Thank you Hincó, for your helps and the positive vibe that you spread around.

If it hadn’t been for the fabricated topological photonic crystal samples, I’d probably have no second part for this thesis. Dimitry and Bob, both of you contributed equally in teaching me the intricate steps in nanofabrication, developing great recipes that we use at AMOLF nanolab, and troubleshooting the complex machines which make the nanostructures. I am particularly grateful to Dimitry for the help received in cleaving the waveguides of the fabricated samples used for near-field experiments. I would also like to thank Andries and Hans for teaching me how to take beautiful pictures of the fabricated samples in the scanning electron microscope.

Being part of two research groups at the same time was a unique experience for me. This meant I had not only two different perspectives to count on for each scientific problem, but also two diverse sets of exceptional friends to hold on to in life. Lorenzo and Dolfine, it was an incredible journey we started together with the summer school in Italy during the beginning phase of our lives as doctoral students. The inordinate rapport and comfort we found in each other made our friendship stronger, and it helped us to tackle many difficult challenges which we had to encounter later. Freek, thank you for being an extremely nice, caring and considerate officemate, and a great friend. The numerous practical insights that you shared during our time together have had a great influence in my research life. Rick, being one of the most knowledgeable senior students at AMOLF, you were a person that a new student could always look up to. Thank you for all your help.

John, you were a great source of assistance and relief for me. As a colleague, talented physicist, movie enthusiast, and a fellow Keralite, you offered a splendid company both at the office and outside. Robin, thank you for being a good friend. You never cease to amaze me with your quick-wits and intriguing questions. The Fabry-Pérot exercise was great fun. Kevin, it was a delight to have you as a neighbour at the fiber-tapering setup when I was building *Mystique*. Thank you also for the mental support during writing of this thesis. Jesse, thank you for drafting an excellent Dutch translation of the summary of this thesis. René, I appreciate you for taking over the *topological torch*. I

am confident that you, together with our collaborators in Delft, will take it forward to newer places and greater heights. Thank you also for the detailed proof-reading of the manuscript of this thesis. Alejandro, I appreciate the interest you shared on topological photonics and all the interesting discussions. Pierre, you often surprise me with the dedication and thoroughness that you show on attending random requests for help. I feel thankful also to the rest of the current and past group members — Randy, Boris, Anouk, Ruben, Isabelle, Lars, Giada, Juha, Amy, Hessel, Su-Hyun, Irina(s), Felipe, Thijs, Martin, Javier(s), Jente, Roel and Marc — for your contributions during the group meetings and for fostering a positive and friendly environment within the group(s).

One thing I particularly like about AMOLF is the connecting culture it promotes. During these four years, I got an opportunity to interact with many excellent scientists also from outside the group. Femius, thank you for the enthusiasm, appreciations, and the interesting questions during presentations. Said and Sander, thank you for the nice chats and the critical reading of my manuscripts. I benefited professionally and personally a lot from interactions with a bunch of colleagues and friends at AMOLF and elsewhere, including (not limited to), Albert, Erik, Bruno, Esther, Clara, Cocoa, Radek, Ruslan, Sachin, Marko, Nick, Andrea, Sophie, Benjamin, Harshal, Biplab, Parisa, Jenny, Ale, Maisie, Vanessa, Giorgio, Lukas, Roos, Reshma, Vikas, Gopika, Arko, Rifat, Ilja, Niesko and Raziman. I am grateful to all of you.

We have a saying in Malayalam [poor translation alert]: *even if you travel to the far side of the moon, you'll spot a Malayali there*. Amsterdam almost felt like a home away from home due to the presence of a good number of fellow Malayalis I found here. Shyama, Stephen, Rakesh, Dona, Dante, Vishnu, Nithin, Lekshmiechi and Sajithettan; thank you for keeping me high-spirited with Kerala food, politics, books, and movies. I'm also grateful to the emotional support I received from all my friends back home.

Lastly and most importantly, I would like to thank my family. *Achan* and *Amma*, you were my first teachers and it was you who prepared me for the journeys to come. Thank you for teaching me how to find my feet on difficult terrains. Yet, I know that these years have not been easy for you. Thank you for supporting me regardless. Thank you also for giving me an awesome little sister. Ammu, I don't know how I would have survived in this life hadn't you been there. Thank you for completing my thoughts faster than me, being a correcting force in my life, and thank you for filling it with joy and hope in the times of sorrow, despair, and frustrations. Finally, Manju, thank you for the care, patience, understanding, and unconditional love. I wonder how different the final phase of my Ph.D. life would have been without you. Thank you for making it more colourful and lively.

We were talking about the climbs in life. At the end of this climb, I realize how (the mountain shows how) small I am, how little I know and how little I could have achieved without these companions.



## ABOUT THE AUTHOR

Nikhil Parappurath was born in 1990 in Perinthalmanna, India. In 2011, he obtained a Bachelor of Technology degree in electronics and communication engineering from Kannur University. After that, he joined Cochin University of Science and Technology to study optoelectronics and laser technology. During this Master's program, Nikhil performed research at Tampere University of Technology in Finland under the supervision of dr. Godofredo Bautista and prof. Martti Kauranen, to write a thesis on nonlinear optical microscopy of carbon nanotubes. After graduating from Cochin University of Science and Technology with a Master of Technology degree in 2014, Nikhil started as a PhD researcher at the AMOLF research institute in Amsterdam, the Netherlands. He carried out his PhD research in the scientific groups of prof. Ewold Verhagen and prof. Kobus Kuipers during the period from 2015 to 2019. The results are presented in this thesis. Nikhil's work has been presented at several national and international conferences and published in refereed journals.





# LIST OF PUBLICATIONS

1. F. Alpeggiani, N. Parappurath, E. Verhagen, and L. Kuipers, *Quasinormal-mode Expansion of the Scattering Matrix*, Physical Review X 7, 0214035 (2017) (**Chapter 2**).
2. N. Parappurath, F. Alpeggiani, L. Kuipers, and E. Verhagen, *The Origin and Limit of Asymmetric Transmission in Chiral Resonators*, ACS Photonics 4, 884 (2017) (**Chapter 3**).
3. N. Parappurath, F. Alpeggiani, L. Kuipers and E. Verhagen, *Direct Observation of Topological Edge States in Silicon Photonic Crystals: Spin, Dispersion, and Chiral Routing*, in review; preprint at arXiv:1811.10739 (2018) (**Chapter 4, 5**).
4. N. Parappurath, R. Barczyk, L. Kuipers, and E. Verhagen, *Topological cavity modes and spin-locked cavity-edge coupling in dielectric photonic crystals*, in preparation (**Chapter 5**).
5. S. Arora, N. Parappurath, T.A. Bauer, E. Verhagen and L. Kuipers, *Near-field imaging of edge state propagation in topological photonic crystals at telecom wavelengths*, in preparation (**Chapter 5**).